Correlation between SQUID and Fluxgate Magnetometer Data for Geomagnetic Storms

by

Temwani-Joshua Phiri

Thesis presented in partial fulfilment of the requirements for the degree of Master of Engineering (Research) in Electronic Engineering at Stellenbosch University

Supervisor: Prof. Coenrad J. Fourie

Department of Electrical and Electronic Engineering

Co-supervisors: Daniel J. Gouws and Elda F. Saunderson

Technology Group, SANSA Space Science

Date: March 2013

Declaration

By submitting this dissertation electronically, I declare that the entirety of the work contained therein is my own, original work, that I am the owner of the copyright thereof (unless to the extent explicitly otherwise stated), that reproduction and publication thereof by Stellenbosch University will not infringe any third party rights and that I have not previously in its entirety or in part submitted it for obtaining any qualification.

Date: March 2013

Abstract

Correlation between SQUID and Fluxgate Magnetometer Data for Geomagnetic Storms

T.J. Phiri

Department of Electrical and Electronic Engineering,

University of Stellenbosch,

Private Bag X1, Matieland, 7602, South Africa.

Thesis: M. Eng. (Research) in Electronic Engineering

March 2013

Geomagnetic storms are primarily driven by the rapid transfer of energy from the solar wind to the magnetosphere. The mechanism of energy transfer involves the merging of the interplanetary magnetic field (IMF) to the geomagnetic field in a process known as magnetic reconnection. This leads to an influx of energetic, charged particles into the magnetosphere so that current systems are enhanced. Specifically, an increase in the equatorial ring current leads to a decrease in the surface field. Geomagnetic storms are thus characterized by a strong decline in the horizontal components of the geomagnetic field, lasting from several hours to days. The intensity of a storm is described by the disturbed storm-time (D_{st}) index, which is essentially a measure of the deviation from the typical quiet day variation along the equator. Severe storms can lead to the disruption of high frequency (HF) communications as a consequence of a strongly perturbed ionosphere. By the same token, the global positioning system (GPS) can become highly unreliable during magnetically disturbed conditions, yielding distance errors as large as 50 meters. The impact of geomagnetic activity and other solar-driven processes on technology systems are collectively known as space weather. Magnetic field sensing thus forms an important part of space weather forecasting and is vital to space science research as a means of improving our understanding of solar wind-magnetosphere interactions.

This study examines the use of magnetometers built as SQUIDs (Superconducting Quantum Interference Devices) for monitoring the geomagnetic field for space weather forecasting purposes. A basic theory of superconductivity is presented and subsequently the key aspects governing the operation of SQUIDs are discussed. Space weather is also introduced with respect to the various processes on the sun that perturb the magnetosphere and hence the geomagnetic field.

The method of analysis was basically to Fourier-transform the data using the Wiener-Khintchine theorem. A systematic approach to Fourier analysis is thus presented, demonstrating the superiority of the Wiener-Khintchine theorem in noise reduction. The suitability of SQUID magnetometers for space science research is demonstrated by a comparative study between SQUID and fluxgate datasets for magnetic storms during 2011. Strong correlation was observed between the frequency content of the SQUID and fluxgate signals. This result supports South Africa's SQUID project, currently undertaken as a collaborative effort between SANSA Space Science and the Department of Electrical and Electronic Engineering at Stellenbosch University. This thesis thus lays a foundation for future research involving advanced magnetometry using SQUIDs.

Opsomming

Korrelasie tussen SQUID en Fluxgate Magnetometer Datastelle vir Geomagnetiese Storms

(Correlation between SQUID and Fluxgate Magnetometer Data for Geomagnetic Storms)

T.J. Phiri

Departement Elektries en Elektroniese Ingenieurswese,

Universiteit van Stellenbosch,

Privaatsak X1, Matieland, 7602, Suid Afrika.

Tesis: M. Ing. (Navorsing) in Elektroniese Ingenieurswese

Maart 2013

Geomagnetiese storms word hoofsaaklik gedryf deur die vinnige oordrag van energie van die sonwind na die magnetosfeer. Die meganisme van energie oordrag behels die samesmelting van die interplanetêre magneetveld (IMV) met die geomagneetveld, in 'n proses wat bekend staan as magnetiese heraansluiting. Dit lei tot 'n instroming van energieke elektries-gelaaide deeltjies, tot in die magnetosfeer, met die gevolg dat magnetosferiese elektriese stroomstelsels versterk word. 'n Toename in die ekwatoriale ringstrome lei spesifiek tot 'n afname in die horisontale komponent van die geomagnetiese veld. Geomagnetiese storms word dus gekenmerk deur 'n sterk afname in die horisontale komponent van die geomagnetiese veld, 'n afname wat etlike ure tot dae kan duur. Die intensiteit van 'n storm word beskryf deur die storm-tyd versteurings indeks , 'n maatstaf van die afwyking van die tipiese stil dag magnetiese variasie langs die ewenaar. Ernstige storms kan lei tot die ontwrigting van hoë frekwensie (HF) kommunikasie as 'n gevolg van 'n erg versteurde ionosfeer. Soortgelyk kan die Globale Posisionering Stelsel (GPS) hoogs onbetroubaar word tydens magneties versteurde toestande, en posisiefoute so groot as 50 meter veroorsaak. Die impak van geomagnetiese aktiwiteit en ander sonkrag gedrewe prosesse op tegnologie is gesamentlik bekend as ruimteweer. Magneetveldmetinge vorm dus 'n belangrike deel van ruimteweervoorspelling en is noodsaaklik vir ruimtewetenskaplike navorsing as 'n middel om die sonwind-magnetosfeer interaksies beter te verstaan.

Hierdie studie ondersoek die gebruik van SQUID (Engels: Superconducting Quantum Interference Device) magnetometers vir die monitering van die geomagnetiese veld vir ruimteweervoorspellingsdoeleindes. 'n Basiese teorie van supergeleiding word aangebied, waarvolgens die sleutelaspekte van SQUIDs bespreek word. Ruimteweer word ook voorgestel in terme van die verskillende prosesse op die son wat die aarde se magnetosfeer en dus die geomagnetiese veld versteur.

Die analisemetode wat hier gebruik word, is om die Fourier-transform van data met die Wiener-Khintchine theorema te bereken. A sistematiese metode vir Fourier-analise word aangebied, wat die superiorireit van die Wiener-Khintchine teorema vir ruisvermindering demonstreer. Die geskiktheid van SQUID magnetometers vir ruimtewetenskaplike navorsing word gedemonstreer deur 'n vergelykende studie tussen SQUID- en vloedhek-datastelle vir magnetiese storms gedurende 2011. Sterk korrelasie is waargeneem tussen die frekwensie-inhoud van die SQUID- en vloedhekseine. Hierdie resultate ondersteun Suid-Afrika se SQUID-projek, wat tans as 'n samewerkingspoging tussen SANSA Space Science en die Departement Elektriese en Elektroniese Ingenieurswese aan die Universiteit van

Stellenbosch bedryf word. Hierdie tesis lê 'n fondasie vir toekomstige navorsing oor gevorderde magnetometrie met SQUIDs.

Acknowledgements

I am grateful to my supervisor, Prof. Coenrad Fourie, for guiding this study with insight and enthusiasm in a manner that made it both scholastic and enjoyable. He has been a great inspiration and I am privileged to have been his student. Mr. Daniel Gouws and Mrs. Elda Saunderson – my external co-supervisors at SANSA Space Science in Hermanus, have also been of invaluable help. I'm indebted to them for their constant support and confidence in me. My interactions with them in and away from the work environment were very pleasant.

I extend my gratitude to the National Astrophysics and Space Science Programme (NASSP) for awarding me a bursary that facilitated for coursework at the University of Cape Town (UCT) and subsequently research at Stellenbosch University (SU). I am thankful to Mrs. Nicky Walker for adequately addressing all administrative issues pertaining to my relationship with NASSP. In June 2012 I also received funding from SANSA Space Science and the Postgraduate and International Office (PGIO) at SU for a research visit to the Low-Noise Underground Laboratory (LSBB) in Rustrel, France. This proved a very important and worthwhile trip and I am indebted to the individuals who ensured that funds were available at the right time. I also convey my gratitude to the National Research Foundation (NRF) for the Grant-Holder-bursary awarded through SU. This facilitated for my continued stay in South Africa to successfully complete my research.

Being based at SANSA Space Science for the duration of my study, I owe a debt of appreciation to management and staff for making my stay comfortable and fruitful by providing assistance in different ways and at various times. I appreciate the exposure of being based at such a facility and I am very thankful for all the privileges I enjoyed in that community over the last 18 months. I wish to acknowledge by name Dr. Pierre Cilliers, for always being at hand to respond to a variety of questions and giving helpful hints on digital signal processing techniques; Dr. Ben Opperman helped to overcome a huge hurdle in downloading data; Dr. John Habarulema, Dr. Stefan Lotz and Dr. Zama Katamzi were key in helping me gain a better understanding on magneto-ionosphere interactions; last but not least, Mr. Louis Loubser and Mr. Emmanuel Nahayo for helping me understand fluxgate data better.

In the last 6 months of my study I enjoyed correspondence with Prof. Pascal Febvre and Dr. Elisabeth Pozzo di Borgo after meeting them at LSBB. I learned a great deal about the science at LSBB and specifically on processing and interpreting SQUID data. I am grateful to both of them for their availability and willingness to help wherever they could. Prof. Febvre was instrumental in sharpening my understanding of spectral analysis using Fast Fourier transforms.

The student community at SANSA Space Science has also been of value to me. In particular Electdom Matandirotya and Tshimangadzo Matamba have been very supportive and shown much kindness to me by their thoughtful deeds; Nicholas Ssessenga frequently helped me troubleshoot problems in MATLAB and made many helpful suggestions; my former classmates at UCT in the NASSP Space Science class of 2011 have stood with and by me through all the ups and downs of my work. Michael Afful, Samuel Oronsaye and Doreen Agaba, I salute you.

Dedicated to my parents, Fred and Cathy, for teaching me to read and write

Table of Contents

List of Figures

List of Tables

1 Introduction

Essentials of Superconductivity

1.1 Introduction to Superconductivity

Superconductivity is a macroscopic quantum effect whereby the electrical resistance of a material transitions to zero at cryogenic temperatures [1, 2]. Thus a superconductor exhibits perfect conductivity and is described by three important parameters: the critical temperature T_c, below which a material transitions to the superconducting state, the critical current I_c, defined as the maximum current that can be carried by a material before its superconductivity is "destroyed", and the maximum (critical) magnetic field H_c, that can be applied to the superconductor without causing it to lose its superconductive properties [1]. Typically, both I_c and H_c increase as the temperature of the superconductor is lowered farther below T_c.

Superconductors are classified as type I if the induced magnetization, $\boldsymbol{M}$, in the material is anti-parallel to the applied field $\boldsymbol{B}$. In type II materials $\boldsymbol{M}$ is field aligned so that type II materials are paramagnetic in the superconducting state. On the other hand, type I materials are perfectly diamagnetic since $\boldsymbol{M}$ is opposes the applied field in such a way that it leads to the condition $\boldsymbol{B} = 0$ within the materials interior. This phenomenon of flux expulsion is called the *Meissner effect* [1], illustrated schematically in Figure 1.1. Though type II superconductors "defy" the Meissner effect, the magnetic flux is only allowed to accumulate in small packets equal to 2.07×10^{-15} T-m^2, a quantity defined as the fluxon, Φ_0 [3]. This enables type II superconductors to retain their superconducting properties in stronger magnetic fields. The two classes of superconductors are also distinguished in their respective ranges of critical temperatures. For type I materials (which are mostly pure metals), T_c extends from 0.01 K to 9.3 K, while type II superconductors have critical temperatures in the range 25 K to 125 K [1, 3].

1.1.1 The Phenomenon of Superconductivity

Superconductivity was first observed in 1911 by H. K. Onnes as he studied the behaviour of the resistance of mercury as it was cooled using liquid helium [1]. Contrary to expected results, at around 4.2 K (the boiling point of helium) the resistance of the mercury *abruptly* dropped to zero. This feature is definitive for all superconductors and defines the transitioning of materials to the superconducting state at their respective critical temperatures. Figure 1.2 shows the characteristic resistance-temperature curve for a superconductor.

Various models have been proposed to explain the mechanism(s) governing superconductivity. The Bardeen-Cooper-Schrieffer (BCS) theory formulated in 1957 is one of the most robust, providing a description of superconductivity on a microscopic scale in terms of the behaviour of electrons as opposed to a formulation built on macroscopic observations [1, 4].
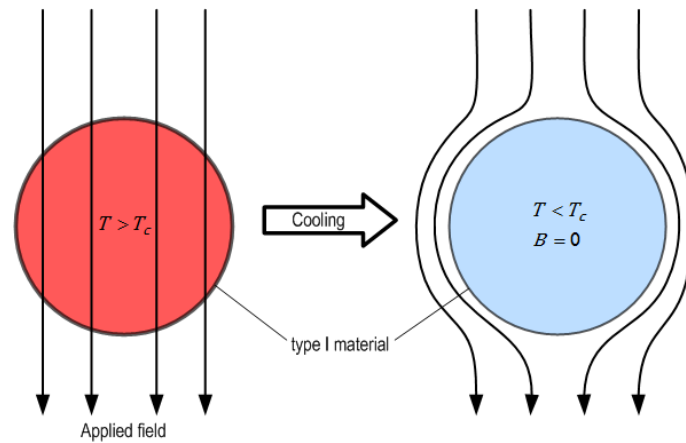
Figure 1.1: Flux expulsion in a type I superconductor. Flux does not penetrate the interior of the superconductor when it is cooled below its critical temperature. The Meissner effect is actually due to circular currents (not shown) whose fields are opposite the applied field, so that they "cancel" out.
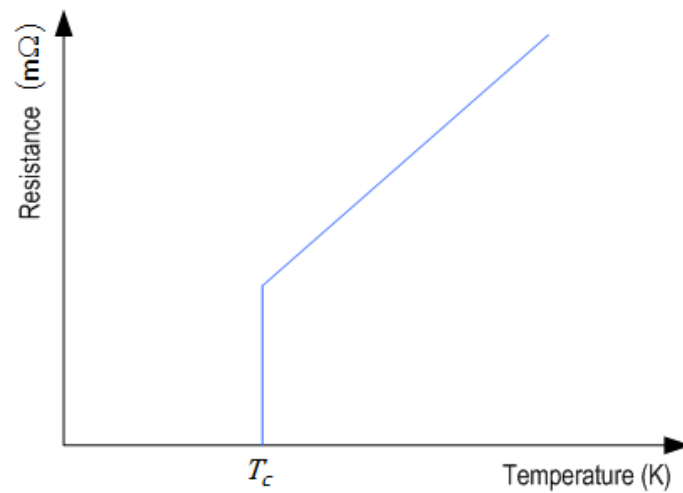
Figure 1.2: Characteristic Resistance-temperature curve for a Superconductor. There is a sharp transition to zero resistance at the critical temperature.

This theory builds up on earlier work which suggested that superconductivity arose primarily due to electron-phonon interactions [5] and states that the condition for an attractive *phonon interaction[1]* is

$$\Delta\varepsilon < \hbar\omega, \tag{1.1}$$

where $\Delta\varepsilon$ is the energy difference between the electron states involved and $\hbar\omega$ is the phonon energy of the ground state. Here, ω is the vibration frequency and $\hbar = h/2\pi$, where h is Planck's constant.

The phonon interaction leads to a screening of the repulsive Coulomb force between electrons, so that there is an electron-electron attraction which mostly occurs between electrons of opposite spin and momentum. This electron-electron attraction gives rise to the so-called *Cooper pairs (superelectrons)* [4, 5]. Electron pairing holds as long as the thermal energy due to lattice vibrations is lower than the bond energy between the electron pairs which is given approximately as $2\Delta \approx 10^{-3}$ eV. This helps to conceptualize why superconductivity necessarily occurs at very low

---

[1] "Phonon interaction" was the term used in the BCS theory to describe electron interactions due to the influence of phonons.

2

temperatures and accounts for the observed increase in the *supercurrent* density farther below the critical temperature due to increasing density of Cooper pairs. In addition, Cooper pairs have the property that they move with the same net momentum so that they do not experience scattering as a result of collisions with one another. Therefore, once generated, supercurrents can flow for a very long time since they are lossless [1].

The classical model of superconductivity is built on the assertions of zero resistance and total flux expulsion [1], encapsulated in two equations called the first and second London equations respectively, namely:

$$E = \frac{\partial}{\partial t}(\Lambda J), \text{ and} \tag{1.2}$$

$$\nabla \times (\Lambda J) = -B, \tag{1.3}$$

where E is the electric field, J is the current density, B is the magnetic field flux, and the London coefficient is defined as

$$\Lambda = \frac{m^*}{n^*(q^*)^2}, \tag{1.4}$$

where the mass m^*, and the charge q^*, of a superelectron are twice the mass and charge of an ordinary electron, respectively, and n^* is the superelectron density.

Replacing $J = (\nabla \times B)/\mu_0$ in equation (1.2) gives

$$E = \frac{\partial}{\partial t}\left(\frac{\Lambda}{\mu_0}\nabla \times B\right) = \frac{\Lambda}{\mu_0}\left(\nabla \times \frac{\partial}{\partial t}B\right). \tag{1.5}$$

Dimensional analysis shows that the term Λ/μ_0 must have units of squared length. Taking the square root gives the (London) penetration depth given as

$$\lambda = (\Lambda/\mu_0)^{1/2}. \tag{1.6}$$

The penetration depth is an intrinsic feature of superconductors. It describes the extent of penetration of magnetic fields [3].

A superconducting system can be adequately designed and built using equations (1.2) and (1.3) as well as others which may be derived from these (using the Maxwell relations) by appropriate substitutions and manipulation depending on the problem at hand. Superconductivity applications such as magnetic levitation are successfully constructed using the classical model [1]. Yet, as superconductivity is a quantum mechanical process, it is better explained using the macroscopic quantum model (MQM).

The MQM supersedes the classical model in that it incorporates both the electromagnetic and thermodynamic (Ginzburg-Landau theory) characteristics of superconductivity. By virtue of a quantum theory approach, violation of the Meissner effect in type II superconductors is clearly accounted for in the MQM in a systematic way [1]. In the MQM, all the important information that can be known about a system of very many superelectrons such as the density and movement is contained in a wave function of the form $\Psi(r, t) = \left(n^*(r, t)\right)^{1/2} e^{i\theta(r,t)}$.

The flow of the probability of Ψ leads to an expression for the supercurrent density in an isotropic superconductor [1]:

$$J_s = q^* n^*(r,t)\left[\frac{\hbar}{m^*}\nabla\varphi(r,t) - \frac{q^*}{m^*}A(r,t)\right],$$

(1.7)

where J_s is the supercurrent density (macroscopic quantum current density), A s a magnetic vector potential such that $B = \nabla \times A$, and θ represents the phase of Ψ and is real. Using equation (1.4) in (1.7), the supercurrent equation is conventionally expressed as

$$\Lambda J_s = -\left[A(r,t) - \frac{\hbar}{q^*}\nabla\varphi(r,t)\right],$$

(1.8)

from which the London equations can be recovered. Integration of (1.8) around a closed path c gives [1]

$$\oint_c \Lambda J_s \cdot dl + \oint_s (\nabla \times A)\cdot ds = \frac{\hbar}{q^*}\oint_c \nabla\varphi \cdot dl \,,$$

(1.9)

And in the limit where $\oint_c \nabla\varphi \cdot dl = 2\pi n$, with $n = 0,1,2,3, ...$ equation (1.9) becomes [6]

$$\oint_c \Lambda J_s \cdot dl + \oint_s B \cdot ds = \frac{2\pi\hbar}{q^*} n = n\Phi_0 \,,$$

(1.10)

where Φ_0 is a quantum of flux. Equation (1.10) states that the flux contained within a superconductor exists in fixed packets. These packets are in fact are a validation for the existence of Cooper pairs.

1.1.2   Electronics of Superconductors

One of the ways to verify flux quantization in superconductors is by studying the electrical properties of a system containing two superconductors separated by a thin non-superconducting region. Such a set up introduces some key concepts in superconductor electronics [2], such as the *Josephson Effect*. This is a quantum tunnelling of Cooper pairs from one superconductor to another across an insulating region. The insulator could either be a non-superconducting material (such as an oxide) or a weak link, which is a constriction in a superconductor wherein superconductivity is destroyed for $I > I_c$, thereby creating two superconducting regions on either side of the link [3]. Such a configuration is known as a Josephson junction and is shown in Figure 1.3.

<div align="center">(a)   (b)</div>
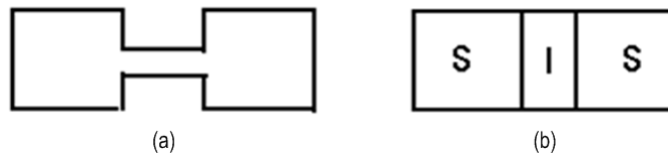
Figure 1.3: Josephson junction as a weak link (a) and as a Superconductor-Insulator-Superconductor (SIS) junction (b).

The tunnelling of Cooper pairs gives rise to a zero-voltage supercurrent,

$$I = I_c \sin\varphi \,,$$

(1.11)

where I is the Josephson current, I_c is the critical current of the junction, and φ is the phase difference between the wave functions on either side of the insulating layer.

Equation (1.11) defines the dc Josephson effect which is a statement that no voltage drop is developed across the junction given that the current flowing through it is not larger than I_c. If the junction is biased with a dc current so that the

4

current through the junction exceeds I_c, a voltage will develop across the junction. This property is used in digital electronics applications such as in latching gates and more recently in the development of rapid single flux quantum (RSFQ) logic circuits [7] where Josephson junctions maintain the zero-voltage state. If a Josephson junction is biased with a dc voltage across the junction, an alternating current develops due to a time-varying phase [1, 6]. This can be derived from the voltage phase relation

$$\frac{d}{dt}\varphi = \frac{2\pi}{\Phi_0}V \,,$$

(1.12)

$$\Rightarrow \varphi = \frac{2\pi}{\Phi_0}Vt + \text{constant}\,,$$

(1.13)

As can be seen, replacing φ in equation (1.11) with (1.13) results in an ac current through the junction.

The term $2\pi V/\Phi_0$ is the characteristic angular frequency, ω_J, with which the current oscillates. Using $\Phi_0 = 2.0679$ fT-m^2, the Josephson frequency is thus

$$\frac{f_J}{V} = \frac{\omega_J}{2\pi V} = \frac{1}{\Phi_0} = 483.6 \, \text{GHz/mV}\,.$$

(1.14)

Since the Josephson frequency has a voltage-dependence, Josephson junctions are successfully used for voltage standardization purposes [1, 8].

Flux quantization can easily be demonstrated by a parallel arrangement of two Josephson junctions a ring circuit as illustrated in Figure 1.4. This circuit arrangement forms the basis of a superconducting quantum interference device (SQUID) [1]. If the line integral $\oint_c \boldsymbol{J_s} \cdot d\boldsymbol{l}$ is evaluated for a path deep inside the superconductors, where the current density is negligible, we find

$$\oint_s \boldsymbol{B} \cdot d\boldsymbol{s} = \Phi = n\Phi_0\,.$$

(1.15)

Hence we see that the flux penetrating the circuit is quantized in units of Φ_0. If instead $\Phi = \left(n + \frac{1}{2}\right)\Phi_0$, then $\oint_c \boldsymbol{J_s} \cdot d\boldsymbol{l}$ is non-zero and the current will oscillate with a maximum value determined by the applied magnetic field [6].
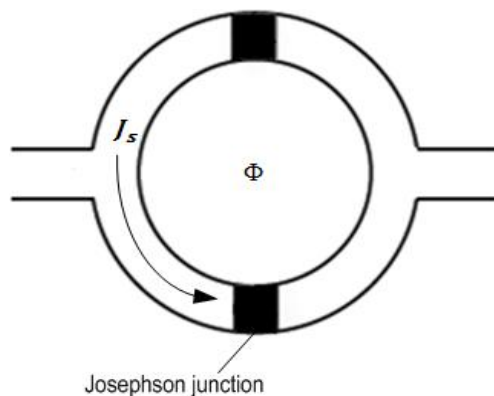
Figure 1.4: Basic dc SQUID configuration. Two Josephson junctions are arranged parallel to each other in a ring circuit.

If a dc current is supplied to the ring, then

$$I = I_1 + I_2 = I_c \sin\varphi_1 + I_c \sin\varphi_2, \tag{1.16}$$

where φ_1 and φ_2 are the phase differences across junctions 1 and 2 respectively. The overall phase difference around the ring must be such that [9]

$$\varphi_1 - \varphi_2 = \frac{q^*}{\hbar}\Phi = \frac{2\pi}{\Phi_0}\Phi, \tag{1.17}$$

where the phase differences can be expressed as $\varphi_1 = \delta_0 + (\pi\Phi/\Phi_0)$ and $\varphi_2 = \delta_0 - (\pi\Phi/\Phi_0)$, with δ_0 an arbitrary phase constant. Thus equation (1.16) simplifies to

$$I = 2I_c \sin\delta_0 \cos\frac{\pi}{\Phi_0}\Phi. \tag{1.18}$$

The current oscillates between its maxima when $\sin\delta_0 = 1$ in equation (1.18). Thus,

$$I_{max} = 2I_c\left|\cos\frac{\pi}{\Phi_0}\Phi\right|, \tag{1.19}$$

and this is in turn maximized whenever $\pi\Phi/\Phi_0 = n\pi$. We thus see that maximum current in a dc SQUID is observed when the total flux is quantized in integral multiples of Φ_0.

1.1.3   Modelling Josephson Junctions

If the current through a Josephson junction exceeds the critical current, the effect of resistance due to the presence of normal electrons and capacitance due to the separation between the two superconductors must be taken into account. The resulting circuit dynamics are well explained by the resistively and capacitively shunted junction (RCSJ) model shown in Figure 1.5. It also called the generalized Josephson junction.
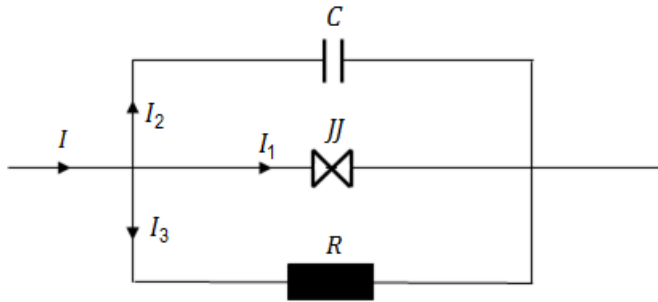
Figure 1.5: Generalized (RCSJ) model of a Josephson junction.

The current through the circuit is

$$I = I_1 + I_2 + I_3 = I_c \sin\varphi + C\frac{dV}{dt} + \frac{V}{R}. \tag{1.20}$$

But from (1.13) $V = (\Phi_0/2\pi)\frac{d\varphi}{dt}$ and we find a nonlinear second order differential equation with respect to the phase difference as

$$I = \frac{\Phi_0 C}{2\pi}\ddot{\varphi} + \frac{\Phi_0}{2\pi R}\dot{\varphi} + I_c \sin\varphi. \tag{1.21}$$

Dividing throughout by I_c and setting $\tau = 2\pi R I_c t/\Phi_0$, leads to the dimensionless equation [1]

$$i = \beta_c \frac{d^2\varphi}{d\tau^2} + \frac{d\varphi}{d\tau} + \sin\varphi \, , \qquad\qquad (1.22)$$

where $i = I/I_c$ and $\beta_c = 2\pi I_c R^2 C / \Phi_0$ is the Stewart-McCumber parameter. It describes whether or not the junction is more capacitive or more resistive. This can easily be seen by expressing β_c in the form

$$\beta_c = RC \frac{2\pi(I_c R)}{\Phi_0} = \frac{RC}{\omega_J} \equiv \frac{\tau_{RC}}{\tau_J} \, , \qquad\qquad (1.23)$$

where we have taken $I_c R = V_J$ as the typical voltage across a Josephson junction and have used equation (1.14). If the capacitive time constant, τ_{RC}, is much smaller than the time constant, τ_J, of the Josephson junction, $\beta_c \ll 1$. In this case, the first term on the right-hand side of equation (1.23) becomes negligible and the circuit's behaviour is determined purely by the Josephson junction and resistance. On the other hand, if $\tau_J \ll \tau_{RC}$, then $\beta_c \gg 1$ and the properties of the circuit are predominantly governed by the dynamics of a parallel RC circuit. A dc SQUID requires that $\beta_c \ll 1$ in order to minimize hysteretic effects [1].

1.1.4   High Temperature Superconductivity (HTS)

As pointed out in Section 1.1, type II superconductors have higher critical fields and higher critical temperatures than type I materials. This favours type II materials for most practical applications, since type I materials require somewhat complex and costly cryogenics and lose their superconductivity in fields as small as 0.1 T [1]. The two classes of superconductors are described intrinsically by the Ginzburg-Landau parameter [10], namely

$$\kappa = \frac{\lambda}{\xi} \, , \qquad\qquad (1.24)$$

where λ is the London penetration depth as defined in equation (1.6), ξ is the coherence length, given approximately by [1]

$$\xi = \frac{\hbar v_F}{\sqrt{3}(2\Delta)} \, , \qquad\qquad (1.25)$$

where v_F is the Fermi (background) velocity of electrons and 2Δ is the energy gap binding a Cooper pair. The coherence length, ξ, is roughly the smallest distance between Cooper pairs before the destruction of superconductivity. Type I materials have $\kappa < 1/\sqrt{2}$, while $\kappa > 1/\sqrt{2}$ defines a type II material [10]. Clearly, the coherence length is smaller than the London penetration depth for a type II material. This fact is the reason for the different characteristics observed between the two groups of superconductors.

Superconductors of the second class have two superconducting regions – the Meissner state which exists below the first critical field (H_{c1}) and the vortex (mixed) state which lies between the two critical fields (H_{c1} and H_{c2}). The two curves in Figure 1.6 provide a description of this, showing induction and reversible magnetization. The mixed state is so-called because of the phenomenon whereby flux enters the material without loss of superconducting properties. The flux penetration is in quantized amounts in structures known as vortices at whose centres the material is in the normal state [1, 11]. The radius of each vortex is ξ and as stated earlier, the unit of quantization is the fluxon, Φ_0. A schematic of this effect is shown in Figure 1.7.

Type II materials are able to retain their superconducting properties at high magnetic fields and higher critical temperatures because of the presence of vortices and their interaction with one another [12]. Type II superconductors

are usually alloys and compounds. Materials with $\kappa \gg 1$ are especially called high temperature $\left(\text{high-}T_c\right)$ superconductors and have transition temperatures of around 77 K or higher. Mostly ceramics, such superconductors include yttrium barium copper oxide, YBCO, ($YBa_2Cu_3O_7$) with critical temperature of 93 K. They are usually multi-layered in structure and this feature is in part responsible for the high-T_c characteristics [11]. Two other key high-T_c ceramics are the bismuth strontium calcium copper oxides (BSCCO) $Bi_2Sr_2CaCu_2O_8$ and $Bi_2Sr_2Ca_2Cu_3O_{10}$. They have transition temperatures of 92 K and 110 K, respectively.
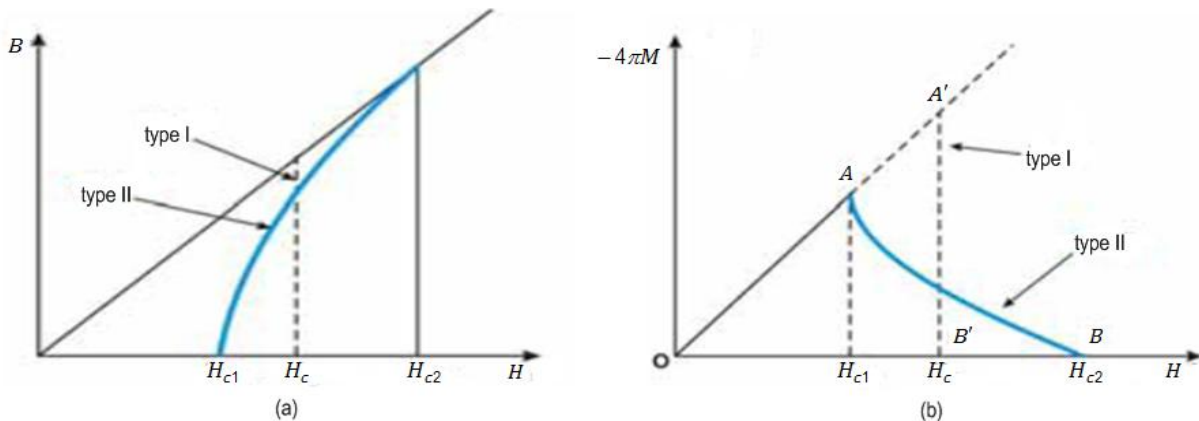
Figure 1.6: Induction as a function of the applied field (a); Reversible magnetization curve (b) (Source: The Discovery of Type II Superconductors (Shubnikov Phase), Kharkov Institute of Physics and Technology, Ukraine)
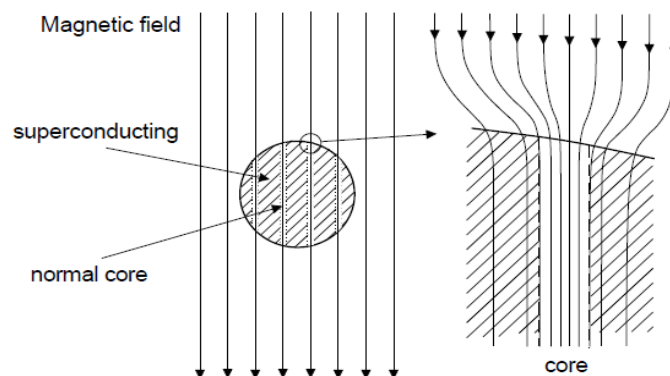
Figure 1.7: Type II superconductor in the mixed state flux penetration in a vortex. (Source: Vortex Properties from Resistive Transport Measurements on Extreme Type-II Superconductors, Doctoral Dissertation, Stockholm 2001, pp 11)

1.1.5   Application of Superconductivity to Magnetometry

Magnetometers built as SQUIDs are the most sensitive detectors of magnetic flux. However, due to the need for cryogenics involving liquid helium and liquid nitrogen for low-T_c and high-T_c materials, respectively, SQUIDs are not widely used in geophysical research. In this work, we report on the analysis of SQUID data from measurements at the Laboratoire Souterrain à Bas Bruit (LSBB) – a low-noise underground laboratory in Rustrel, France operating a low-T_c SQUID. The results of this research provide a good reference point for South Africa's SQUID project, currently undertaken as a collaborative effort between SANSA Space Science and the Department of Electrical and Electronic Engineering at Stellenbosch University.

1.2   Motivation

Inspiration for this research arises due to the need for systems monitoring faint magnetic signals for studying Earth-ionosphere coupling [17]. Geomagnetic data is used in space weather forecasting and studying solar-terrestrial dynamics, as well as exploring the Earth's interior [14]. Low frequency measurements are of key interest in geophysical science because the waves involved travel very long distances. Hence, with the appropriate shielding mechanisms, magnetic variations from outer space or half-way around the world from the location of a sensor could be detected. Fluxgate magnetometers are the conventional instrument for low-frequency measurements at magnetic observatories, typically sampling at 1 Hz or lower. However, various geophysical phenomena occur at frequencies up to 10 Hz. It is not sufficient to simply sample at a higher rate. A highly sensitive magnetometer with high frequency resolution is required and SQUID magnetometers fit this profile well. Indeed, it has already been demonstrated by the so-called [SQUID]^2 system (Superconducting QUantum Interference Device with Shielding QUalified for Ionosphere Detection) at LSBB, that the shielded SQUID magnetometer appears to be in a near-field configuration that has proved effective in detecting the hydromagnetic response of the ionosphere to P waves [13, 15].

As has been noted in [13] and [16], there is a need to develop a network of magnetic observatories implementing SQUID sensors for the development of complimentary space weather prediction systems and provide a broad frame of data for analysing seismo-ionospheric coupling. This research is a response to that necessity as a contribution to the Seventh Framework Project (FP7) proposal on Monitoring Space and Earth Hazards with Advanced Magnetometers (MARMOTS) – a collaborative project coordinated by the Université de Savoie, France, of which South Africa is a partner through the Department of Electrical and Electronic Engineering at Stellenbosch University and SANSA Space Science.

1.3   Outline of the Study

The origin of space weather and its effects are explained in Chapter 2, with a description of solar wind-magnetosphere interactions that account for how the geomagnetic field and the near-space environment is influenced by solar activity. The basic specifications of some magnetometers are then discussed, and this section concludes with an emphasis on the science performed by analysis of fluxgate data.

Chapter 3 takes are more in-depth look at SQUID theory, commencing with the RCSJ model through to SQUID noise. The application of SQUIDs as magnetometers introduces advanced magnetometry, that is, the analysis and interpretation of SQUID data for the purpose of investigating magnetic-seismic and seismic-ionospheric interactions. A description of the system and unique environment at LSBB is also provided, as well as an overview of the newly installed SQUID system in Hermanus.

In Chapter 4, the method of data processing with regard to spectral analysis is presented. This begins with a review on the analytic expressions for the representation of continuous signals by a Fourier series. A consistent and systematic transition is made to the discrete domain in such a way that the spectra obtained from the Fourier transform of the samples retain their physical meaning.

Based on both SQUID and fluxgate data, geomagnetic storms that occurred during 2011 are studied in Chapter 5. The analysis focuses on the frequency spectra of the data, with emphasis on identifying frequencies recurring in both datasets.

Chapter 6 concludes the study by highlighting the significance of the results obtained.

2 Conventional Magnetometry

Magnetometry and Space Weather

Magnetic sensing is important for space exploration, and monitoring of the near-space environment for space weather prediction as well as monitoring the impact of disturbances in the Earth's magnetic field. In this chapter, space weather is defined and the main drivers are discussed. We then give an overview of various magnetic sensors in use and conclude with a discussion on fluxgate magnetometers which are the most widely used sensors for monitoring the geomagnetic field.

2.1 Space Weather

Space weather is concerned with the study of how the extra-terrestrial environment interacts with the Earth, focusing on the harmful effects that threaten the performance of technology systems such as positioning systems (GPS), internet, and radio communication. The factors that dictate the state of the space environment include the solar wind, coronal mass ejections (CME's), and solar flares, all of which originate in the Sun's atmosphere. The solar wind is an extension of the Sun's *corona* into space and is responsible for "carrying" the interplanetary magnetic field (IMF) into space. Depending on the orientation of the IMF, its interaction with the Earth's magnetosphere can cause a geomagnetic storm, wherein the Earth's field is strongly perturbed and there is an increase in the amount of particle radiation within the magnetosphere due to the so-called magnetic reconnection between the IMF and the geomagnetic field. Geomagnetic storms can in turn lead to telecommunication disruptions due to undesirable changes in the ionosphere which cause frequency jamming.

2.1.1 The Sun

As our nearest star, the Sun is the primary source of energy for the support of life on Earth. This energy is generated by the nuclear fusion of hydrogen atoms into helium, and is radially emitted as electromagnetic radiation at a rate of 4×10^{26} joules of energy per second from its surface. Thus at the Sun's radius, $R_\odot = 6.96 \times 10^8$ m, the total diffuse flux leaving the surface is 6.416×10^7 W·m^{-2}. The value however falls off as the inverse of the square of the distance from the sun, such that outside the Earth's atmosphere the irradiation is 1382 W·m^{-2}. Absorption and ionization in the upper atmosphere reduces the amount of irradiation at the Earth's surface even further [17].

The structure of the Sun is typically studied by highlighting four regions: the core, the radiative zone, the convection zone and the atmosphere.

i.   The *core* lies at the centre of the Sun and accounts for half its total mass as the densest region $\left(\sim 10^5 \text{ kg·m}^{-3}\right)$. It covers a radius of $0.25\,R_\odot$ and is the site where the energy-generating nuclear reactions take place. Atoms in the core exist in a fully ionized state due to a high temperature of 15×10^6 K. This ensures a sufficiently high pressure for the ions to overcome the large gravitational forces exerted on them and provides the right conditions for nuclear

reactions to take place. The fusion reaction proceeds in three stages with an overall effect of four hydrogen nuclei $(4\mathrm{H}^1)$ combining to give one helium nucleus (He^4) [17]. There is a mass difference of 4.81×10^{-29} kg $(0.029$ amu)[†] between the rest mass of the hydrogen nuclei and the helium nucleus, which translates to a net energy of 27 MeV $(4.33 \times 10^{-12}$ J$)$ associated with this reaction. Throughout the core, several such reactions take place and their rate of occurrence is largely responsible for the solar luminosity – that is, the Sun's power output.

ii. The *radiative zone* is the region responsible for transmitting the energy generated in the core to the surface via the diffusion of high energy, high frequency particles (gamma-ray photons). Scattering, absorption and reemission occur in this region over and over as the photons progressively move towards the convection zone. Typically, the radiation in the solar interior is approximated to be blackbody, so that the radial photon flux can be given as [17]

$$F_{\mathrm{ph}} = -\frac{16}{c} D_{\mathrm{ph}} \sigma \frac{\partial T}{\partial r}, \tag{2.1}$$

where D_{ph} is the average photon diffusion coefficient, σ is the Stefan-Boltzmann constant and c is the speed of light. Without going into the details, this equation is stated here to show that the diffusion transport of energy in the core and radiative zone is a function of r, going as the temperature gradient $\partial T / \partial r$ [17].

iii. In the *convection zone*, the temperature gradient is not sufficient to aid energy transport beyond a radius of $0.7R_\odot$ since T drops rapidly as r approaches $R_\odot$. Thus the means of energy transport in the outer part of the solar interior is by convection currents of gas due to buoyancy forces. The evidence of convection is in the granular structures of various sizes which have been observed in the Sun's atmosphere. Energy transport by the movement of the so-called convection cells, either upwards or downwards, is adiabatic and thus governed by an adiabatic temperature gradient [17]

$$\left(\frac{dT}{dr}\right)_{\mathrm{ad}} = -\frac{\gamma-1}{\gamma} \frac{1}{\tilde{R}} \frac{dU_{\mathrm{grav}}}{dr}, \tag{2.2}$$

where $\tilde{R}$ is the gas constant, $\gamma = C_p/C_v$ is the ratio of specific heats at constant pressure and volume respectively, and U_{grav} is the gravitational potential.

Convection is possible in the convection zone because the temperature gradient due to radiation is less (more negative) than the adiabatic temperature gradient (lapse rate). This results in a convectively unstable atmosphere, whereby a parcel of air cooling at the adiabatic lapse rate is pushed up by surrounding parcels which are cooler and denser. This is called positive buoyancy [17].

iv. The surface of the Sun is called the *solar atmosphere*, and is the region from which solar radiation is emitted into space. It is the visible part of the Sun, consisting of the photosphere, the chromosphere, the transition zone and the corona. The photosphere is the closest region to the convection zone and is largely responsible for the radiation of the solar luminosity into space at a temperature of approximately 5800 K. The outermost part is the corona which has a temperature on the order of 10^6 K. This temperature change in the solar atmosphere is not fully understood, but suffice to say that the corona is a very lightly packed region and hence rather than heating the cooler

---

[†]1 amu $\approx 1.66 \times 10^{-27}$ kg

photosphere, it is heated instead. Several Sun radii away, the temperature drops slowly as the corona extends radially into space, becoming the solar wind [17, 18].

The Sun has a highly complex magnetic field in both its origin and structure. However, it can roughly be approximated as a dipole field with a mean magnitude of 10^{-4} T on its surface [18]. Every 11 years, the polarity of this field reverses, so that the Sun has a 18 year (magnetic) cycle marked with two distinct half cycles. The half cycles in turn have two epochs called solar maximum and solar minimum [17, 19] that define the solar cycle by the varying number of *sunspots* – cooler regions ($\sim 3,800$ K) of the Sun covering a horizontal distance of $20,000$ to $40,000$ km on the surface, with strong magnetic fields of around 0.1 T. Sunspots serve as a proxy for solar activity since their appearance exhibits an 11 year cycle (Figure 2.1) and they are particularly linked to the so-called *active regions* of the Sun observed in the chromosphere and corona. Active regions are complex, arch-like magnetic structures surrounding or located above sunspots where coronal eruptions and radiation bursts (solar flares and coronal mass ejections) occur. Figure 2.2 shows a picture of an active region taken by NASA's TRACE satellite. Solar maximum corresponds to maximum sunspot number, and as this epoch is approached, the dipole field is observed to evolve into a complex, multipolar configuration as the field weakens and eventually reverses [18]. Sunspots occur in pairs that are connected magnetically in a bipolar fashion, since they are due to the appearance of a loop of flux above the solar surface [18]. Furthermore, sunspots of the same polarity most often cluster together in groups. Accordingly, the groups occur in pairs which can have complex magnetic fields and are classified according to their size and stage of evolution. Typically, sunspots last for anything from a few hours to several days. Their average position varies over the course of the solar cycle from mid-latitudes to the solar equator [17], with average sunspot numbering ranging from below 20 at minimum to over 100 at maximum. Counting from 1755 when sunspot number was first recorded, we are currently in solar cycle[‡] 24 which began in December 2008. Sunspot number is expected to peak early in 2013.

Another feature of solar activity typifying solar maximum is the increased frequency of bursts of high energy particles and extreme ultraviolet (EUV) and x-ray radiation from the corona called *solar flares*. As much as 10^{25} J of energy are associated with solar flare events. Typical electron and nucleon energies are tens of mega-electronvolts and hundreds of mega-electronvolts, respectively. The space weather effects of this are two-fold: first, the high energy particle radiation can damage satellites by deep electric charging that causes electronic components such as field-effect transistors (FETs) to malfunction. Such high levels of radiation pose a serious health risk to astronauts. In the second place, the intense particle and electromagnetic radiation leads to increased ionization in the Earth's upper atmosphere with the potential to cause jamming of radio transmissions [19]. At times, geomagnetic storms can occur due to solar flare eruptions directed towards the Earth [18].

[‡] Take note that though a full solar cycle is 22 years, the nomenclature is such that solar cycles are counted according to the sunspot number in half cycles, that is, 11 years on average.
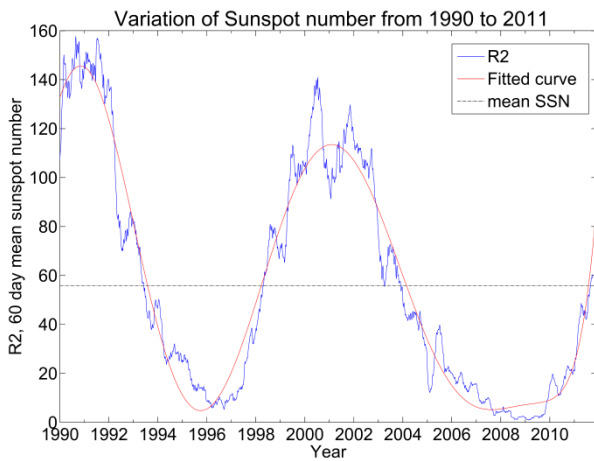
Figure 2.1: Sunspot number (SSN) plotted for a 21-year duration, averaged every 60 days. Mean SSN for the duration is shown by the horizontal line at 55. The red curve is a polynomial fitted to the data. (Data from the Space Physics Interactive Data Resource (SPIDR))
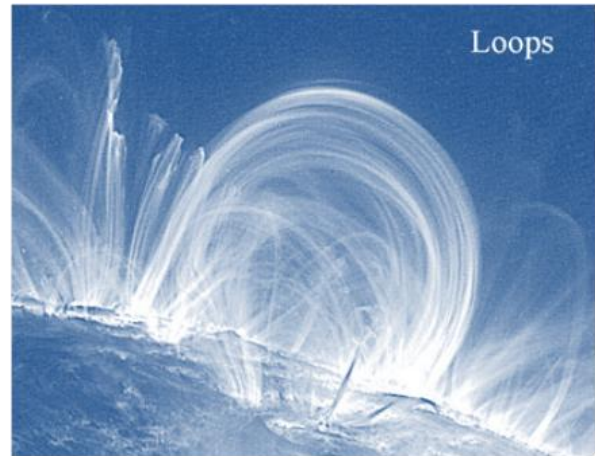
Figure 2.2: Magnetic loop structures associated with active regions. (Adapted from N. Meyer-Vernet, "Basics of the Solar Wind", pp 174)

Massive space weather disturbances are caused by the sudden ejection of coronal matter from an active region at speeds of some hundreds of kilometres per second. Believed to be caused by changes in very large magnetic fields, these explosions are called *coronal mass ejections* (CME's) and can contain as much as 10^{13} kg of coronal mass. Their energy is on the same order as solar flares, but energy transfer to particles is progressive in CME's, as opposed to instant and mostly to radiation (EUV and x-ray) in solar flares. Also, CME's produce strong perturbations in the solar wind called *shock waves*, which have dramatic effects on the Earth's magnetic field. Implications for satellites are the possibility of disorientation, loss of communication and power disruptions [17, 18, 20].

At solar maximum, CME's occur at least twice a day, while on average, they are observed once a week during solar minimum. The time of travel of an Earth-directed CME is 3 days but the effects can at times be "felt" immediately after the eruption if it is accompanied by solar energetic particle (SEP) events which travel at the speed of light. SEP's are in fact caused by pressure perturbations generated by the shock waves in the corona and solar wind at the release of a CME [21].

2.1.2   The Solar Wind and the Interplanetary Magnetic Field

The high energy of the particles in the corona as a result of its high temperature enables these particles to escape the gravitational field of the Sun, extending into space as a fast-moving stream of charged particles that fill the solar system, forming an envelope called the *heliosphere*. The heliosphere terminates at a boundary with the interstellar medium called the *heliopause*, estimated to lie at 80 − 100 AU from the sun [19]. This blowing stream of charged particles is actually a plasma – an ionized but quasi-neutral gas – which is called the *solar wind*. It possesses both magnetic and hydrodynamic characteristics and is thus called a *magneto-hydrodynamic* fluid. Consequently, the solar wind is studied extensively in the specialized field of Magnetohydrodynamics (MHD) which uses various models to account for the composition and observed behaviour of this wind as it travels throughout space [22].

At the mean Earth-Sun distance $(1 \, \text{AU} = 1.5 \times 10^{11} \, \text{m})$, solar wind speed is on average $400 \, \text{km} \cdot \text{s}^{-1}$, with proton and electron temperatures of 1.2×10^5 K and 1.4×10^5 K, while the particle density is $5 \, \text{cm}^{-3}$.

The magnetic field of the solar wind is said to be frozen-in to the plasma so that the ions travel strictly along field lines [17, 22]. With this description, the solar wind is said to carry the solar magnetic field into space. This field pervades interplanetary space and is designated the *interplanetary magnetic field* (IMF). It has a mean magnitude of 5 nT. The field components of the IMF are described by a coordinate system defined on the ecliptic plane. The component lying perpendicular to the ecliptic is denoted B_z. If B_z is oriented northward, it is said to be positive, while a southward orientation is negative, and is the condition that leads to geomagnetic storms through a process called magnetic reconnection. During reconnection, energy and mass is transferred from the solar wind into the magnetosphere.

2.1.3 The Geomagnetic Field

The Earth's magnetic field is believed to be caused mainly by electric currents generated by the dynamo action of molten iron in the outer core. It varies between $20,000$ nT and $70,000$ nT on the surface, and within a few Earth radii, it is approximated as the dipole field

$$B(\lambda, r) = \frac{\mu_0}{2\pi} \frac{M_E}{r^3} \left(1 + 3\sin^2 \lambda\right)^{1/2}, \tag{2.3}$$

where μ_0 is the magnetic permeability of free space, $M_E = 8.05 \times 10^{22} \, \text{A} \cdot \text{m}^2$ is the Earth's dipole moment, r is the distance from the centre of the Earth, and λ is the magnetic latitude. Equation (2.3) can also be written in terms of the shell parameter L as [23]

$$B(\lambda, L) = \frac{B_E}{L^3} \frac{\left(1 + 3\sin^2 \lambda\right)^{1/2}}{\cos^6 \lambda}, \tag{2.4}$$

where $L = r_{\text{eq}}/R_E$, and we have used the dipole field line equation, $r = r_{\text{eq}} \cos^2 \lambda$.

The L-value is a parameterisation of equatorial radial distance to a field line (r_{eq}) in terms of Earth radii, whereby an L-value of 4 describes magnetic field lines located at a distance of $4R_E$ from the centre of the Earth. Figure 2.3 shows a schematic of the relationship between r and r_{eq}.

As with the IMF, the geomagnetic field is monitored in a three-dimensional coordinate system with horizontal components X and Y giving the variation in north-south and east-west directions, while the vertical component is given by Z which points upward in the southern hemisphere and downward in the northern hemisphere. The resultant vector between X- and Y-components points to magnetic north and is called the horizontal field, H. By definition, it is related to X and Y through

$$H = \left(X^2 + Y^2\right)^{1/2}. \tag{2.5}$$

The angle between the true north (X) and magnetic north (H) directions is called the declination, D, given by

$$D = \cos^{-1}\left(\frac{X}{H}\right) = \sin^{-1}\left(\frac{Y}{H}\right) = \tan^{-1}\left(\frac{Y}{X}\right). \tag{2.6}$$
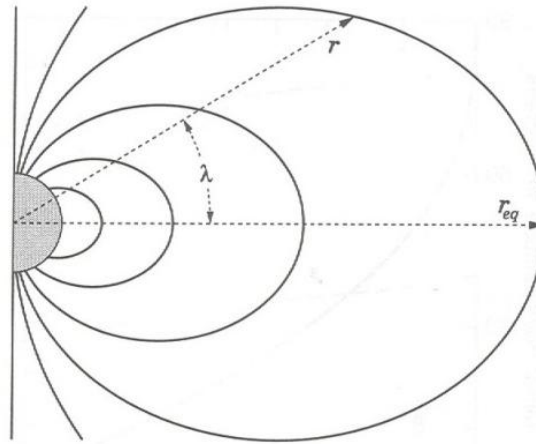
Figure 2.3: Configuration of dipolar magnetic field lines showing how r and r_{eq} are related through magnetic latitude λ. (Source: Basic Space Plasma Physics, Imperial College Press, 2004, pp 33)

The total field F is the resultant between the horizontal and vertical components, mathematically stated as

$$F = \left(H^2 + Z^2\right)^{1/2} = \left(X^2 + Y^2 + Z^2\right)^{1/2} , \qquad (2.7)$$

The angle between F and H is known as the inclination, I.

Figure 2.4 condenses the above relations for the geomagnetic field components in the southern hemisphere.

Frequently, measurements of the Earth's field are given in terms of the horizontal field H, the declination D and the vertical component Z. Conversion from the (H, D, Z) to the (X, Y, Z) system is straightforward using equations (2.5) and (2.6).
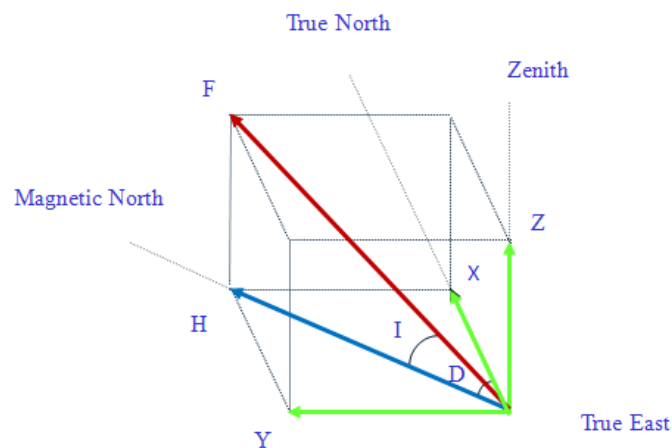
Figure 2.4: Geomagnetic field components in the southern hemisphere. (Source: SAAF Training Manual, SANSA Space Science)

The region in space bounded by the geomagnetic field is called the *magnetosphere.* It contains several plasma-filled regions, the first being the *plasmasphere* which has high populations $\left(\sim 10^9 \text{ m}^{-3}\right)$ of low-energy particles (~ 1 eV). It terminates at an L-value of about 5 at a boundary called the *plasmapause* [24].

Overlapping with the plasmasphere at $L = 1.5$ to 2.5 and $L = 4$ to 6 are two regions of trapped, high-energy particles atoms with cosmic rays, the inner belt consists mostly of protons with energies ranging from 1 MeV to more than

16

100 MeV. With such energies, the Van Allen belts pose a serious threat to spacecraft and astronauts due to the deep penetration capability of the particles. The outer belt is populated with electrons whose typical energies are on the order of $\sim 100\,\text{KeV}$ to $\sim 10\,\text{MeV}$. In addition, the lower energy particles generate a ring current around the Earth that influences the surface magnetic field. Other plasma regions include the ionosphere, the so-called magnetotail and the plasma sheet which separates the plasmasphere from the magnetotail.

The magnetosphere serves as a natural shield against most particle radiation since it deflects the solar wind around the region of its influence. The reason for the deflection lies in the fact that plasmas of different magnetic systems do not mix as a consequence of the frozen-in field condition. The surface where the solar wind plasma encounters the magnetosphere forms a boundary called the *magnetopause,* which is characterized by a bow shock in front of it. Formation of the bow shock is due to the obstruction of the solar wind's supersonic flow [25] whereby it becomes subsonic and flows around the magnetosphere [18]. A schematic of this interaction is shown in Figure 2.5. Between the magnetopause and the bow shock is a region known as the *magnetosheath*. The solar wind constantly exerts pressure on the magnetosphere and actually shapes it, compressing it on the day-side but elongating the field lines on the night side to form the magnetotail. An increase in the solar wind pressure shrinks the magnetopause and in turn causes the magnetopause current to increase. This current increase causes a sudden "jump" in the geomagnetic field, called a *sudden impulse*. If a geomagnetic storm occurs, a sudden impulse is referred to as a *sudden storm commencement* (SSC) [25].
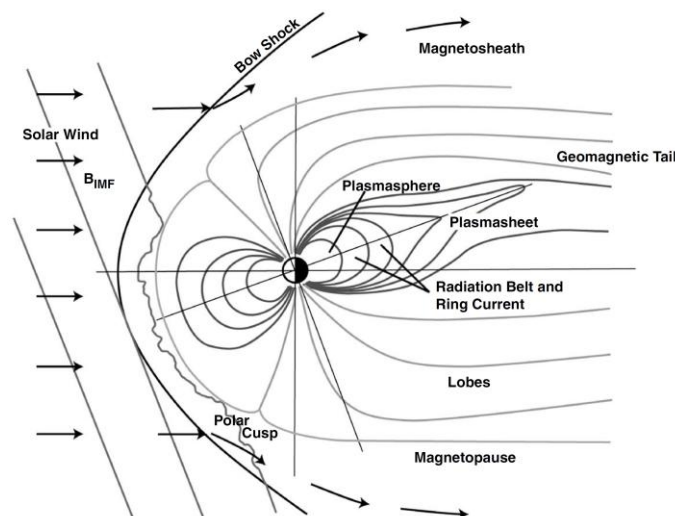
Figure 2.5: Solar wind – magnetosphere interactions in a noon-to-midnight plane. (Source: An Introduction to Space Weather, 2008, pp 52)

Charged particles moving in a magnetic field will gyrate in a circular fashion about a guiding centre – positive ions clockwise and electrons counter clockwise – due to the Lorentz force. This is defined by the gyrofrequency (cyclotron frequency), namely [26]

$$\omega_g = \frac{|q|B}{m}\,, \tag{2.8}$$

where q is the charge of the particle and m its mass, and B is the magnitude of the field.

The gyro motion has radius $r_g = v_\perp / \omega_g$, where $v_\perp$ is the component of velocity perpendicular to the applied field. If an electric field is present as well, the guiding centre will drift at a velocity given by [26]

$$\mathbf{v}_E = \frac{\mathbf{E} \times \mathbf{B}}{B^2},$$ (2.9)

where $\boldsymbol{E}$ is the electric field vector perpendicular to the magnetic field $\boldsymbol{B}$.
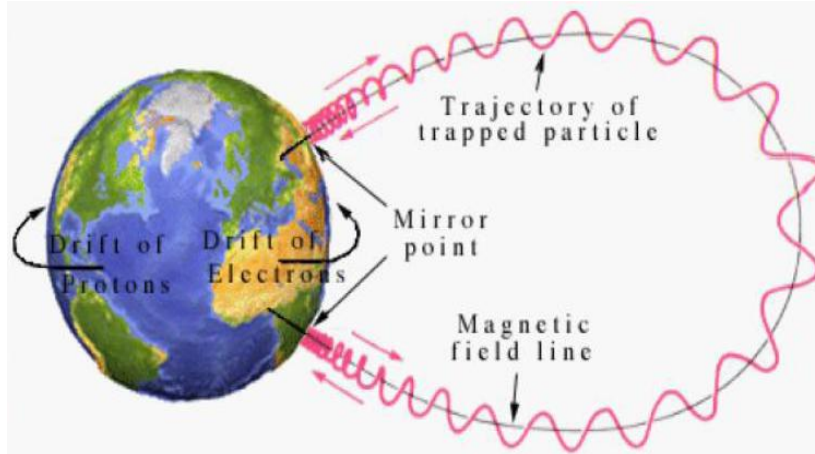
Figure 2.6: Motions of charged particles in the geomagnetic field due to the magnetic mirror effect. The trapped particles constitute the radiation (Van Allen) belts. (Source: Basic Space Plasma Physics, 1999, pp 26)

An interesting scenario arises when the magnetic field is inhomogeneous. As the particle moves into the region of stronger field, it loses parallel energy while its transverse component increases. At the point where the velocity in the parallel direction becomes zero, the particle is reflected and this is called the mirror point [25]. In the geomagnetic field which is stronger at the poles, this trapping of particles gives rise to the radiation belts – regions in the atmosphere covering an altitude of 1, 000 to 38, 000 km with a high density of energetic charged particles. The spiralling, bouncing and drifting motions of these particles along and across field lines gives rise to westward flowing *ring current* [18] illustrated in Figure 2.6.

2.1.4   The Ionosphere

The ionosphere is the partially ionized region Earth's atmosphere covering an altitude of $60 - 1000 \, \text{km}$ which is a medium for high frequency (HF) wave transmission. Ionization is typically due to EUV radiation photons "knocking out" the outer shell electrons of neutral atoms.

The ionosphere is highly variable since neither the intensity of EUV radiation nor the density of particles available for ionization atmosphere is constant. The atmospheric constituents vary with altitude and the ionization strength decreases at lower altitudes. This gives rise to a layered ionosphere described according to the number density of ions as well as the particular ion and neutral species [25]. Ranging from about 50 to 90 km lies the D layer with a peak electron density (n_e) of around 10^7 m^{-3}. Electron density increases to about 10^{10} m^{-3} in the E layer over an altitude of 90 to 120 km while the F_1 layer ($120 - 200$ km) shows a peak density of 2.5×10^{11} m^{-3}. The F_2 layer is defined to range from 200 to 350 km and its peak electron density is about 10^{12} m^{-3} [27]. Electron density profiles are shown in Figure 2.7.

Recombination of electrons with ions at night causes the D, E and F_1 layers to vanish leaving only the F_2 region. Thus the F_2 region is the most important region for HF radio propagation. In particular, the maximum electron density and the

height at which this density occurs are the parameters of interest since the electrons are the only charged particles light enough to respond to the oscillations of radio waves [27]. This is expressed in terms of the characteristic (plasma) frequency§ as

$$\omega_p^2 = \frac{n_e e^2}{\varepsilon_0 m_e} \, , \tag{2.10}$$

where e is the electron charge, ε_0 is the permittivity of free space, and m_e is the electron mass. Equation (2.10) is more accurately called the angular plasma frequency, from which we obtain the plasma frequency [26]

$$f_p = \frac{\omega_p}{2\pi} = 8.97\sqrt{n_e} \, . \tag{2.11}$$

The frequency corresponding to the maximum electron density is called the critical frequency f_0, and for the F2 layer we have $f_0 F_2 \approx 9$ MHz for $n_e = 10^{12}$ m^{-3}. This means that if the signal being transmitted exceeds $f_0 F_2$, it simply penetrates the ionosphere [27]. The HF frequency range is $3 - 30$ MHz.
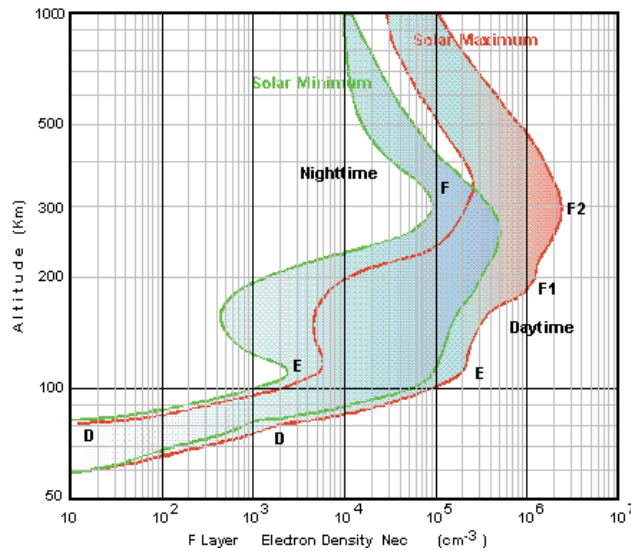
Figure 2.7: Day and night electron density profiles at solar minimum and solar maximum (Source: NASSP Aeronomy Course Manual, 2011)

A current system exists in the ionosphere which registers as the solar quiet day (S_q) variation of the geomagnetic field on the Earth's surface [27]. Solar quiet variation is unique to latitude so that the characteristic curve varies from one location to another. However, in general the variation is roughly symmetric about local noon, with a relatively smooth curve as shown in Figure 2.8. During geomagnetic storms, this smooth variation is lost which is indicative of a perturbed ionosphere. Thus the ionosphere not only shows diurnal, seasonal and latitudinal variation but varies with solar activity as well. In addition, the ionosphere is perturbed as a result of seismic events though the effects are local [28].

---

§ When ions play a significant role, we speak of the electron plasma frequency ω_p and ion plasma frequency Ω_i.
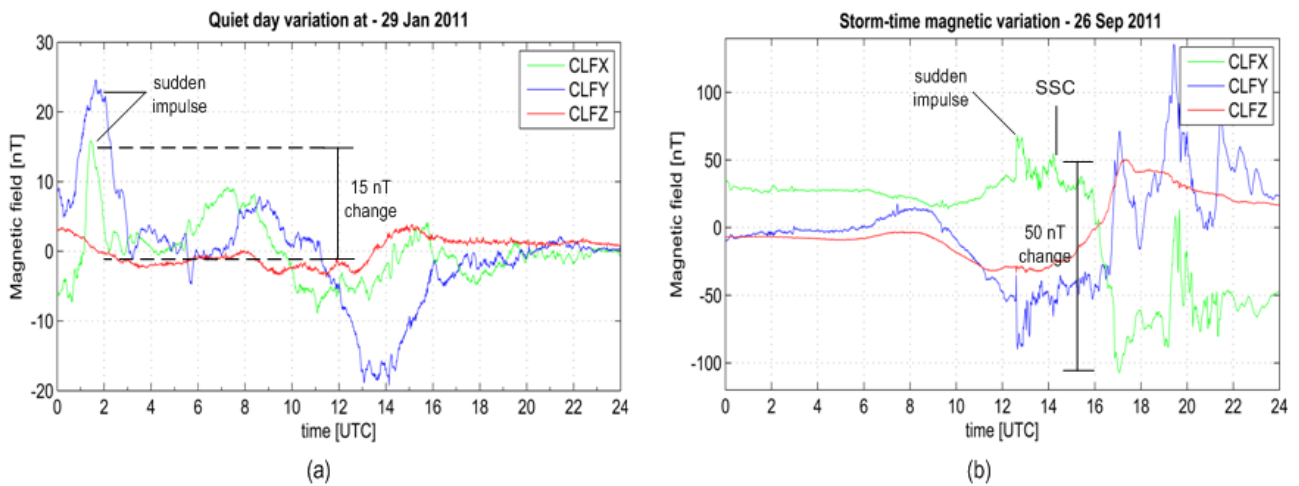
Figure 2.8: Typical solar quiet day (S$_q$) variation as observed in Chambon la Forêt, France, at latitude 48.0° north and longitude 2.30° east (a). The sudden impulse (SI) visible on both X and Y components does not distort the approximate symmetry about midday. On a magnetically disturbed day, the variation lacks symmetry (b) and shows field changes on the order of 50 nT following the sudden storm commencement (SSC) visible on the X-component.

2.1.5   Geomagnetic Storms

A geomagnetic storm can be defined as a strong perturbation of the geomagnetic field characterized by a sudden decrease in the horizontal component due to an increase in the ring current energy in the magnetosphere. Increase in the ring current is due to the injection of plasma from the magnetotail as a result of magnetic reconnection which occurs when the vertical component of the interplanetary field $\left(\text{IMF-}B_z\right)$ is oriented southward (negative). The extent of the disturbance is typically indicated by a comparison to the average deviation of the H-component on a quiet day along the equator [29]. This average fluctuation is defined as the disturbance storm time (D_{st} or Dst) index. A magnetic storm is considered intense for a decrease in the D_{st} index of 100 nT, while a 50 nT decrease indicates a moderate storm. Minor magnetic disturbances are defined by a D_{st} index of 30 nT.

Geomagnetic storms are the result of strong coupling between the solar wind and the magnetosphere. The main drivers are an increase solar wind pressure such as when there are solar flare events and CME's, and a negative IMF-B_z. Due to pressure increase, the magnetopause current rises and this is seen as a sudden increase (SSC) in the horizontal field component, followed by a strong decrease (main phase) which may last from a few hours to days as a result of the injection of magnetotail plasma into the radiation belts [18]. In the recovery phase of the storm, the magnetic field rises steadily on a time scale of typically 2 days attaining to the usual S_q variation. Less intense storms are referred to as substorms, and these usually manifest as aurora in high latitude (60 − 90°) regions [30].

2.1.6   Effects on Technology

Space weather effects threaten various technological systems directly and indirectly. These effects can be examined under the following categories: ionospheric and magnetic variations, solar radio bursts, radiation and atmospheric effects, and geomagnetically induced currents.

Since the ionosphere contributes to changes in the magnetic field, ionospheric and magnetic perturbations are normally studied simultaneously. A perturbed ionosphere leads to the loss of HF communications as a result of changes in the

refractive index of the ionosphere, which depends on its density. Strong geomagnetic fluctuations could result in a satellite becoming disorientated. Both of these effects can be driven by solar flares and CMEs. In particular, solar flares increase the number density of electrons in the ionosphere, principally in the D region, through photoionization by x-rays and EUV radiation. The result is that propagated radio waves will lose their energy by the increased collisions between electrons and neutral atoms in the D region, causing transmission failure known as shortwave fadeout (SWF) [27]. The extent of a SWF depends on the intensity and duration of the solar flare causing it. Low frequencies are most affected.

Solar radio bursts in the microwave range are frequent at times of high solar activity. They normally occur at the outset of intense x-ray and EUV radiation, increasing background noise. It then becomes difficult to propagate a signal to the ground since transmitters jam, and the high noise-to-signal ratio makes masks the signals. Transmissions to and from satellites are also affected by increased absorption and refraction in the ionosphere. Frequency prediction is thus essential during bad space weather conditions to prevent loss of communication and preserve the accuracy of information received from satellites.

Satellite life-times can also be affected drastically by particle radiation from solar flares, CME's and SEP's. High-energy particles can cause power blackouts by damaging solar panels. They also cause deep electric charging which degrades the electronics. Additionally, high-energy particles cause bulk (surface) charging which later causes abrupt discharges that are damaging to the satellite circuitry. It is mostly high altitude orbit satellites which are prone to these effects [31]. Low-Earth orbit (LEO) satellites are affected by low-energy particles that increase drag and cause damage to thermal control surfaces due to discoloration. They may also cause surface charging, and due to their own thermal energy the particles can give rise to an increase in temperature.

A remarkable space weather effect is the induction of electric currents in the ground as a result of the geomagnetic storms. These geomagnetically induced currents (GICs) have been found to cause power grids to fail to the extent that nationwide blackouts could occur [32]. Pipelines are affected by GICs in that the rate of corrosion increases due to the flow of current through the pipes. The frequency range of GICs is $0.01 - 1$ Hz.

2.2   Scalar Magnetometers

Magnetic sensing is important for space exploration, monitoring of the near-space environment and investigating various geophysical phenomena. Sensing of magnetic fields is also vital for attitude determination of air- and spacecraft, as well as for navigation of land and sea vehicles.

Magnetic sensors are classified as either scalar magnetometers or vector magnetometers depending on whether they measure only the total field or measure the components of the field, respectively. Sensors can also be classified based on their application as low, medium or high-field sensors in terms of the magnitudes of the fields being measured. A low field is typically defined as anything below 10 nT, while a medium field may range between 10 nT and 1 mT, with high fields being regarded as anything above 1 mT [33, 34]. The choice of which magnetometer is used depends on the application and associated field strengths.

2.2.1   Nuclear Precession Magnetometers

We saw in Section 2.1.3 that charged particles gyrate under the influence of a magnetic field. Due to their charge and constant motion, the behaviour of protons is likened to tiny, spinning magnetic dipole moments [35]. If a fluid containing hydrogen nuclei is exposed to a strong external field, the spin axis of the protons will become aligned to the direction of the magnetic field. In a nuclear precession magnetometer, this is achieved using a dc current through a coil winding a cylinder containing a hydrocarbon fluid. When the external field is interrupted, a torque is exerted on the protons due to the earth's magnetic field and the protons will then precess in a direction parallel to the total field of the Earth. This precession traces a circle about the direction of the dc field, generating a small, varying magnetic field. An ac current is thus induced in the coil, with a frequency in proportion to the total strength of the Earth's magnetic field [35]. The frequency of the current is precisely the precession frequency, also called Larmor frequency, and is given by.

$$f_L = \frac{B_0 \gamma_P}{2\pi} \text{,}$$

(2.12)

where B_0 is the total field of the Earth, and $\gamma_p = 2.675 \times 10^8$ $(sT)^{-1}$ is the gyromagnetic ratio.

The sensitivity range for nuclear-precession magnetometers is 10^{-2} to 10^5 nT, with a field resolution of and typical power consumption is below 0.5 W. Typical bandwidth is dc to 2 Hz. Proton precession magnetometers are used at magnetic observatories to accurately measure the total field F.

2.2.2   Overhauser Magnetometers

Similar to the nuclear (proton) precession magnetometer, the Overhauser magnetometer utilizes proton precession but with the addition of excess electrons from radical ions. The addition of electrons increases the proton polarization due to a radio frequency (RF) magnetic field by a factor of 1000. Overhauser magnetometers can attain noise levels of 0.01 nT/$\sqrt{Hz}$ at 1 Hz, and are more energy efficient and accurate than proton precession sensors [35]. Consequently, where available, they may be used in place of proton precession magnetometers for monitoring the Earth's total field with the advantage of continuous measurements. A bandwidth of up to 10 Hz is possible. Their range of sensitivity is comparable with optically pumped magnetometers.

2.2.3   Optically Pumped Magnetometers

Optical pumping is the effect of circularly polarized light (photons) in raising the energy state of electrons in an atom. Optically pumped magnetometers utilize this as well as the *Zeeman effect* – the splitting of the spectral lines of an atom into several lines corresponding to slightly different wavelengths. In caesium (Cs), which is the most widely used element for optically pumped magnetometers, there are two low energy states and one significantly higher state which its outermost electron can occupy. The lower energy states differ in energy due to a difference in spin orientation of the electrons. Thus, when the atoms of a caesium vapour are exposed to a beam, only the lower energy electrons with a spin momentum opposite the spin of the higher energy state will absorb energy and move to the higher state [35]. A schematic of the sensor's main features is shown in Figure 2.9.

The spin of the electrons can be flipped using a radio frequency field applied along the direction of the beam. Due to a change in spin, the electrons drop to either of the lower energy states. The amount of energy needed to flip the spin depends on the magnetic field strength [35].

Instead of caesium, helium (He) can also be used. The respective sensitivities are 7 MHz/mT and 28 MHz/mT, giving a sensitivity range of 10^{-3} to 10^5 nT for the sensor [35]. They are powerful scalar, earth-field sensors which detect the total field in the sensor's vicinity regardless of the orientation of the field. The major drawback of these sensors is high power consumption ($\sim$10 W). Their bandwidth is from dc to 5 Hz.
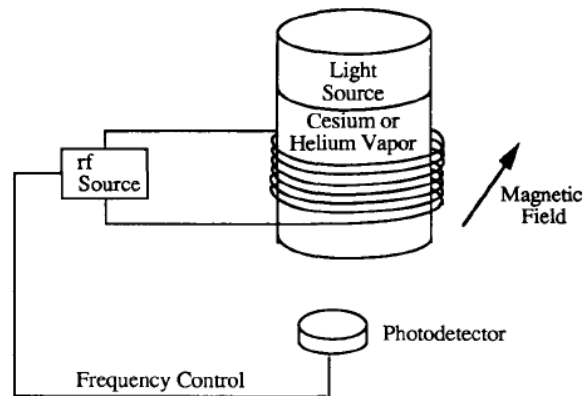
Figure 2.9: Features of an optically pumped magnetometer (Source: A Review of Magnetic Sensors, Proceedings of the IEEE, Vol. 78, 1990)

2.3   Vector Magnetometers

Vector magnetometers sense the magnitude and direction of the surrounding field. As we've seen this is important for monitoring magnetosphere-ionosphere interactions where the H-component gives an indication of the behaviour of the ionospheric ring current. Thus by monitoring the field components we can gain some insights into the mechanisms and/or processes responsible for changes in the field. This is particularly true for space exploration and space weather monitoring. One drawback of vector magnetometers is that they require specialized calibration to accurately measure field strength and direction unlike the quantum sensors discussed above whose output is inherently obtained at microscopic level [36].

2.3.1   Search-coil Magnetometer

Based on Faraday's law of induction, the search-coil magnetometer is a low-field sensor measuring fields as small as 10 nT [35]. It has a bandwidth of 1 mHz to 1 Hz which is influenced by the quality factor of the coil, that is, the ratio of inductance to resistance in the coil [37]. By using a high-permeability core, increasing the cross-sectional area and maximizing on the number of turns in the wire, the sensitivity of the coil can be improved [33, 37]. In addition, the sensitivity and frequency response of the sensor can be limited by the readout electronics [35]. The power required to operate the sensor is 1 to 10 mW.

2.3.2   Anisotropic Magnetoresistive Sensor

The anisotropic magnetoresistive (AMR) sensor is an earth field sensor that can measure both dc and vector fields. The typical sensitivity range is 10^3 to 5×10^6 nT with a bandwidth of about $1 - 5$ MHz [33, 37].

Anisotropic magnetoresistance is the direction-sensitive response of a material's resistance to a magnetic field. The change in the resistance is positive or negative according to whether the applied magnetic field is parallel or perpendicular, respectively [37]. Specifically, the resistance depends on the angle θ, between the direction of current flow and the magnetization vector in the material. This dependence is approximately $\cos^2 \theta$. A field applied perpendicular to the magnetization vector will alter the angle θ and thus change the resistance as shown in Figure 2.10. The change in resistance is typically about 2 to 3 percent. This in turn results in a change in the output voltage of the sensor [33].

The most commonly used material for the fabrication of AMR sensors is the nickel-iron alloy Permalloy, owing to a comparatively large magnetoresistance and the ease of manufacture with regard to integrated circuits [37].
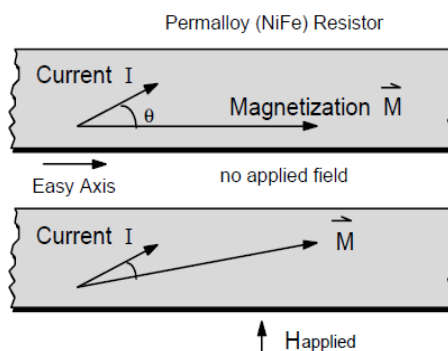
Figure 2.10: The effect of an applied field on the direction of the magnetization and current in an AMR sensor. (Source: A New Perspective on Magnetic Field Sensing, Honeywell Microelectronics and Precision Sensors)

AMR sensors have low power requirements ranging from 0.1 to 0.5 mW. Some of the well-known applications are wheel speed and crankshaft sensing for automotives, compass navigation, vehicle detection and current sensing.

2.3.3   Giant Magnetoresistance

Giant magnetoresistance (GMR) is a magnetoresistive effect in thin metallic multilayers showing changes in resistance in tens of percents due to large magnetic fields (above 1 mT). Possible bandwidth ranges from 125 Hz to over 1 MHz. The basic multilayer structure consists of a non-magnetic conductor sandwiched between two ferromagnetic metals. The principle of operation is based on the fact that the magnetization in the two ferromagnetic layers can be aligned parallel or anti-parallel, thereby switching the resistance of the structure from low to high, respectively [33]. The physical property responsible for this is electron scattering at the interfaces: the more scattering, the more collisions and the higher the resistance. This is well illustrated in Figure 2.11.

Several configurations are possible, but the highest GMR values are obtained for spin valves and spin-dependent tunnelling devices.
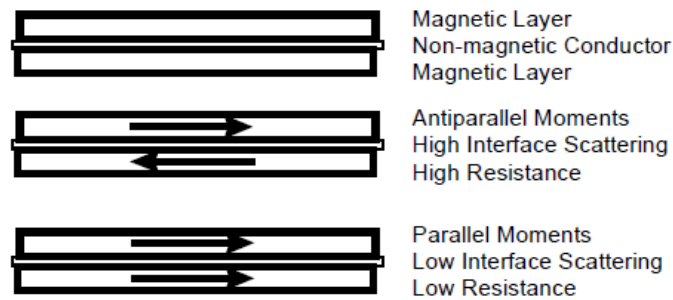
Figure 2.11: Schematic of the mechanism responsible for the manifestation of giant magnetoresistance. (Source: A New Perspective on Magnetic Field Sensing, Honeywell Microelectronics and Precision Sensors)

A *spin valve* is obtained by adding a fourth anti-ferromagnetic layer to the basic three layers in order to inhibit the rotation of the magnetization in the ferromagnetic layer adjacent to this additional anti-ferromagnetic layer. The system is then such that only one layer is allowed to rotate. This is called pinning, and the designations *hard* and *soft* are used to refer to the pinned and unpinned ferromagnetic layers, respectively [33, 37]. Materials such as nickel oxide (NiO) and ferro-manganese (FeMn) are used for the anti-ferromagnetic material. The orientation of the magnetization in the pinned layer is set by cooling the structure in a strong magnetic field [33]. Spin valves saturate at fields ranging between $10^6 - 7.5 \times 10^6$ nT and exhibit GMR values extending $4 - 20\%$. They must be operated below their blocking temperature** otherwise they become disoriented.

The *Spin dependent tunnelling (SDT) device,* also called magnetic tunnel junction (MTJ) sensor, is much like the unpinned GMR sandwich. It differs by having a very thin insulator for the sandwich material, in place of a conductor. Operation of SDT devices is based on the quantum tunnelling of electrons from one magnetic layer to the other, wherefore the orientation of the magnetization in the two layers influences the magnitude of resulting tunnelling current [36]. SDT devices saturate at fields between $\sim 10^5 - 10^7$ nT, depending on the type of magnetic layer used as well as the technique of aligning and misaligning the magnetization. Changes in resistance lie at $10 - 25\%$ [33].

2.3.4   Hall Effect Sensor

If a voltage is applied to a semiconductor material in the presence of a magnetic field at right angles to the direction of current flow, the charge carriers will be deflected by the Lorentz force to one side of the semiconductor. A voltage develops as a result of the electric field generated due to the build-up of charge. This is called the Hall voltage and it is perpendicular to both the applied magnetic field and the applied voltage.

An input resistance is obtained by Ohm's law from the applied voltage and the input current, while the Hall resistance is the quotient of Hall voltage and input current. The perpendicular component of the applied magnetic field will affect the

---

** A complete discussion on blocking temperature must include a description of the relaxation time τ – the average time it takes for the magnetization to change orientation, and the measuring technique, which influences the measuring time τ_m, of the magnetic moment. If $\tau_m < \tau$, the magnetization is seen to be fixed in one direction but will flip several times at a sufficiently high temperature. The blocking temperature is that temperature at which $\tau_m = \tau$. (*Handbook of Advanced Magnetic Materials, Volume 1*, edited by Yi Liu, et al, pp. $148 - 150$)

Hall voltage – as measured from the middle of the sides of the slab, and the Hall resistance [33]. Up to a few tesla, the response of the Hall resistance to changes in the magnetic field is linear.
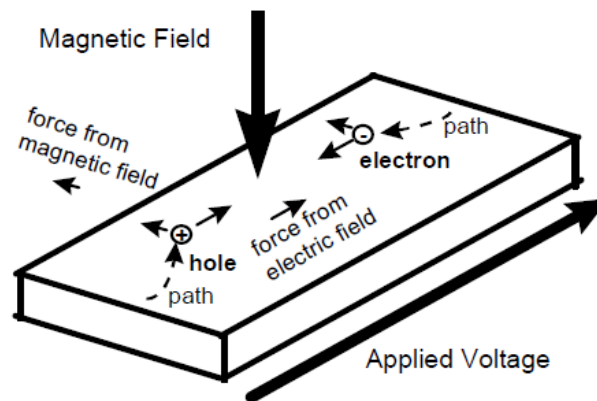
Figure 2.12: Geometry of the Hall effect in a semiconductor slab. (Source: A New Perspective on Magnetic Field Sensing", Honeywell Microelectronics and Precision Sensors)

Hall sensors are typically fabricated using n-type silicon (Si) and gallium arsenide (GaAs) due to the advantages of low cost and high efficiency, respectively [33]. Different materials and the amount of doping offer varying levels of sensitivity. Additionally, sensitivity is affected by the Hall voltage and input resistance, that in turn depend on charge carrier mobility and the Hall coefficient, both of which are temperature dependent. For silicon-built Hall sensors, the sensitivity range is $10^6 - 10^8$ nT, while InSb devices have a lower limit of 10^2 nT. In terms of bandwidth, the upper limit is 1 MHz [35]. Power consumption is 0.1 to 0.2 W.

2.4   Fluxgate Magnetometers

Fluxgates are medium (earth) field sensors with wide application as navigation, detection and geophysical sounding instruments [33]. They can measure both dc and ac fields, and are also the most widely used sensors for magnetic mapping and space-based applications [36].

The operating principle is based on magnetic induction whereby two coils are wound around the same ferromagnetic core. The primary coil supplies a driving current at a frequency between 400 Hz and 100 kHz that leads the core into a periodic, hysteretic cycle. In the presence of an external field, the core saturates faster and this difference is detected by the secondary (sense) coil [37].

Figure 2.13 demonstrates the operation of the fluxgate magnetometer. The readout involves extraction of the second harmonic from the output voltage (V_{sense}) which comprises even-numbered multiples of the driving frequency. Demodulation, filtering and rectification of the second harmonic give the value of the magnetic field [33, 37].
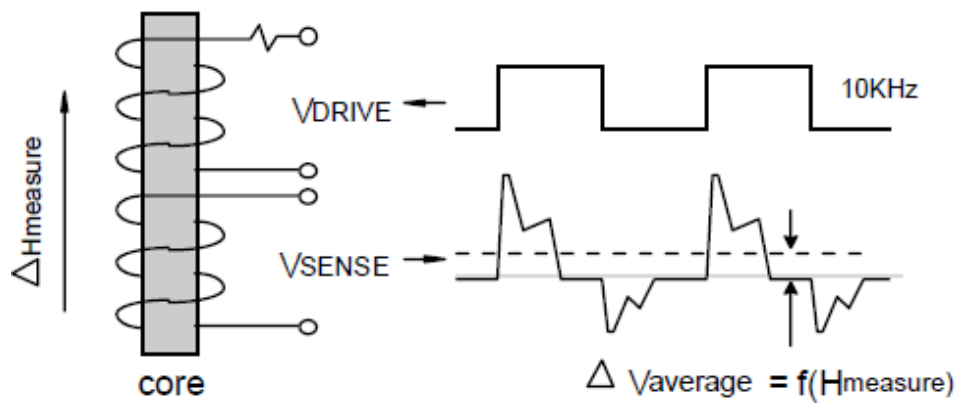
Figure 2.13: Basic operation of the fluxgate magnetometer. (Source: A New Perspective on Magnetic Field Sensing, Honeywell Microelectronics and Precision Sensors)

Fluxgate magnetometers have a wide sensitivity range of 10^{-2} to 10^{7} nT and an upper limit on bandwidth of around 10 kHz, measuring both static and varying fields. The output response per cycle per unit time is influenced by the driving source and the response time of the core material to changes in flux [35, 37].

Power consumption is on the order of 50 mW.

As mentioned above, vector sensors require calibration. For fluxgates this is best achieved using three-axis coil systems where the Earth's field is cancelled. Known fields are then applied to determine the magnetometers zero-field.

2.4.1   Ionosphere-Magnetosphere Interactions

Magnetic observatories use fluxgate magnetometers as key ground-based instruments for monitoring the geomagnetic field. They are also deployed on satellites to probe the solar wind via measurements of the IMF. The former gives information on ionosphere-magnetosphere[††] interactions, while the latter focuses on solar wind-magnetosphere coupling. As mentioned earlier, disturbed-time variations of the geomagnetic field are caused by an increase in the ring current due to injection of magnetotail plasma into the radiation belts, and are "visible" in the magnetic recordings. Analysis of storm-time data is thus a window into the behaviour of the ionosphere as influenced by the magnetosphere [30]. In fact, the D_{st} index is actually a proxy for the ring current [38]. If we wish to remove the ionosphere's influence, data from two magnetometers lying 6° from the equator on opposite sides can be subtracted. This is useful to better understand other influences driving magnetic storms.

2.4.2   Pulsations

The magnetosphere is constantly perturbed by the solar wind causing various excitations defined by their wave characteristics. One important class of such excitations are low frequency (mHz to fractions of Hz) waves called *continuous pulsations* (Pc). Since these frequencies are lower than the natural frequencies associated with the plasma, they are called ultra-low frequency (ULF) waves [39]. ULF waves are believed to be key in providing a better understanding of Sun-Earth dynamics since they appear as standing waves, revealing that there is some resonant

---

[††] The ionosphere forms part of the inner magnetosphere. We are thus distinguishing between interactions in the outer and inner regions of the magnetosphere.

process driving the excitation. Furthermore, a certain class of ULF waves called Pc5 pulsations $(2 - 7 \, \text{mHz})$ are believed to be to key players in energizing electrons within the magnetosphere and thereby driving energy transport [40]. Thus studies of ULF waves are important for space science research and are undertaken using magnetic data either from space-borne or ground-based fluxgates.

3 SQUID Magnetometry

New Perspectives on Geomagnetic Data

Sensors built as Superconductive Quantum Inference Devices (SQUIDs) are the most sensitive flux-to-voltage transducers capable of detecting changes in magnetic flux of only a few femtotesla (fT). They have a wide bandwidth extending from quasi-dc to above 1 GHz [41]. The use of SQUID magnetometers for monitoring the geomagnetic field is a new and exciting aspect of space science research with regard to investigating magneto-ionosphere and magneto-seismo couplings. The goal of this research is to work towards the development of tools to complement existing space weather prediction schemes as well as early warning systems for seismic events. In this section, key aspects of the theory pertaining to dc SQUIDs are presented, with a brief discussion on the advantages of geophysical research undertaken using SQUID data.

3.1   SQUID Theory

The dc and ac characteristics of Josephson junctions are described by equations (1.11) and (1.12), namely,

$$I = I_c \sin\varphi \,, \tag{3.1}$$

and

$$\frac{d\varphi}{dt} = \frac{2\pi}{\Phi_0} V \,. \tag{3.2}$$

As long as the junction current I does not a exceed the critical current I_c, the junction voltage remains zero. However, when $I > I_c$, the phase difference φ, of the wave functions in the two superconductors develops a time dependence which results in a voltage V, across the junction. The I-V characteristics of Josephson junctions are in general hysteretic (Figure 3.1), that is, below I_c the paths traced for increasing and decreasing bias current differ. If present, this hysteresis must be overcome for implementation in a SQUID [41]. For low-T_c SQUIDs, this is achieved by introducing an external resistance in parallel with the junction. The role of the external resistance can be understood by revisiting the resistively- and capacitively-shunted (RCSJ) model discussed briefly in Chapter 1 and shown in dc SQUID configuration in Figure 3.2. The RCSJ model is in fact the basis for most implementations of dc SQUIDs. It describes a Josephson junction as a superelectron tunnelling channel in parallel with a resistance and a capacitance. The resistance is included to account for tunnelling of normal electrons when superelectrons separate at currents above the critical current, while the capacitance is due to displacement currents arising from the separation between the two superconductors [1]. Applying Kirchhoff's law at one of the junctions results in the following differential equation in the phase difference φ [1]:

$$I - I_c \sin\varphi = \frac{\Phi_0 C}{2\pi} \ddot{\varphi} + \frac{\Phi_0}{2\pi R} \dot{\varphi} \,. \tag{3.3}$$

Equation (3.3) looks like the driven, damped harmonic oscillator equation

$$m\ddot{x} + c\dot{x} = F_d - kx \,, \tag{3.4}$$

where the first term on the left hand side is the resultant force on the oscillator, the second term is the damping (friction) force, the first term on the right-hand side is the driving force, and the last term, $-kx$, is the restoring force.
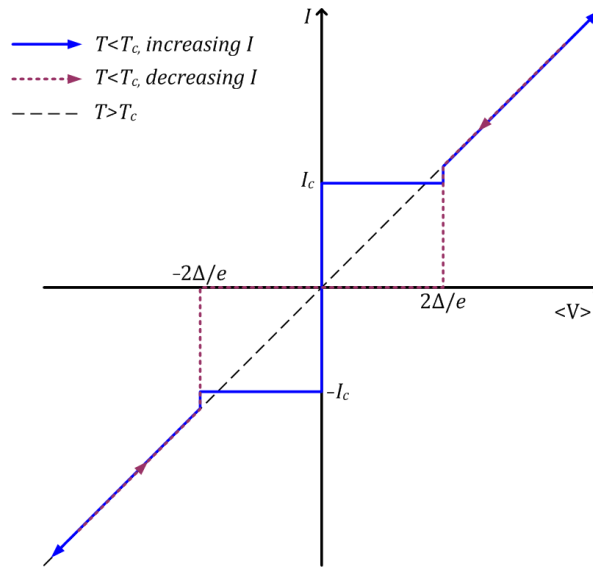
Figure 3.1: Typical I-V Characteristics of a Josephson junction at absolute zero as driven by a dc current source.
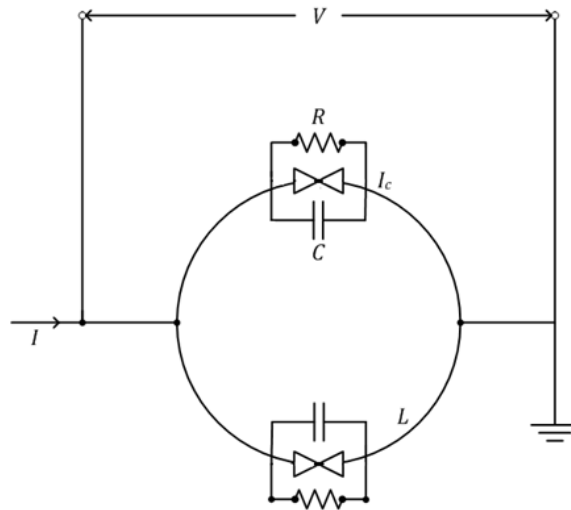
Figure 3.2: Configuration of a dc SQUID showing the self-capacitance C and internal resistance R as described by the RCSJ model. The ring has an inductance L due to current flowing through it.

The right-hand side term is related to the potential energy, U, as

$$F_d - kx = -\frac{\partial U}{\partial x} \ . \tag{3.5}$$

Thus, by analogy to (3.4) and (3.5), with $I \equiv F_d$, $I_c \sin\varphi \equiv kx$, the left-hand side of equation (3.3) can be written as

$$\frac{2\pi}{\Phi_0}\frac{\Phi_0}{2\pi}\left(I - I_c \sin\varphi\right) = -\frac{2\pi}{\Phi_0}\left[\frac{\Phi_0}{2\pi}\left(I_c \sin\varphi - I\right)\right] \equiv -\frac{2\pi}{\Phi_0}\frac{\partial U_J}{\partial\varphi} \ . \tag{3.6}$$

Hence, equation (3.3) becomes

$$\frac{\Phi_0 C}{2\pi}\ddot{\varphi} + \frac{\Phi_0}{2\pi R}\dot{\varphi} = -\frac{2\pi}{\Phi_0}\frac{\partial U_J}{\partial\varphi} \ , \tag{3.7}$$

with

$$U_J = \frac{\Phi_0}{2\pi} \int (I_c \sin\varphi - I) d\varphi = \frac{\Phi_0}{2\pi} (-I_c \cos\varphi - I\varphi + I_c) = E_J (1 - \cos\varphi - i\varphi), \tag{3.8}$$

where $i = I/I_c$ is the normalized bias current, and $E_J = I_c \Phi_0/2\pi$ is the Josephson coupling energy between the two superconducting electrodes.
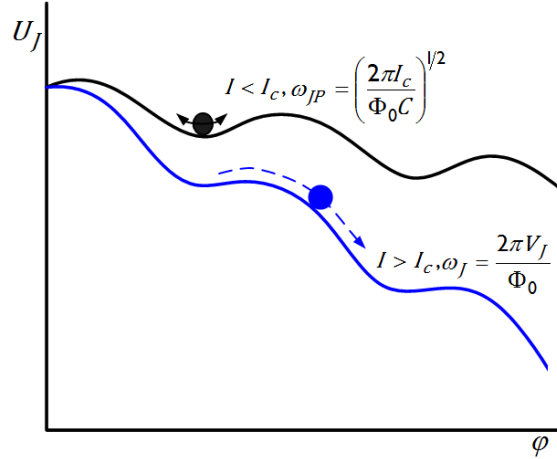
Figure 3.3: Mechanical analogue of the dynamics of a Josephson junction with respect to the effect of the biasing current I. The junction's potential is "tilted" whenever $I > I_c$ resulting in a voltage that evolves with time.

The term U_J is the *tilted washboard potential,* so-called because the junction potential "rolls off" whenever the biasing current I is greater than I_c, as shown in Figure 3.3. Using a mechanical analogue, this means that when the "driving force" I is greater than the "restoring force" I_c, a particle of "mass" C and "position" φ begins to roll down the potential and acquires "kinetic energy" (voltage) due to its motion [41]. For $I < I_c$, the particle is trapped in a potential well and there is no voltage drop across the junction. The particle does, however, oscillate with a frequency

$$\omega_{JP} = \left(\frac{2\pi I_c}{\Phi_0 C}\right)^{1/2}, \tag{3.9}$$

called the *Josephson plasma frequency*. This characteristic frequency is analogous to the undamped frequency of a harmonic oscillator, $\omega_0 = \sqrt{k/m}$, with $2\pi I_c/\Phi_0 \equiv k$, $C \equiv m$. Hence the damped frequency of the system is

$$\omega_D = \left(\frac{2\pi I_c}{\Phi_0 C} - \frac{1}{(RC)^2}\right)^{1/2} = \left(\omega_{JP}^2 - \omega_{RC}^2\right)^{1/2} = \omega_{JP}\left(1 - \frac{\omega_{RC}^2}{\omega_{JP}^2}\right)^{1/2}. \tag{3.10}$$

The damping factor can be alternatively written as

$$\frac{\omega_{RC}^2}{\omega_{JP}^2} = \frac{1}{(RC)^2}\frac{\Phi_0 C}{2\pi I_c} = \frac{1}{RC}\frac{\Phi_0}{2\pi(I_c R)} = \frac{\omega_{RC}}{\omega_J}. \tag{3.11}$$

Comparing (3.11) with (1.23), leads to

$$\beta_c = \frac{RC}{\Phi_0/2\pi V_J} = \frac{\tau_{RC}}{\tau_J} \equiv \frac{\omega_J}{\omega_{RC}}, \tag{3.12}$$

clearly shows that the damping factor in (3.10) is the reciprocal of the Stewart-McCumber parameter β_c. Hence the damped frequency can be written as

$$\omega_D = \omega_{JP}\left(1-\frac{1}{\beta_c}\right)^{1/2} . \tag{3.13}$$

The parameter β_c describes whether a Josephson tunnel junction is capacitive or resistive, or equivalently, whether it is underdamped or strongly damped. Strong damping corresponds to $\beta_c \ll 1$, in which case the capacitance of the junction is minimized, thereby removing hysteresis. This is the regime of interest for dc SQUID operation. It can be shown that $\omega_{JP} = \omega_J\sqrt{\beta_c}$ and equation (3.3) can be written as,

$$\frac{\beta_c}{\omega_J^2}\ddot{\varphi}+\frac{1}{\omega_J}\dot{\varphi} = i-\sin\varphi . \tag{3.14}$$

For the case $\beta_c \ll 1$, the equation of motion then becomes

$$\frac{1}{\omega_J}\dot{\varphi} = i-\sin\varphi , \tag{3.15}$$

for which the I-V characteristics for a dc driving source are described by

$$\left(I^2-I_c^2\right)^{1/2} = \frac{V}{R} , \tag{3.16}$$

or equivalently,

$$\left(i^2-1\right)^{1/2} = v , \tag{3.17}$$

where $i = I/I_c$, and $v = V/I_cR$.

Figure 3.4 shows the typical I-V curve for a tunnel junction under these conditions. The curve is single-valued regardless of the size of the bias current for both increasing and decreasing values. This is crucial for SQUID operation. The condition $\beta \ll 1$ means that the resistance of the junction is much more dominant than its capacitance and thus the device can be approximated as a tunnel junction in parallel with a resistance – the resistively-shunted junction (RSJ) model – which is a favourable description of high-T_c junctions. On the other hand, low-T_c devices exhibit high hysteresis and thus must be shunted with an external resistor in order to reduce the capacitive effects to ensure that $\beta \ll 1$.
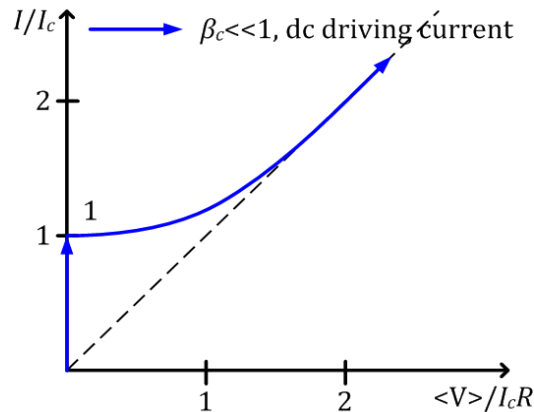
Figure 3.4: *I-V* **curve of a Josephson junction with a dc driving current for** $\beta \ll 1$ **and time-averaged voltage. No hysteresis is observed.**

3.1.1   SQUID Noise

Noise in SQUIDs can be classified in two broad categories, namely white (random) noise and $1/f$ (flicker) noise. White noise is primarily due to thermal motions while $1/f$ noise is caused by fluctuations of I_c. Flux hopping contributes to both white noise and $1/f$ noise.

3.1.1.1   White Noise

Thermal motions in the shunt resistance give rise to current fluctuations which may obscure or distort the SQUID output. This Johnson-Nyquist noise has a current spectral density given by [41]

$$S_I(f) = \frac{4k_B T}{R}, \tag{3.18}$$

where k_B is the Boltzmann constant. Clearly, this noise depends only on temperature since R is constant for a particular junction. Flux fluctuations driven by the thermal motion of vortices are characterized by the spectral flux density, S_Φ. These two noise densities give rise to voltage fluctuations across the SQUID defined by the voltage spectral density

$$S_V(f) = 4k_B T R. \tag{3.19}$$

However, since the voltage density is easier to characterize, the flux noise density is instead defined by the voltage noise as

$$S_\Phi = \frac{S_V}{V_\Phi^2}, \tag{3.20}$$

where $V_\Phi = |\partial V / \partial \Phi_a|$ is the SQUID transfer function. An important quantity related to the flux power density is the magnetic field power density $S_B(f)$ from which we obtain the *field resolution,* that is, the root mean square flux noise – the parameter determining SQUID magnetometer sensitivity, namely $\delta B = [S_B(f)]^{1/2} = [S_\Phi(f)]^{1/2}/A_{\mathrm{eff}}$ [42]. Here A_{eff} is the effective area of the SQUID over which flux is captured. Under optimal conditions [41],

$$V_\Phi \approx \frac{2I_c R}{\Phi_0} = \frac{R}{L}, \tag{3.21}$$

and the voltage noise power density can be estimated as [43]

$$S_v = 16k_B T R, \tag{3.22}$$

so that $S_\Phi = 16k_B T L^2 / R$ and

$$\delta B = \left[\frac{k_B T}{R}\right]^{1/2} \cdot \frac{4L}{A_{\mathrm{eff}}}. \tag{3.23}$$

As can be seen, the root-means-square (rms) noise and hence the sensitivity depends on the inductance and the effective area of the SQUID, which in turn depend on the geometry of the circuit [42].

Another important figure of merit related to the flux noise density is the energy resolution, $\varepsilon = S_\Phi/2L$, which is a characterization of the white noise due to flux hopping. Equation (3.23) can thus be expressed in the form

$$\delta B = \frac{\sqrt{2\varepsilon L}}{A_{\mathrm{eff}}}, \tag{3.24}$$

where optimization is in terms of the energy resolution. SQUID sensitivity is thus limited by the amount of white noise.

Spectral noise reduces the measured critical current of the junction since large T decreases the Josephson coupling between the two superconductors [41]. The prevalence of noise is described by the so-called noise parameter Γ, which is the ratio of the thermal energy to the Josephson coupling energy, namely

$$\Gamma = \frac{k_B T}{I_c \Phi_0 / 2\pi} = \frac{2\pi k_B T}{I_c \Phi_0} . \tag{3.25}$$

When $\Gamma \ll 1$, Josephson coupling is preserved resulting in low junction noise. The current and voltage fluctuations are typically Gaussian white noise with a zero mean and must be incorporated in the equation of motion as [41]

$$\frac{\beta_c}{\omega_J^2} \ddot{\varphi} + \frac{1}{\omega_J} \dot{\varphi} = i + i_N(t) - \sin\varphi , \tag{3.26}$$

where $i_N(t) = I_N(t)/I_c$ is normalized noise current. The presence of $I_N(t)$ means that the total current can exceed I_c even when the bias current I is less than I_c. This tends to "smooth" the value of I_c so that it no longer transitions to the finite voltage state sharply. Figure 3.5 shows simulated I-V curves for the RSJ model for different values of Γ. As can be seen, Josephson coupling is at a minimum for $\Gamma = 1$.
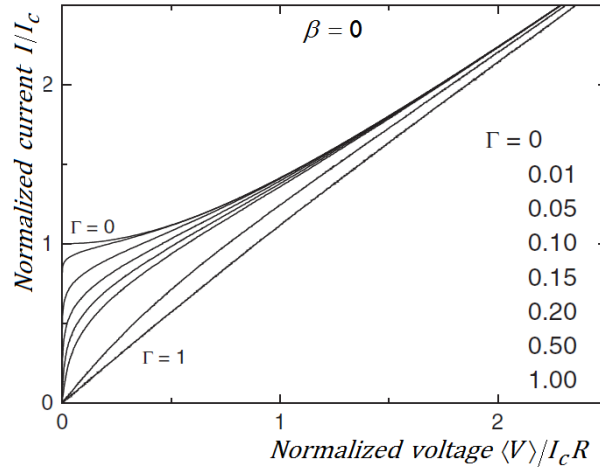
Figure 3.5: The effect of thermal noise on critical current. As $\Gamma \rightarrow 1$ normal electron tunnelling is dominant since Josephson coupling diminishes. (Picture adapted from The SQUID Handbook, Volume I, page 39)

The noise parameter can also be viewed as the ratio of a thermal current, $I_{th} = 2\pi k_B T / \Phi_0$, to the critical current I_c. At 4.2 K, $I_{th} \approx 0.18\ \mu A$, while $I_{th} = 3.23\ \mu A$ for $T = 77$ K [41]. If I_c is less than these respective values of I_{th}, Josephson coupling is weak resulting in high noise. Large coil inductance also contributes to noise by masking the macroscopic quantum mechanical effects. Accordingly, the SQUID self-inductance L must be less than the thermal inductance $L_{th} = \Phi_0^2 / 4\pi k_B T$. These two inductances are related to the noise parameter as [44]

$$\frac{L}{L_{th}} = \frac{4\pi k_B T L}{\Phi_0^2} = \Gamma \beta_L < 1, \tag{3.27}$$

where $\beta_L = 2L I_c / \Phi_0$ is the inductance parameter which is an indicator of the extent of magnetic hysteresis. The self-inductance is thus limited to the small values of $6\ \text{nH}$ and $320\ \text{nH}$ at temperatures of $4.2\ \text{K}$ and $77\ \text{K}$, respectively [44]. Typically, optimization requires $\beta_L = 1$.

3.1.1.2   Flicker Noise

Low-frequency noise with a spectrum that varies inversely with frequency is called flicker or $1/f$ noise. It is most prevalent in high-T_c sensors due to fluctuations of the critical current I_c, and random hopping of flux from vortex to vortex [41]. Fluctuations of I_c are driven by the inhibited motion of electrons as they tunnel across the insulating barrier [41]. The inhibition is as a result of the trapping of electrons in defects, which changes the local potential and hence the critical current I_c, in that region. Upon release, an electron continues to tunnel causing I_c in the vicinity of the defect to change again. The overall effect of this intermittent capture and release of electrons at defect locations generates a so-called *random telegraph signal* (RTS) – a haphazard switching between two states – that leads to variations in the junction current I_c. Trapping is minimized in high quality junctions.

Flux hopping also generates a RTS which results in *flux noise.* High-T_c SQUIDs cooled in a nonzero field particularly suffer from high flux noise having a dominant $1/f$ characteristic at low frequency. Thus to avoid formation of vortices, it is important to cool the SQUID in a shielded environment [41, 44]. However, where the device is meant to operate in the ambient field, slots can be made in the SQUID washer during fabrication. In this fashion, the flux trapped within the device pervades these slots rather than the film to prevent development of additional pinning sites [44]. The presence of $1/f$ flux noise in high-T_c SQUIDs is greatly reduced in high quality films.

3.1.2   DC SQUID Operation

Assuming identical junctions, the zero-voltage current of a dc SQUID is given by equation (1.18) as

$$I_{cs} = 2I_c \left| \cos \frac{\pi \Phi}{\Phi_0} \right|,$$
(3.28)

and has maxima whenever Φ/Φ_0 is an integer, that is whenever the total flux Φ is a multiple of Φ_0. Thus the flow of this critical current across the SQUID ring is periodic in Φ_0 and is modulated between $2I_c$ and 0 by the flux trapped within the ring. The inductance parameter β_L affects the "depth" of modulation as shown in Figure 3.6, and hence is also known as the screening parameter.

Here, $\Phi = \Phi_a + LJ$, where Φ_a is the applied flux, L is the inductance of the ring, and J is the circulating current. Since L is typically small, it is common to take $\Phi \approx \Phi_a$.
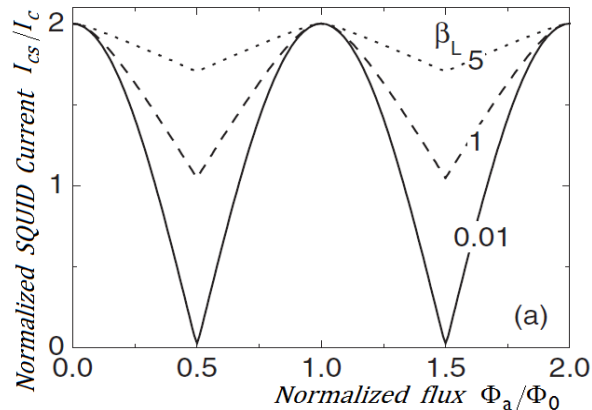
Figure 3.6: Effect of the inductance (screening) parameter β_L on the SQUID critical current. Large values of β_L decrease the critical current which results in higher junction noise. (Adapted from The SQUID Handbook, Volume I, page 48)

The overall dynamics of the SQUID are given by the total current flowing through the loop,

$$I = 2I_c \cos\frac{\pi\Phi_a}{\Phi_0} \sin\left(\varphi_1 + \frac{\pi\Phi_a}{\Phi_0}\right) + \frac{\Phi_0}{2\pi R/2}\dot{\varphi}_1 + \frac{2\Phi_0 C}{2\pi}\ddot{\varphi}_1, \tag{3.29}$$

as well as the overall phase difference of the respective wave functions, [41]

$$\varphi_1 - \varphi_2 = \frac{2\pi}{\Phi_0}\Phi = \frac{2\pi}{\Phi_0}(\Phi_a + LJ) \approx \frac{2\pi}{\Phi_0}\Phi_a. \tag{3.30}$$

Equations (3.25) and (3.26) are obtained using the RCSJ model for a circuit arrangement as in Figure 3.7, with self-inductance L and circulating current J, induced by the applied field. Since the SQUID acts as a flux-to-voltage converter, a small change in flux, $\delta\Phi_a \ll \Phi_0$, is read out as the voltage change [41]

$$\delta V = V_\Phi \delta\Phi_a, \tag{3.31}$$

where the flux-to-voltage transfer coefficient is maximized as regards voltage modulation and applied flux as

$$V_\Phi = \left|\frac{\partial V}{\partial\Phi_a}\right|_{\text{max}}. \tag{3.32}$$

The applied flux is typically chosen to be $(2n+1)\Phi_0/4$. Under optimized conditions, the transfer function can be estimated to be [42]

$$V_\Phi = \frac{\partial V}{\partial\Phi_a} \approx \frac{2I_c R}{\Phi_0}\frac{1}{1+\beta_L}, \tag{3.33}$$

which depends only on intrinsic junction parameters. If $\beta_L \approx 1$, then $V_\Phi \approx I_c R/\Phi_0$. Typical values range between 10 and 100 μV/Φ_0 [41].
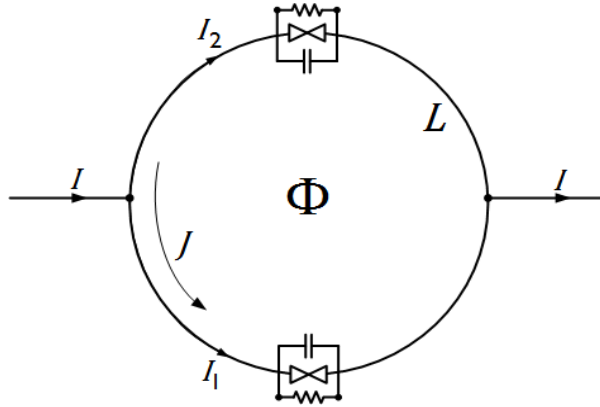
Figure 3.7: DC SQUID configuration with the tunnel junction shown according to the RCSJ model.

Equation (3.29) is much like the equation of motion for a single junction except with half the resistance and twice the capacitance, and a critical current I_{cs} as in equation (3.28). Hence the current-voltage characteristics are given by [41]

$$V = \frac{R}{2}\left(I^2 - I_{cs}^2\right)^{1/2}. \tag{3.34}$$

Since $I_{cs} = 0$ for $\Phi_a = \Phi_0/2$, and $I_{cs} = 2I_c$ when $\Phi_a = 0$, the peak to peak SQUID voltage is

$$V_{pp} = V(\Phi_0/2) - V(0) = \frac{IR}{2} - I_c R\left[\frac{I^2}{4I_c^2} - 1\right]^{1/2} (\mu V). \tag{3.35}$$

Maximizing the transfer coefficient ensures that the SQUID is operated within the linear region of its V-Φ_a characteristic. However, this linearity holds only for small changes in the applied flux $\delta\Phi_a$ around the optimum working point W which is ideally the steepest point of the V-Φ_a curve [41] as illustrated in Figure 3.8. The SQUID response is linear only over the region of W defined by [41]

$$\Phi_{\text{lin}} = \frac{V_{pp}}{|V_\Phi|},$$
(3.36)

which is approximately Φ_0/π for sinusoidal V-Φ_a as shown in Figure 3.8. For practical applications a much wider linear region is required. This is achieved by using a feedback circuit that amplifies V_{pp} and uses it in a feedback coil to generate a flux that counters the applied field, so that the flux in the SQUID loop is *locked* at zero. This negative feedback mechanism is called a flux-locked loop (FFL). A circuit model is shown in Figure 3.9. Normally, the feedback resistance R_f is in the kΩ range in order to dampen resonance in the coil. The preamplifier contributes a flux noise, $S_{\Phi,\text{amp}}^{1/2}$, on the order of 10^{-5} $\Phi_0/\sqrt{\text{Hz}}$, while the intrinsic dc SQUID noise is typically 10^{-6} $\Phi_0/\sqrt{\text{Hz}}$. In readout schemes involving flux modulation, the transfer function is increased by including a step-up transformer before the preamplifier in order to minimize the effect of the preamplifier noise since $S_{\Phi,\text{amp}} = S_{V,\text{amp}}/V_\Phi^2$ [41].

Preamplifier noise can also be reduced by using a feedback scheme known as additional positive feedback (APF), which is useful for minimizing the amplifier noise where direct readout schemes are desirable [41]. FFL circuits also normally include bias current reversal schemes to suppress $1/f$ noise caused by critical current fluctuations [41]. Low-T_c SQUIDs are biased with a static current while high-T_c SQUIDs are biased with an ac current.
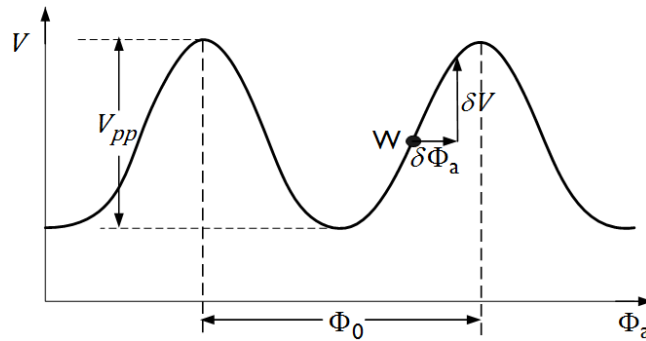
Figure 3.8: Basic principle of the SQUID readout in terms of a sinusoidal V-Φ_a characteristic.

As already seen in equation (3.23), increasing the area of flux capture improves the sensitivity of the SQUID. However, increasing the SQUID loop area increases the inductance. A better way to achieve larger flux capture area is by coupling a pickup loop to the SQUID loop [41]. Figure 3.10 shows a schematic of this arrangement. With the field-to-flux conversion efficiency, $B_\Phi = \Phi_0/A_{\text{eff}}$, where A_{eff} is the effective area of the SQUID loop, equation (3.24) becomes [41]

$$\delta B = \sqrt{2\varepsilon L}\,\frac{B_\Phi}{\Phi_0},$$
(3.37)

where $B_\Phi \equiv \partial B/\partial\Phi$ is the magnetic field sensitivity in nT/Φ_0.
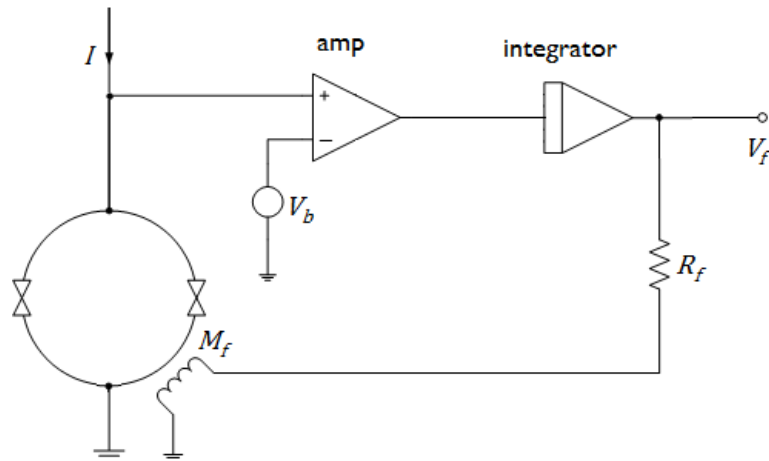
Figure 3.9: Basic flux-locked loop (FFL) circuit for a directly coupled SQUID. V_b **is the voltage at the working point and** V_f **is the voltage drop across the feedback resistor** R_f**, linearly proportional to** Φ_a**. The feedback coil is magnetically coupled to the SQUID loop as given by the mutual inductance** M_f**.**
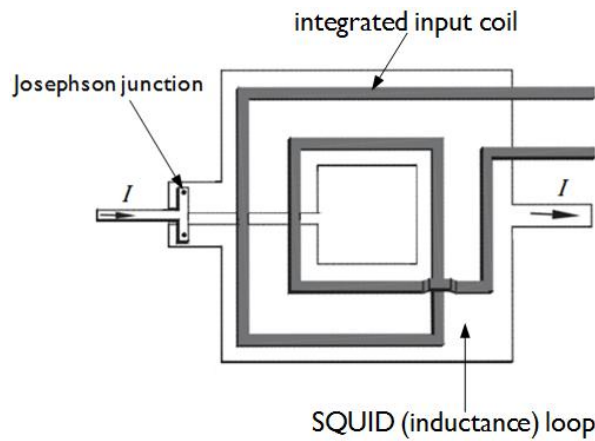
Figure 3.10: Basic configuration of a coupled dc SQUID showing only two turns of the input coil with the SQUID loop shaped as a square washer. This configuration has a flux-focusing effect whereby the flux capture area is increased without increasing the inductance. In particular, the inner dimensions of the washer are kept small. (Adapted from The SQUID Handbook, Volume I, page 177)

The value of B_Φ is heavily dependent on device parameters such as the dimensions of the chip, which influences the inductance.

Denoting pickup loop inductance as L_p, the overall inductance of input coil as $L_{i,\mathrm{eff}}$, the mutual inductance of the input coil and SQUID loop as M_i, and $A_{p,\mathrm{eff}}$ designated for the effective area of the pickup loop, The magnetic field sensitivity is given by [41]

$$B_\Phi = \frac{\left(L_p + L_{i,\mathrm{eff}}\right)\Phi_0}{M_i A_{p,\mathrm{eff}}}.$$

(3.38)

A high magnetic field sensitivity of $0.83\,\mathrm{nT}/\Phi_0$ is achieved for devices having a $7.75\,\mathrm{mm} \times 7.75\,\mathrm{mm}$ loop with $L = 190\,\mathrm{pH}$. Root mean square magnetic field noise of these SQUID magnetometers was reported to be $1.4\,\mathrm{fT}/\sqrt{\mathrm{Hz}}$ at 1 kHz [41].

3.2   Applications of SQUID Sensors

SQUID sensors are very versatile due to their high sensitivity and wide bandwidth which favour their use in a wide variety of disciplines. Biomagnetic applications focus mainly on magnetocardiography (MCG) and magnetoencephalography (MEG), which are concerned with magnetic signals of the heart and brain, respectively. The respective amplitudes are typically tens of femtotesla (fT) for MEG and tens of picotesla (pT) for MCG, spanning frequencies from 1 kHz down to few mHz [45, 46]. In both applications, shielding is generally required and it is best to operate the sensor as a gradiometer as opposed to a magnetometer, to escape environmental noise with amplitudes of about 1 μT to 1 nT [45]. SQUIDs are also used in nondestructive evaluation (NDE) for the detection of flaws in materials as well as structures such as bridges and aircraft bodies [44]. SQUID sensors have also shown superiority in geophysical sounding for the locating of minerals or anomalies in the Earth's crust [47].

Another geophysical application of SQUIDs is in the long term monitoring of the geomagnetic field for the study of magneto-ionospheric and magneto-seismic interactions. This application makes full use of the high sensitivity and wide dynamic range of SQUIDs in being able to detect both the large amplitude changes associated with geomagnetic storms and the faint contributions from seismic events. To the best of our knowledge, at present the *Laboratoire Souterrain à Bas Bruit* (LSBB) is the only facility that has explored this aspect of research.

3.3   The Laboratoire Souterrain à Bas Bruit (LSBB)

3.3.1   General Environmental and System Characteristics

Located in Rustrel, France, the LSBB is a former nuclear defense military base turned science facility, built into the foot of a mountain. It is a low-noise laboratory with a low-T_c SQUID magnetometer (from StarCryo Electronics) located in the former missile-launch control room (capsule), 550 m under limestone [13, 15]. Access to the capsule is via a network of tunnels along which there are six seismometer stations with one located very close to the SQUID. The capsule is made from semi-mild steel (non μ-metal‡‡) with dimensions 28 m $\times$ 8 m, and 14 mm thick [15] and is decoupled from the ground by a large shock absorber system. The three-axis SQUID magnetometer is suspended in a dewar containing liquid helium that is decoupled from the capsule floor by means of a sand box. Signals arriving at LSBB are low-pass filtered by both the rock and metal, resulting in a unique a low-noise environment with characteristics that are suitable for investigating ionosphere variations related to magnetic activity and seisms. Hence the LSBB system is actually a *Superconducting QUantum Interference Device with Shielding QUalified for Ionosphere Detection,* [SQUID][2] for short. Figure 3.11 shows a picture of the base of the mountain and a schematic of the capsule.

The LSBB is ideal for monitoring seismic activity as it lies in a seismically quiet region that reasonably approximates the global theoretical minima as highlighted in [13]. Furthermore, the unique characteristics of the environment result in a SQUID noise baseline of 2 fT/$\sqrt{\text{Hz}}$ above 10 Hz, which is just the intrinsic SQUID noise [48].

---

‡‡ A μ-metal (mu-metal) is an alloy of nickel, iron, copper and molybdenum used for magnetic shielding.
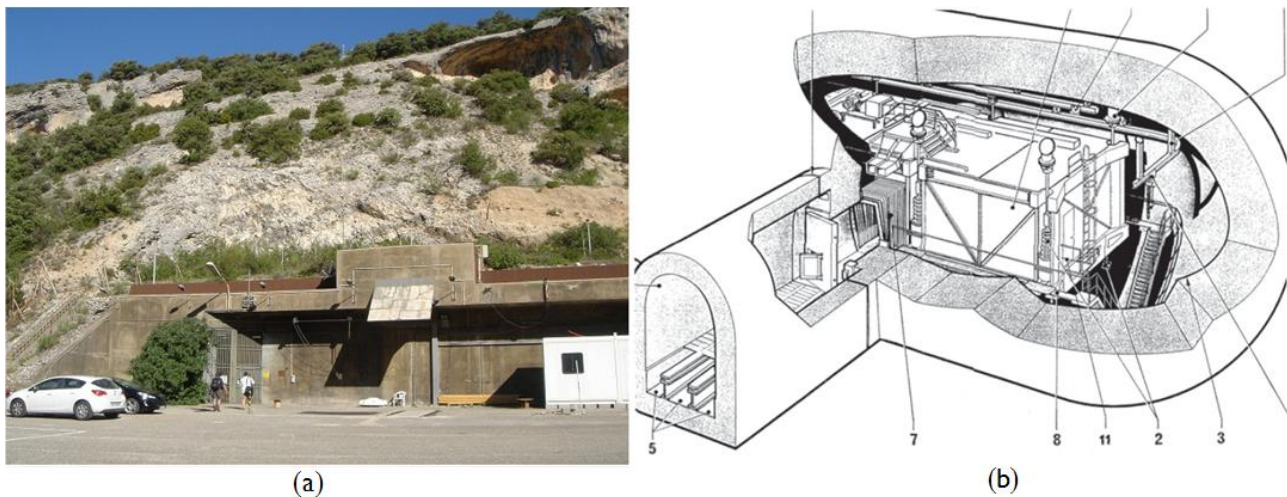
Figure 3.11: The entrance to the Low Noise Underground Laboratory (LSBB) in Rustrel, France in (a), while (b) shows a schematic of the capsule and cabin. (Figure 3.11 (b) was copied from [13])

3.3.2   Advanced Magnetometry

Studies conducted using [SQUID]² data point to a world-wide magnetic response to both terrestrial and extraterrestrial perturbations [13]. Though in a low latitude region, the data from [SQUID]² on magnetically disturbed days shows trends characteristic of high latitude regions. Moreover, magnetic fluctuations associated with seismic events have also been identified, most notably for earthquakes occurring in India (2001) and China (2008) located 6250 km and 8334 km from Rustrel, respectively. While the electromagnetic response of the ionosphere to a seism is nothing new, a near-field response to seismo-magneto signals over a bandwidth from dc to 40 Hz, as reported by the LSBB is unequalled [13, 15, 48, 49]. This outlook on geophysical interactions presents a new and exciting aspect of research involving SQUID data that has come to be referred to as *advanced magnetometry.* Advanced magnetometry is the processing and analysis of high resolution, low frequency magnetic data suitable for investigation Earth-ionosphere interactions.

The identification of earthquake precursors is an active area of research, wherein the electromagnetic effects associated with seisms are well established. These effects include changes in ground conductivity (or resistivity) prior to, during and after an event [50]; ionospheric perturbations (particularly close to the epicentre) [51, 52]; and electric field enhancements in the atmosphere [50, 53]. The difficulty lies in identifying which electromagnetic perturbations are the direct consequences of seismic activity. That is, though the associations are known and to a large degree have been characterized, real-time prediction is yet to be achieved [50]. Seismo-ionosphere coupling is made particularly complex due to the high variability of the ionosphere by its very nature. Also, not all ionospheric perturbations register a corresponding magnetic response and vice versa [52].

One of the evident advantages of advanced magnetometry is that the atmospheric response depends on currents generated in the mesopause (just below D region of the ionosphere) rather than on the ionosphere itself, so that diurnal variations are avoided. The resulting resonance is driven either by emerging P waves or a vertical electric field penetrating the atmosphere. Furthermore, the LSBB system is equipped with a network of seismometers which allows for direct comparisons between seismic and high-resolution magnetic signals arriving at Rustrel. It has been found that

the damped magnetic wave packets recorded by the [SQUID]^2 system exhibit a 300 second delay in relation to the occurrence of $M_w > 3$ earthquakes at the emergence from the ground of a P wave above the epicentre [13]. Another delay of the same length is observed upon the arrival of the P wave at LSBB. This delay is precisely the time of travel for a P wave to reach the mesopause and cause excitation. Evidence of electric field mesopause excitation has also been reported in [13]. With this unique arrangement, new strides have been made pertaining to magneto-seismo-ionosphere coupling which allude to a near-field configuration whereby magnetic precursors and signatures of seismic events can be detected over terrestrial distances. However, to realize the full potential of advanced magnetometry systems such as [SQUID]^2, it is imperative to develop a global network of such observatories [13].

3.4   The Hermanus Environment

Prompted by the research benefits that stand to be gained from a world-wide SQUID network, the Space Science Directorate of the South African National Space Agency (SANSA) installed a high-T_c SQUID magnetometer (also from StarCryo Electronics) at their facility in Hermanus, South Africa, during July/August 2012 in collaboration with the Electrical and Electronic (E&E) Engineering Department at Stellenbosch University.

Hermanus is a magnetically quiet environment with a mean magnetic field strength of 25 μT and is home to a magnetic observatory previously known as the Hermanus Magnetic Observatory (HMO) – now SANSA Space Science. This facility is part of the **Inte**rnational **R**eal-time **Mag**netic Observatory **Net**work (INTERMAGNET) and as such records high quality magnetic data to meet the INTERMAGNET specifications. Thus, SQUID data recorded in Hermanus can easily be compared to a reliable standard, which is important since SQUID magnetometers measure only the relative change in the field.

Figure 3.12: Dewar and jig pillars of the Hermanus SQUID system during the construction phase of the non-magnetic hut. The Styrofoam was laid in order to decouple the pillars from the floor and walls of the building as well as provide some damping of mechanical vibrations in the ground.

The noise baseline of the Hermanus SQUID is significantly higher than [SQUID]^2 at 150 fT/$\sqrt{\text{Hz}}$, this is still better than the fluxgate baseline of around 10 pT/$\sqrt{\text{Hz}}$ at a frequency of 1 Hz. Operated without shielding, the SQUID is housed in a non-magnetic hut, carefully built with separate pillars for the nitrogen dewar and the jig for the SQUID probes. Both pillars are decoupled from the building and from each other by laying separate foundations for the pillars "lined" with Styrofoam, so that the magnetic response is uninfluenced by the mechanical vibrations of the building. Figure 3.12

shows pictures of the pillars at foundation level. The inner and outer walls are also separated by a Styrofoam layer in order to improve the temperature stability of the hut. Pictures of the complete hut and the SQUID system are shown in Figure 3.13.

Figure 3.13: The SQUID hut at SANSA Space Science, Hermanus (a), and the set up in (b) with a close-up of the Programmable Feedback Loop (PFL-100) units in (c).

As discussed in Chapter 2, studies of the geomagnetic field are important for better understanding at solar-terrestrial interactions. SQUID magnetometers offer magnetic data with both a higher field resolution and wider frequency band pass than fluxgates. Hence the use of SQUID data for geophysical research is highly advantageous.

In spite of the fact that Hermanus is not currently equipped with a seismometer, comparisons to magnetic data at LSBB are sufficient for the interim to initiate the near-field hypothesis tests.

4 Spectral Analysis by Fourier Transforms

Fourier Analysis for Advanced Magnetometry

Magnetometry in geophysical research typically involves identifying periodicities in the data by spectral analysis. For discretely sampled data, the frequency spectrum is most commonly computed using Fast Fourier Transform (FFT) algorithms. Data from SQUID magnetometers contain information relating to a wide variety of phenomena and this is the "back-bone" of advanced magnetometry. What remains is to identify the source of the periodicities by cross-checking against solar, ionospheric and seismic data sets. This chapter presents some of the theory pertaining to time series analysis (TSA), concluding with a description of spectra from the FFT in MATLAB.

4.1 Properties of Basis Functions

A time series is a sequence of numbers arranged in chronological order and hence can be represented by sinusoidal functions. This is particularly so when dealing with a series describing or containing periodicities. Analysing a time series using harmonic analysis thus implies breaking up the function describing the series into a sum of cosines and sines [54]. Hence, these trigonometric functions, as well as the complex exponential function, are the *basis* functions of TSA, namely [55]

$$
\begin{aligned}
g_1(t) &= \cos \omega_0 t \\
g_2(t) &= \sin \omega_0 t \\
g_3(t) &= e^{j\omega_0 t} = \cos \omega_0 t + j\sin \omega_0 t
\end{aligned}
\tag{4.1}
$$

where $j = \sqrt{-1}$, $\omega_0 = 2\pi f_0$ is the fundamental angular frequency in radians per second (rad/s), and f_0 is the fundamental frequency in hertz (Hz). At the angular frequency ω_0 and its integer multiples $(k\omega_0)$, this set of functions is periodic with fundamental period $T_0 = 2\pi/\omega_0 = 1/f_0$.

A cyclic signal can be synthesized as the sum

$$
h_k(t) = \sum_{k=-\infty}^{\infty} \{a_k \cos k\omega_0 t + b_k \sin k\omega_0 t\}.
\tag{4.2}
$$

where k is an integer, and the a_k and b_k are coefficients that give the respective amplitudes of the functions. Using the identities $\cos \vartheta = (e^{j\vartheta} + e^{-j\vartheta})/2$ and $\sin \vartheta = (e^{j\vartheta} - e^{-j\vartheta})/2$, equation (4.2) can be written in the form

$$
h_k(t) = \sum_{k=-\infty}^{\infty} c_k e^{jk\omega_0 t} \ ,
\tag{4.3}
$$

where $c_k = a_k - jb_k/2$. Though c_k is in general complex, if the function h_k is real, c_k is also real.

Any trigonometric function can thus be *synthesized* as a complex exponential of the form (4.3), which is actually the *exponential Fourier series* of the signal $h_k(t)$. The *trigonometric Fourier series* expansion of $h_k(t)$ is

$$
h_k(t) = a_0 + \sum_{k=1}^{\infty} \{a_k \cos k\omega_0 t + b_k \sin k\omega_0 t\}.
\tag{4.4}
$$

Fourier series representation of a signal is made easier by the fact that cosines are even $(\cos 2\pi(-f)t = \cos 2\pi ft)$ while sines are odd $(\sin 2\pi(-f)t = -\sin 2\pi ft)$. This means an even function is synthesized using cosine terms only, while odd functions are synthesized by a sequence comprising only sines.

An important property of Fourier basis functions is orthogonality, defined by the vector product

$$\int_{-T/2}^{T/2} \sin\omega_m t \cos\omega_n \, dt = 0 \tag{4.5}$$

for all ω_m and ω_n. This result is obtained because sine and cosine functions are 90° $(\pi/2)$ out of phase with each other. For cosine-cosine and sine-sine pairs, the orthogonality relations are

$$\int_{-T/2}^{T/2} \cos\omega_m t \cos\omega_n t \, dt = \begin{cases} 0 & \text{for } m \neq n \\ T & \text{for } m = n = 0 \\ \frac{1}{2}T & \text{for } m = n > 0 \end{cases}, \tag{4.6}$$

and

$$\int_{-T/2}^{T/2} \sin\omega_m t \sin\omega_n t \, dt = \begin{cases} 0 & \text{for } m \neq n \\ \frac{1}{2}T & \text{for } m = n > 0 \end{cases}. \tag{4.7}$$

Orthogonality shows that basis functions of differing frequencies are independent of one another, such that one frequency component can be manipulated without affecting the other [55]. More importantly, frequencies corresponding to periodicity tend to have a dominant value in the Fourier transform, while non-periodic components will usually have values close to zero.

Basis functions are also harmonic§§ in nature which means that they retain their mathematical structure following a change of timescale – a useful property for manipulating periodic functions. If the time scale of a function $x(t) = \cos(2\pi ft + \phi)$ is changed from t to $u = (t - a)/b$, where a and b are constants, then [54]

$$\begin{aligned} x(t) = x(a+bu) &= A\cos(2\pi f(a+bu)+\phi) \\ &= A\cos(2\pi fbu + 2\pi fa + \phi) \ , \\ &= A\cos(2\pi f'u + \phi') \end{aligned}$$

where $f' = fb$, and $\phi' = 2\pi fa + \phi$. Clearly, even after the changing the time scale, the form and amplitude of the function remain the same. Also, if the terms in a sum of basis functions have a common frequency, the sum can be reduced to a single expression with that particular frequency.

For example [54], given the sum $A\cos 2\pi ft + B\sin 2\pi ft$, if the amplitudes are written as $A = R\cos\phi$ and $B = R\sin\phi$, the sum reduces to $A\cos 2\pi ft + B\sin 2\pi ft = R\cos(2\pi ft - \phi)$.

Manipulation of a function by Fourier analysis is also made easy because basis functions are infinitely differentiable.

---

§§ In the broader world of mathematics, a harmonic function is a twice differentiable function satisfying Laplace's equation, $\nabla^2 h = 0$ (see S. Axler, et al, *Harmonic Function Theory*, Second Edition, Dec 2000, pp 1, 25)

4.2 Fourier Analysis

4.2.1 Fourier Series

In order for a function to be represented by a Fourier series, it must satisfy the following properties known as *Dirichlet* conditions [56, 57]:

i.   It must be periodic over a given interval, satisfying the condition $h(t + T_0) = h(t)$, where T_0 is the period.

ii.   It must be continuous or piece-wise continuous on the defined interval.

iii.   It's energy must be finite over one period, namely, $\int_{-T_0/2}^{T_0/2} |h(t)| \ dt < \infty$.

Only when a function (signal) satisfies the above conditions can it be represented as the exponential Fourier series

$$h(t) = \sum_{k=-\infty}^{\infty} c_k e^{j2\pi k f_0 t} \ , \tag{4.8}$$

or the trigonometric form,

$$h(t) = a_0 + \sum_{k=1}^{\infty} \left\{ a_k \cos 2\pi k f_0 t + b_k \sin 2\pi k f_0 t \right\}, \tag{4.9}$$

where we have set $\omega_0 = 2\pi f_0$ in equations (4.3) and (4.4), with $f_0 = 1/T_0$, where T_0 is the period of the function. The a_k, b_k, and c_k are called Fourier coefficients and are given by [58]

$$c_k = \frac{1}{T_0} \int_{-T_0/2}^{T_0/2} h(t) e^{-j2\pi k f_0 t} \ dt \ , \tag{4.10}$$

$$a_k = c_k + c_{-k} = \frac{2}{T_0} \int_{-T_0/2}^{T_0/2} h(t) \cos 2\pi k f_0 t \ dt \ , \tag{4.11}$$

$$b_k = j(c_k - c_{-k}) = \frac{2}{T_0} \int_{-T_0/2}^{T_0/2} h(t) \sin 2\pi k f_0 t \ dt \ , \tag{4.12}$$

$$a_0 = 2c_0 = \frac{2}{T_0} \int_{-T_0/2}^{T_0/2} h(t) \ dt \ . \tag{4.13}$$

If the Fourier coefficients are known, they can be used to estimate a function in terms of the total average power of the signal as

$$\frac{1}{T_0} \int_{-T_0/2}^{T_0/2} |h(t)|^2 \ dt = \left(\tfrac{1}{2} a_0 \right)^2 + \tfrac{1}{2} \sum_{n=1}^{\infty} \left(a_n{}^2 + b_n{}^2 \right). \tag{4.14}$$

This result is known as *Parseval's* theorem. It must be noted here that the square of the amplitude of function in the time domain is called the power in signal processing, regardless of the units involved. In other words, signal power is seldom in watts. Here, the energy is $|h(t)|^2 \ dt$ and the *instantaneous* power is $|h(t)|^2$.

45

4.2.2 Fourier Analysis of Aperiodic Signals

Fourier series approximation of a function is limited to periodic signals. However, one seldom encounters signals with distinct periodicity. In this case, TSA (time series analysis) can be performed by Fourier transforming the function from the time to frequency domain. For a function $h(t)$, the Fourier transform is defined by [56],

$$H(\omega) = \frac{1}{2\pi} \int_{-\infty}^{\infty} h(t)e^{-j\omega t} \, dt \; . \tag{4.15}$$

For equation (4.15) to hold, $h(t)$ must be a finite energy signal as given by Dirichlet condition (iii) (Section 4.2.1). The Fourier transform is called the *analysis function* since it allows for a signal to be described in terms of its constituent frequencies. The signal can be recovered from its transform by the *synthesis function*,

$$h(t) = \int_{-\infty}^{\infty} H(\omega)e^{j\omega t} \, d\omega \; , \tag{4.16}$$

which is the inverse transform. In signal processing, the conventional representation of the analysis and synthesis equations are

$$H(f) = \int_{-\infty}^{\infty} h(t)e^{-j2\pi ft} \, dt \; , \tag{4.17}$$

$$h(t) = \int_{-\infty}^{\infty} H(f)e^{j2\pi ft} \, df \; , \tag{4.18}$$

where t is in seconds and $f = \omega/2\pi$ is the frequency in hertz. Since in practice, a signal is measured for a **finite duration**, T, the Fourier analysis relation must be expressed as

$$H(f) = \lim_{T \to \infty} \frac{1}{T} \int_{-T/2}^{T/2} h(t)e^{-j2\pi ft} \, dt \; , \tag{4.19}$$

with the inverse transform written as

$$h(t) = \lim_{T \to \infty} \frac{1}{T} \int_{-T/2}^{T/2} H(f)e^{j2\pi ft} \, df \; , \tag{4.20}$$

where we have used the property [57]

$$\int_{-\infty}^{\infty} \zeta(x) \, dx \equiv \lim_{X \to \infty} \frac{1}{X} \int_{-X/2}^{X/2} \zeta(x) \, dx \; , \tag{4.21}$$

where X is the interval of interest.

For aperiodic signals, Parseval's theorem takes the form

$$\lim_{T \to \infty} \frac{1}{T} \int_{-T/2}^{T/2} |h(t)|^2 \, dt = \lim_{T \to \infty} \frac{1}{T} \int_{-T/2}^{T/2} |H(f)|^2 \, df \; , \tag{4.22}$$

where T is a finite portion of $h(t)$ within which the function is non-zero. Parseval's theorem is thus a conservation law since the total average power contained in a signal is the same regardless of whether it is computed in the time or

46

frequency domain [59]. The term $|H(f)|^2 \, df$ is the energy contained within a small frequency band, and hence $|H(f)|^2$ is the energy spectral density (ESD) which must have units of energy/hertz (J/Hz) in a physical sense. In this particular case of magnetic signals, the units are obtained by simple dimensional analysis of the expression [55],

$$\varepsilon_h = \left| \int_{-\infty}^{\infty} h(t) \, e^{-i2\pi ft} \, dt \right|^2 = |H(f)|^2 \,, \tag{4.23}$$

where $h(t)$ is the magnetic signal in nT and ε_h is the ESD corresponding to $h(t)$. Clearly, the units of the ESD are $\mathrm{nT}^2 \cdot \mathrm{s}^2 \equiv \mathrm{nT}^2 \cdot \mathrm{s/Hz}$, where we have used $1/\mathrm{s} \equiv \mathrm{Hz}$. The signal energy then has units of $\mathrm{nT}^2 \cdot \mathrm{s}$. A more commonly used spectral quantity is the time-weighted energy spectrum, that is, the power spectral density (PSD)

$$S_h(f) = \lim_{T \to \infty} \frac{1}{T} \varepsilon_h = \lim_{T \to \infty} \frac{|H(f)|^2}{T} \,, \tag{4.24}$$

whose units are $\mathrm{nT}^2/\mathrm{Hz}$. Integration of the PSD gives average power within a frequency band as

$$P = \int_{-T/2}^{T/2} S_h(f) \, df \quad (\mathrm{nT}^2). \tag{4.25}$$

4.2.3 Convolution and Correlation

It is often useful to express one function in terms of another. This is important for most filtering techniques and is called *convolution*. It is defined mathematically as

$$g * h = \int_{-\infty}^{\infty} g(t) h(\tau - t) \, dt = \int_{-\infty}^{\infty} g(\tau - t) h(t) \, dt \,, \tag{4.26}$$

where τ is the time lag. For functions of finite duration, the convolution is written

$$g * h = \lim_{T \to \infty} \frac{1}{T} \int_{-T/2}^{T/2} g(t) h(\tau - t) \, dt \,, \tag{4.27}$$

where T is the *duration of observation* and **not** the period of either function.

The Fourier transform of a convolution is simply the product between the transforms of the two functions g and h, namely

$$\Im(g * h) = G(f) H(f) \,, \tag{4.28}$$

where $\Im$ denotes the Fourier transform. This relation is known as the *convolution theorem* and is an energy spectral density relation provided the two functions have the same dimensions. Since the frequency response of one function is known, the convolution theorem can be used to determine or manipulate the behaviour of the second function.

The statistical dependence of two functions can be computed by their correlation, defined as

$$c_{gh}(t) = \int_{-\infty}^{\infty} g(t) h(t + \tau) \, dt = \int_{-\infty}^{\infty} g(t - \tau) h(t) \, dt \,, \tag{4.29}$$

or for a finite range,

$$c_{gh}(t) = \lim_{T \to \infty} \frac{1}{T} \int_{-T/2}^{-T/2} g(t)h(t + \tau)\, dt \,, \tag{4.30}$$

Correlation is a description of the similarity in behaviour between two functions for all corresponding points in the series [60]. Equation (4.30) is sometimes called the cross-correlation between the functions g and h. The Fourier transform of the cross-correlation function gives the *correlation theorem*

$$C_{gh}(f) = G(f)H(-f) = G(f)H^*(f)\,, \tag{4.31}$$

where C_{gh} is the Fourier transform of c_{gh} and the last equality arises because $H(-f) = H^*(f)$ for real h. Clearly, the correlation theorem is also a spectral density relation given that $g(t)$ and $h(t)$ have the same units. Orthogonality will result in a small output from equation (4.31), while a large value indicates strong frequency correspondence.

Functions corresponding to stochastic processes possess infinite energy [55, 58] and as such do not have a Fourier transform. The correlation of a function with itself then becomes the quantity of interest. It is given by

$$c_{gg} = \lim_{T \to \infty} \frac{1}{T} \int_{-T/2}^{T/2} g(t)g(t + \tau)\, dt = \lim_{T \to \infty} \frac{1}{T} \int_{-T/2}^{T/2} g(t - \tau)g(t)\, dt \,, \tag{4.32}$$

and it's Fourier transform gives the ESD

$$\varepsilon_g = C_{gg}(f) = \lim_{T \to \infty} \frac{1}{T} \int_{-T/2}^{T/2} c_{gg}\, e^{-j2\pi ft}\, dt = G(f)G^*(f) = |G(f)|^2 \quad (\text{nT}^2 \cdot \text{s/Hz}). \tag{4.33}$$

from which the PSD can be obtained as in equation (4.24). This is called the *Wiener-Khintchine theorem.*

4.3   Discretely Sampled Data

A real-world, continuously varying function (physical quantity) is sensed by an appropriate system equipped with analogue-to-digital converters (ADC) so that the function is approximated by a sequence of numbers. How well this discrete data approximates the original physical quantity depends on the quality of the system and the sampling rate therein. Assuming sufficient and accurate sampling, the underlying processes and mechanisms driving the changes in the geomagnetic field – in our particular case – are easier to identify by viewing the frequency spectrum of the samples. The basic tool in achieving this objective is the discrete Fourier transform (DFT).

4.3.1   Sampling

The sampling frequency, f_s, is the reciprocal of the sampling period, Δt. Proper sampling requires that f_s be greater than the frequencies of interest. In fact, f_s imposes an upper limit on the identifiable frequency in a harmonic wave, called the *Nyquist* frequency,

$$f_N = \frac{1}{2\Delta t} = \frac{f_s}{2}\,. \tag{4.34}$$

At least two points must be sampled per cycle of the harmonic wave in order for a signal to be properly reconstructed from its samples. In other words, the Nyquist frequency must be at least twice the largest expected frequency present in a set of observations [59]. Since the observable frequencies do not exceed f_N, the transform of a continuous function

$h(t)$ must be bandwidth limited such that $H(f) = 0$ for $|f| > f_N$ [59]. If this condition is not satisfied, it is likely that frequency components that do not lie in $(-f_N, f_N)$ have been mirrored onto this range. This is called *aliasing,* which means that, two frequencies f and f' that differ by a multiple of $1/\Delta t$, are indistinguishable [59].

A more basic form of aliasing occurs due to the even and odd nature of cosine and sine functions, whereby positive and negative frequencies become identical, since

$$\begin{aligned}
\cos 2\pi(-f)t_n &= \cos 2\pi f t_n \\
\sin 2\pi(-f)t_n &= -\sin 2\pi f t_n
\end{aligned}.$$

(4.35)

Negative frequencies actually do not hold any physical meaning and may be reflected into the positive axis.

Another problem that leads to inaccurate spectrum results is the broadening of peaks whereby two neighbouring frequencies are identified as one peak. This is called *spectral leakage.* It is due to a low frequency resolution and may be addressed by increasing the duration of measurement since

$$\Delta f = \frac{1}{T} = \frac{1}{N\Delta t} = \frac{f_s}{N} \, ,$$

(4.36)

where Δf is the frequency resolution and T is the duration over which the signal is sampled. In cases where the duration cannot be increased, the frequency resolution can be increased by appending zero's (zero padding) to the samples.

4.3.2   The Discrete Fourier Transform

The Fourier transform of discretely sampled data is known as the discrete Fourier transform (DFT), given by [59]

$$H(f_k) = \frac{1}{T} \sum_{n=0}^{N-1} h(t_n) e^{-j2\pi f_k t_n} \Delta t = \frac{1}{N} \sum_{n=0}^{N-1} h(t_n) e^{-j2\pi f_k t_n} \, ,$$

(4.37)

where $f_k = k/N\Delta t$, with k an integer, and $t_n = n\Delta t$ with $n = 0, 1, \dots, N-1$, and $T = N\Delta t$. The units of the transform (4.37) are nT as can be worked out easily from the first term on the right-hand side (RHS). The DFT can be written more simply as,

$$H_k = \frac{1}{N} \sum_{n=0}^{N-1} h_n e^{-j2\pi kn/N} \, ,$$

(4.38)

while the inverse discrete Fourier transform (IDFT) is

$$h_n = \sum_{k=0}^{N-1} H_k e^{i2\pi kn/N} \, .$$

(4.39)

It should be noted that the $1/N$ factor serves as a normalization of the transform amplitude such that it is scaled to the original magnitude of the time signal.

The computation time for the DFT is determined by the square of the number of points in the sample. For large N, this calculation proceeds rather slowly. Requiring that N be a power of 2 greatly reduces computation time since the transform can then be calculated as $2 \times (N/2)^2$. For $N = 2^p$, where p is the number of points, the computation time is $N_p = N\log_2 N$. Computation of the DFT based on this principle is called the *Fast Fourier Transform* (FFT) [59].

4.3.3   Convolution and Correlation in the Discrete Domain

From equation (4.30), the correlation between two discrete signals may be written as

$$c_{gh}[n] = \lim_{T\to\infty} \frac{\Delta t}{T} \sum_{n=-T/2+1}^{T/2} g_n h_{n+m} = \lim_{N\to\infty} \frac{1}{N} \sum_{n=-N/2+1}^{N/2} g_n h_{n+m} = \frac{1}{N} \sum_{n=-N/2+1}^{N/2} g_n h_{n+m} \, , \tag{4.40}$$

where $T = N\Delta t$ is the duration of measurement, n is the sampling index, m is the lag index, and the last equality arises by extending N to infinity by zero-padding.

Since negative frequencies have no physical meaning, it is more common to write the discrete correlation function as

$$c_{gh}[n] = \frac{1}{N} \sum_{n=0}^{N-1} g_n h_{n+m} \, , \tag{4.41}$$

and the correlation theorem is simply

$$C_{gh}[k] = \sum_{n=-\infty}^{\infty} c_{gh}[n] e^{-j2\pi kn/N} = G_k H_k^* \, . \tag{4.42}$$

It easy to see that the discrete auto-correlation function is

$$c_{gg}[n] = \frac{1}{N} \sum_{n=0}^{N-1} g_n g_{n+m} \, , \tag{4.43}$$

from which we get the Wiener-Khintchine theorem,

$$\varepsilon_g[k] = C_{gg}[k] = \frac{1}{N} \sum_{n=0}^{N-1} c_{gg}[n] e^{-j2\pi kn/N} = G_k G_k^* = |G_k|^2 \, . \tag{4.44}$$

The energy density relation (4.44) gives the power density

$$S_g[k] = \lim_{T\to\infty} \frac{1}{T} \varepsilon_g[k] \equiv \frac{1}{N\Delta t} |G_k|^2 = \frac{1}{N} |G_k|^2 \, , \tag{4.45}$$

where the last equality arises by setting $\Delta t = 1$. This can be done since the sampling interval is innate in the index n.

It must be noted here that from the definition of the DFT that has been used, the ESD in equation (4.44) has units of square nanotesla $\left(nT^2\right)$ while the PSD is in square nanotesla/second $\left(nT^2/s\right)$. To obtain the correct units, both equations (4.44) and (4.45) must be multiplied by T^2, where T is the duration of measurement in seconds.

Discritizing the relation (4.27), the convolution of two discrete samples is

$$(g * h)[n] = \frac{1}{N} \sum_{n=0}^{N-1} g_n h_{n-m} \, , \tag{4.46}$$

and the convolution theorem takes the form

$$\Im(g * h)[k] = \frac{1}{N} \sum_{n=0}^{N-1} (g * h)[n] e^{-j2\pi ft} = G_k H_k \, . \tag{4.47}$$

4.3.4   Types of Spectra

A plot of the transform amplitude versus frequency gives the amplitude spectrum (AS), while the power spectrum (PS) is the square amplitude against frequency. It is often more useful to view the spectrum in terms of either the amplitude spectral density (ASD) or the PSD. The ASD of a time series g_n is simply the product $|G_k| \cdot \sqrt{T}$ in units of nT/√Hz since $\sqrt{s} \equiv 1/\sqrt{Hz}$. A log-log plot of the ASD gives the noise spectrum of the data, while the PSD is useful for determining the statistical significance of peaks in the spectrum, since the effect of squaring is to minimize small numbers while large values become more dominant. There may, however, be some large peaks present that are not due to periodicity. It is here that probability estimators such as the probability density function (PDF) become important.

The total average power is estimated by the discrete form of Parseval's theorem as

$$\frac{1}{N} \sum_{n=0}^{N-1} |g_n|^2 = \frac{1}{N^2} \sum_{k=0}^{N-1} |G_k|^2 \,.$$

(4.48)

while the PS is given by the quantity $|G_k|^2/N^2$.

Table 4.1 summarises the expressions of the various spectra with corresponding units.

Table 4.1: Summary of the spectra that can be obtained from the Fourier transform specific to magnetometry.

Spectrum	Expression	Units
Amplitude spectrum (AS)	$|G_k|$	nT
Energy spectral density (ESD)	$|G_k|^2 \times T^2$	nT^2·s/Hz
Amplitude spectral density (ASD)	$|G_k|\sqrt{T}$	nT/√Hz
Power spectrum (PS)	$\dfrac{1}{N^2}|G_k|^2$	nT^2
Power spectral density (PSD)	$\dfrac{|G_k|^2}{N} \times T^2 \equiv |G_k|^2 \times T$	nT^2/Hz

4.4   Spectral Analysis in MATLAB

The analytic solution for the Fourier transform of a signal $h(t) = \sin 2\pi ft$ is

$$H(f) = \int_{-\infty}^{\infty} h(t)e^{-j2\pi ft}\, dt = \int_{-\infty}^{\infty} \frac{3}{2i}\left\{e^{j2\pi f_1 t} - e^{-j2\pi f_1 t}\right\}e^{-j2\pi f_k t}\, dt = -\frac{3i}{2}\left[\delta(f_1 - f_k) - \delta(f_1 + f_k)\right],$$

where we have used the Dirac-delta function identity $\int_{-\infty}^{\infty} e^{\pm i2\pi ft}\, dt = \delta(f)$, where $\delta(f) = 0 \; \forall \; f \neq 0$ and $\delta(f) = 1 \; \forall \; f = 0$. Setting $f_1 = f_k$ gives

$$H(f) = -\frac{3i}{2},$$

51

The absolute value is

$$|H(f)| = \left(H \cdot H^*\right)^{1/2} = \sqrt{\left(0 - \frac{3i}{2}\right)\left(0 + \frac{3i}{2}\right)} = \frac{3}{2}.$$

Thus for any signal, the analytic solution yields an amplitude of $A/2$, where A is the amplitude of the time signal. This is because the analytic solution corresponds to a two-sided spectrum with peaks at $-f$ and $+f$. The original amplitude is recovered by folding the negative frequencies onto the positive axis. The folding must be done **before** any squaring otherwise the amplitude will be incorrect. For instance, squaring the amplitude before folding to obtain the power spectrum gives two peaks of value $A^2/4$ which give $A^2/2$ when folded. Taking the square root to get back the amplitude gives $A/\sqrt{2}$.

Transform amplitudes in MATLAB are according to the analytical result of $A/2$. The original amplitude is simply twice the FFT output. As an example, an artificial signal is generated as $x(t) = 3\sin 2\pi f_1 t + 5\cos 2\pi f_2 t$ with $f_1 = 20$ Hz and $f_2 = 50$ Hz using the following code:

```
N = 1000000; % sample length
n = 0:N-1; % time index
f1 = 20; f2 = 50; % frequencies in Hz
fs = 1024; % sampling frequency, must be a power of 2 in order to obtain correct
amplitude
dt = 1/fs; %sampling period
time = (0:dt:(N-1)*dt);

x = 3*sin(2*pi*(f1/fs)*n) + 5*cos(2*pi*(f2/fs)*n);

plot(time,x),title('Time Domain signal of {\itx} = 3sin(2{\pi}{\itf_1}{\itt}) +
5cos(2{\pi}{\itf_2}{\itt})')
xlabel('Time t [sec]'),ylabel('Amplitude [units]')

m = length(x);
Nn = 2^nextpow2(m); % transform length as a power of 2
f = (0:Nn-1)*fs/Nn; % frequency axis in Hz
X = (fft(x,Nn))/m; % transform of x
XR = real(X); % real part of the spectrum
XI = imag(X); % imaginary part of the spectrum
f2 = ((-Nn/2)+1:Nn/2)*(fs/Nn); % wrap around for negative and positive frequencies

figure
subplot(3,1,1),plot(f2,fftshift(XR))
title('Real Part of the Spectrum of 3sin(2{\pi}{\itf_1}{\itt}) +
5cos(2{\pi}{\itf_2}{\itt})')
xlabel('frequency {\itf} [Hz]'), ylabel('amplitude [arbitrary units]')

subplot(3,1,2),plot(f2,fftshift(XI))
title('Imaginary Part of the Spectrum of 3sin(2{\pi}{\itf_1}{\itt}) +
5cos(2{\pi}{\itf_2}{\itt})')
xlabel('frequency {\itf} [Hz]'), ylabel('amplitude [arbitrary units]')

subplot(3,1,3),plot(f(1:Nn/2),2*abs(X(1:Nn/2)))
title('Spectrum of 3sin(2{\pi}{\itf_1}{\itt}) + 5cos(2{\pi}{\itf_2}{\itt})')
xlabel('frequency {\itf} [Hz]'), ylabel('amplitude [arbitrary units]')
```

Figure 4.1 shows the time domain signal, while the frequency spectrum is shown in Figure 4.2. As can be seen from the real and imaginary spectral plots (a) and (b), respectively, the Fourier spectrum is two-sided with the amplitudes equally divided between negative and positive frequencies. The dominant peak in the real spectrum corresponds to the cosine

wave while the sine wave dominates in the imaginary spectrum, as expected. However, this is not useful for real functions, and hence the quantity of interest is the absolute value of the transform. Since only positive frequencies have physical meaning, in this study we take the one-sided spectrum $0 \leq f_k \leq N$ as shown in Figure 4.2(c) for the present example. The FFT output is thus taken as $2|X_k|$ giving an amplitude of the same magnitude as the original signal x_n. The one-sided is actually fully defined $0 \leq f_k \leq f_N$ since there are no frequencies higher than the Nyquist present.

Figure 4.3 is a plot of the signal $x(t)$ with the addition of Gaussian (random) white noise. White noise has a flat frequency response as shown by the ASD plot in Figure 4.4(a). The spectrum in Figure 4.4(b) was computed by taking the FFT of the autocorrelation function (Wiener-Khintchine theorem). Notice that the only peaks present are the actual frequencies in the artificial signal, namely 20 Hz and 50 Hz with their respective amplitudes.
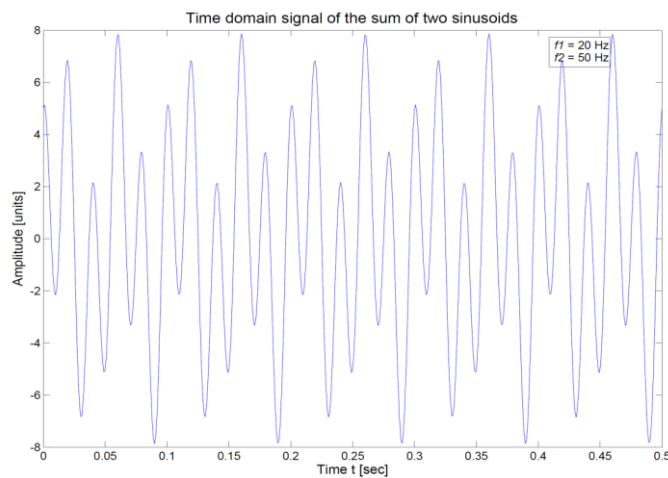
Figure 4.1: Artificial signal generated as the sum of a sine and cosine wave with frequencies 20 Hz and 50 Hz, respectively.
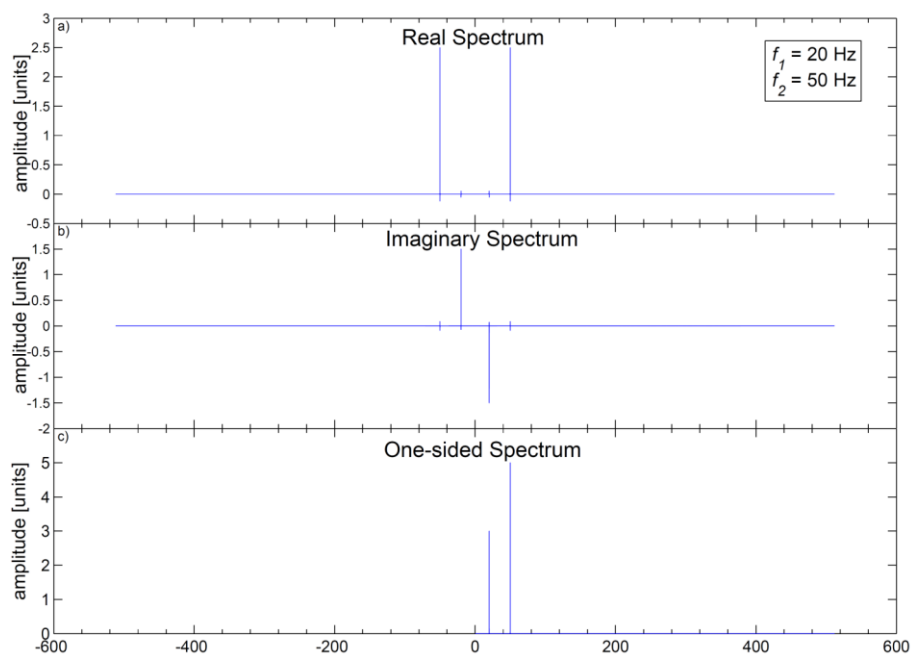
Figure 4.2: Frequency spectrum of the artificial signal $x(t)$. The real part of the spectrum in (a) is dominated by the cosine component while the sine component dominates the imaginary spectrum, as expected. In both cases the magnitude of the

53

peaks is half the original amplitude. The one-sided spectrum in (c) shows the spectrum of interest with the correct amplitudes.

Care must be taken when computing a frequency spectrum from the FFT of the autocorrelation function. In MATLAB, if a signal has length N, the autocorrelation function has length $2N - 1$ because the function is computed for positive and negative lags. This can affect the amplitudes of the resulting spectra of a signal. It is advisable to remove the values at negative lag (see code in Appendix A.3).
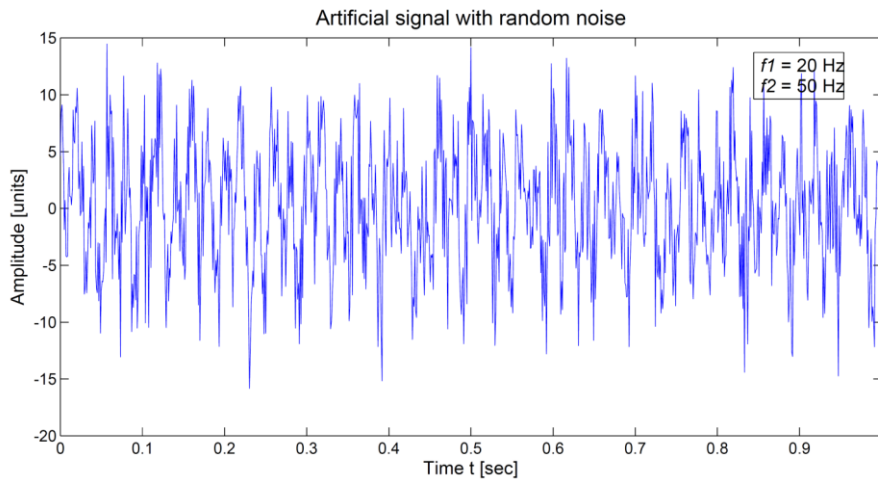
Figure 4.3: Noisy time signal generated by adding Gaussian white noise to $x(t) = 3 \sin 2\pi f_1 t + 5 \cos 2\pi f_2 t$.
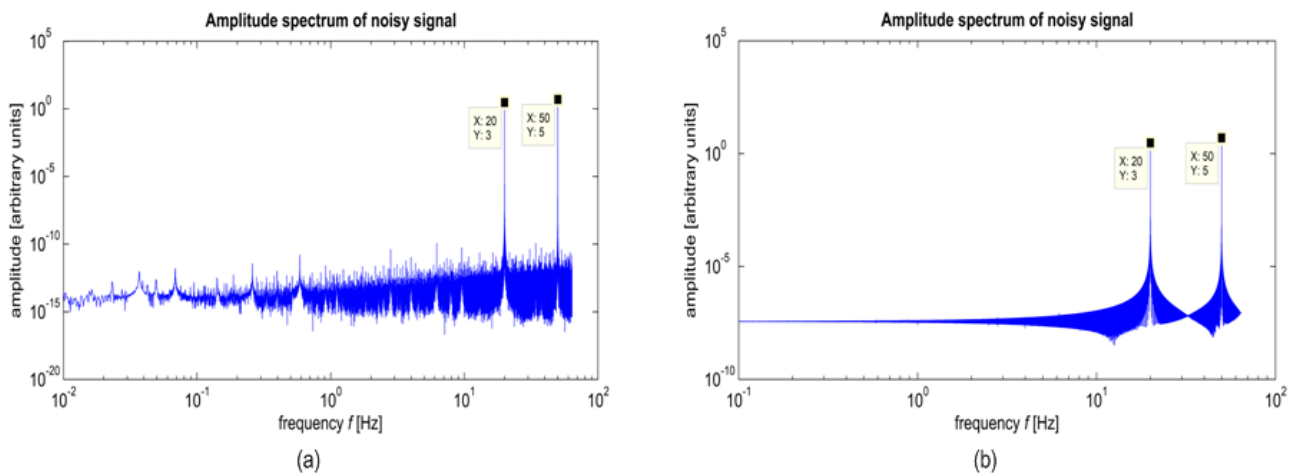
Figure 4.4: Amplitude spectrum of the signal $x(t)$ computed as the FFT of the arificial signal (a). Though the frequency components are clearly visible, some noisy peaks appear like periodicities. The amplitude spectrum computed as the FFT of the autocorrelation function of the signal (b) "cancel" out the noise and there are no spurious peaks.

54

4.5   Data Formats

LSSB data is binary encoded in SEGY and TITAN (NATIVE) formats, and is available at sampling frequencies of 125 Hz and 500 Hz for both magnetic and seismic recordings. Depending on the phenomena being investigated, magnetic data can be filtered as necessary. For correlations to seismic events, the data are typically band-pass filtered between 0.01 Hz and 10 Hz, while for magnetospheric and ionospheric phenomena frequencies below 1 Hz are very important.

SEGY is actually a file system created by the Society of Exploration Geophysicist (SEG) in order to standardize the archiving of seismic data. SEGY files are used in this research and Appendix A.2 gives a useful code for reading them into MATLAB.

5 Analysis of SQUID and Fluxgate Datasets

A Case Study on Geomagnetic Storms in 2011

Perturbations of the geomagnetic field are an indicator of activity in the ionosphere and magnetosphere. Hence geomagnetic field measurements form an important part of near-space monitoring. In this chapter, magnetic storms occurring during 2011 are studied in terms of their frequency components using both fluxgate and SQUID datasets. The fluxgate data were obtained from INTERMAGNET and the SQUID data were obtained from LSBB. The months studied were chosen based on the K_p index and the particular days in a month were selected based on the D_{st} index. That is, the K_p index is useful for identifying magnetically active days while the D_{st} index best describes the extent of magnetic variability (Section 2.1.5). A value of 5 for the K_p index signifies magnetic activity. Since INTERMAGNET data are averaged over 60 seconds, the Nyquist frequency of the fluxgate data is 8.3 mHz. Thus, the fluxgate and SQUID datasets were compared over a frequency range from 1 mHz to 8 mHz, with frequencies below 1 mHz excluded because of the high $1/f$ noise. The SQUID noise density spectra were also inspected for frequencies from 10 mHz up to 10 Hz. The results suggest that there could be some influences on the geomagnetic field with frequencies in the tens of millihertz (mHz) range, playing a role during disturbed conditions. This has been reported in [61] and [62] with regard to seismic influences on the ionosphere, and hence the magnetic field. The analysis reported here contains numerous graphs of frequency spectra and tables summarizing the information obtained from the graphs.

5.1   Quiet Day Variation and Noise Baselines

Based on K_p index data, December was the magnetically quietest month in 2011, but SQUID data for this month were not usable. Hence, instead, the quiet day noise baselines and frequency distributions were established using data recorded in January 2011. With the exception of a storm that occurred at 00:00 AM, coordinated universal time (UTC) on 6 January, the rest of the month was quiet with $K_p < 5$. Days 29 and 30 of the month had K_p values less than 0.5 (Figure 5.1) and were used to examine quiet day characteristics.
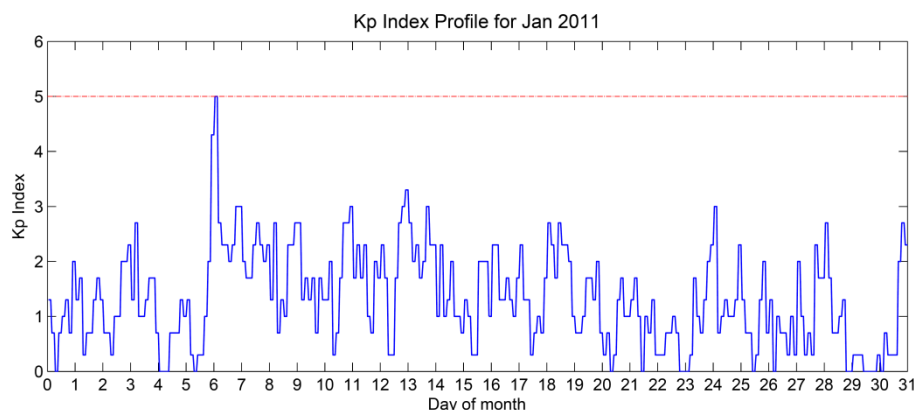
Figure 5.1: K_p index profile for January 2011. Days 6 and 7 were the most magnetically active days with a minor storm occurring in the early hours of day 6.

Figure 5.2 shows the time signals for Chambon la Forêt (CLF, 48.0°N, 2.3°E) in France and Furstenfeldbruck (FUR, 48.2°N, 11.3°E) in Germany with strong correlation as expected for sites with close latitudinal proximity. The variation at Hermanus (HER, 34.4°S, 19.2°E) and Hartebeesthoek (HBK, 25.9°S, 27.7°E), both in South Africa, is shown in Figure 5.3. It is clear from the two plots that a quiet day in the northern hemisphere is generally u-shaped, while the magnetic signals in the southern hemisphere are in general n-shaped. In both cases there an approximate symmetry around 10:00 – 12:00 UTC.
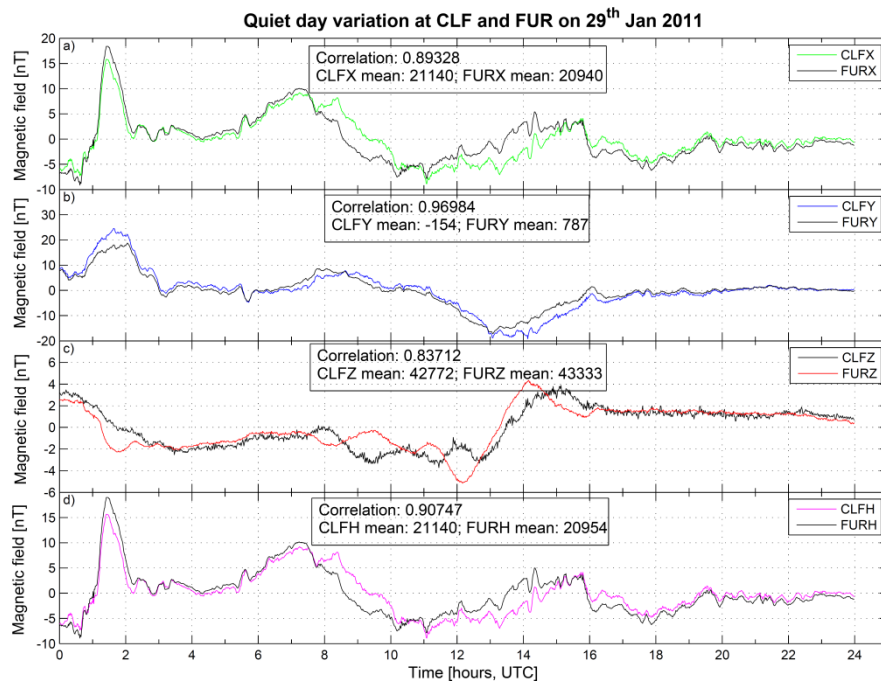
Figure 5.2: Quiet day variation in the northern hemisphere at Chambon la Forêt (CLF), France, and Furstenfeldbruck (FUR), Germany on 29 January 2011.
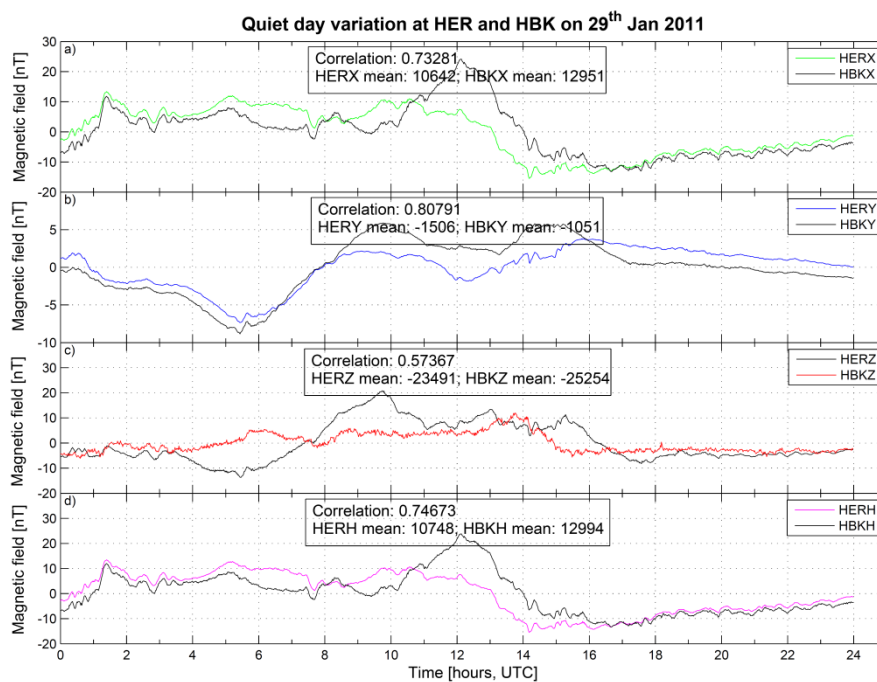
Figure 5.3: Quiet day variation in the southern hemisphere at Hermanus (HER) and Hartebeesthoek (HBK) stations in South Africa.

57

In Figure 5.4, the [SQUID][2] signals are plotted alongside observatory data from CLF and HER stations. LSBB is located at 43.92°N and 5.48°E, and shows good time and amplitude coincidence with CLF, which is typically the case for magnetometers within the same range of latitude. From the noise density plots (log-log plots of the amplitude spectral density) in Figure 5.5, the mean noise level in the SQUID signals for the two given days was calculated as 8.11 pT/√Hz.at 1 Hz, and increased to 8.00 nT/√Hz at 1 mHz. The average fluxgate noise level for both CLF and HER stations were 9.77 nT/√Hz and 10.00 nT/√Hz, respectively at 1 mHz.
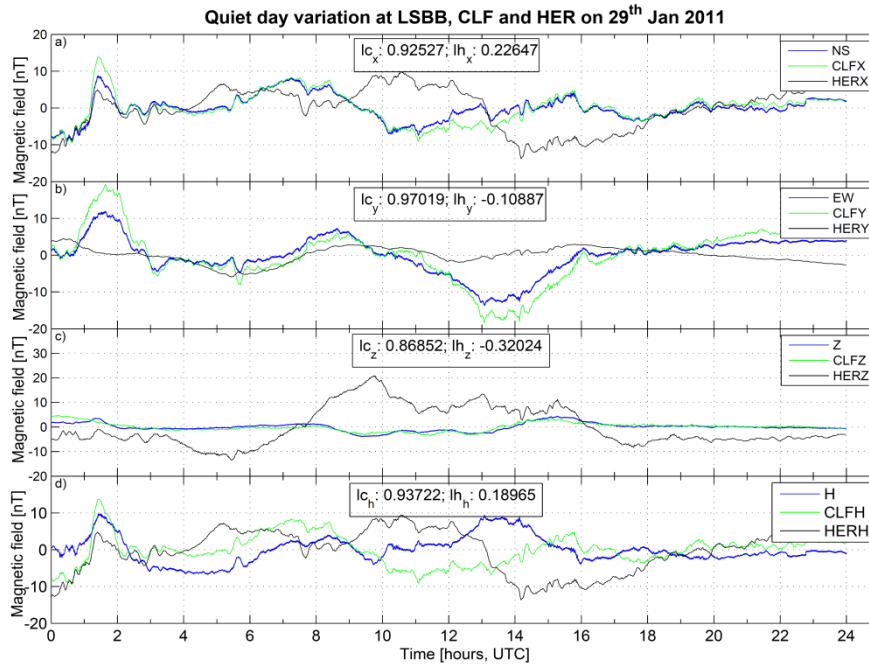
Figure 5.4: Magnetic signals at LSBB, CLF and HER on 29 January 2011. The SQUID signals are poorly correlated to the measurements at HER which shows localization of magnetic variation based on latitude.
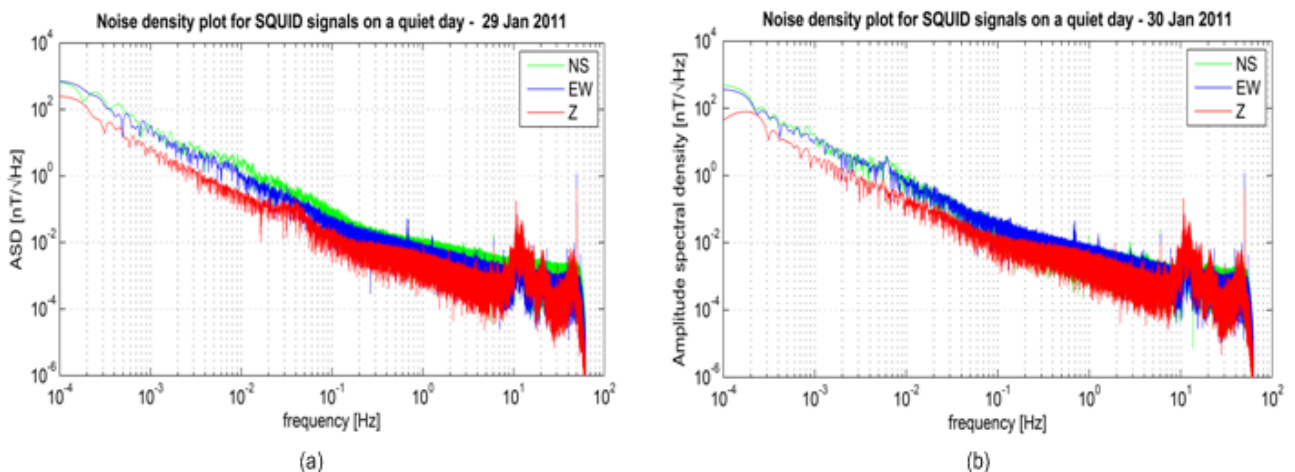
Figure 5.5: : Noise density plots for SQUID signals at LSBB on 29 and 30 January, 2011. The slopes indicate the presence of $1/f$ noise up to about 10 Hz.

The fact that the noise baselines are in the same range of magnitude both for different regions (using fluxgates) and for different sensors indicates that at low frequency $1/f$ noise is driven by environmental effects, rather than sensor performance.
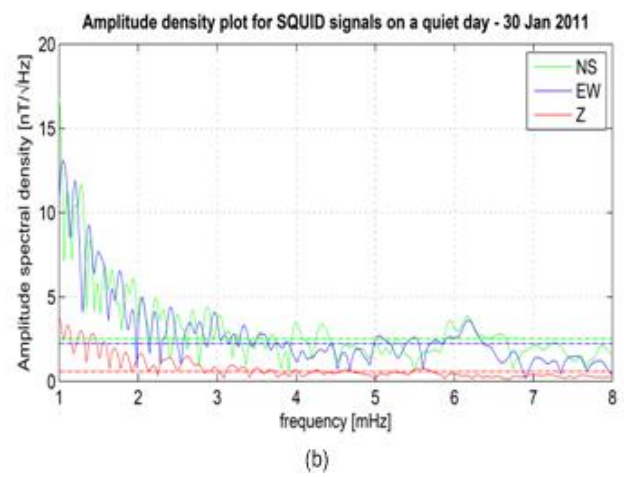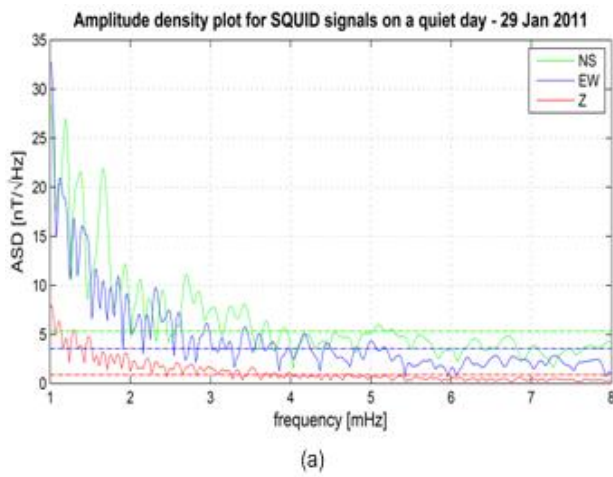
Figure 5.6: Amplitude density of SQUID signals in the 1 – 8 mHz range on 29 and 30 January 2011. Horizontal lines indicate thresholds for selecting or discarding frequency peaks.
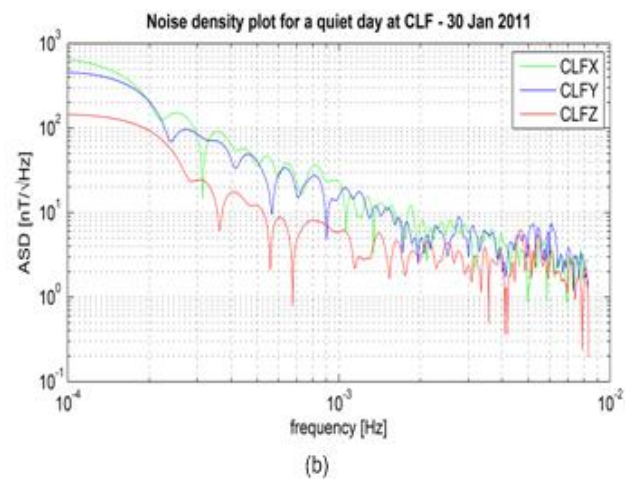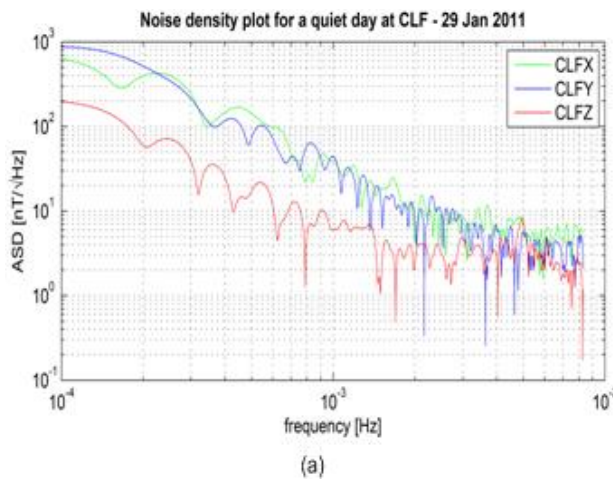
Figure 5.7: Noise density of fluxgate signals at Chambon la Forêt (CLF), France, on 29 and 30 January, 2011. The mean $1/f$ noise level was found to be 9.77 nT/$\sqrt{\text{Hz}}$ at 1 mHz. White noise dominates from around 3 mHz.
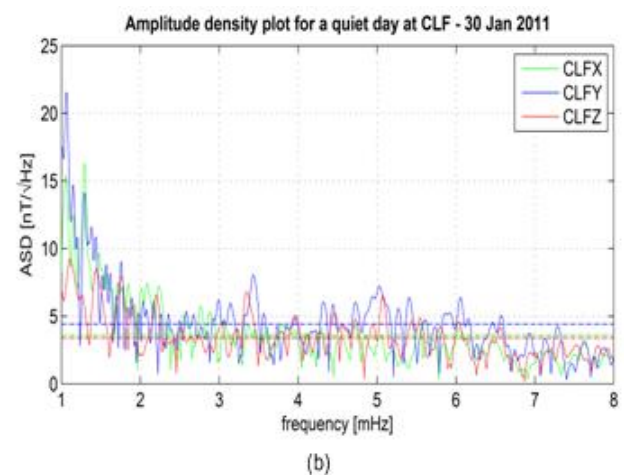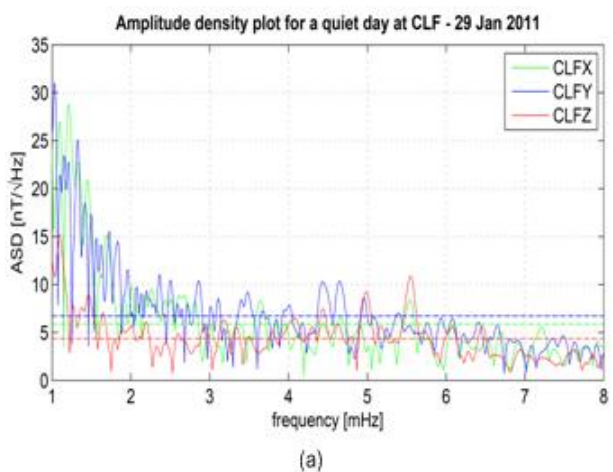
Figure 5.8: Amplitude density plots for signals at Chambon la Forêt (CLF) in the range 1 – 8 mHz on 29 and 30 January 2011. The horizontal lines indicate thresholds for selecting frequencies, with all peaks below the lines being discarded.
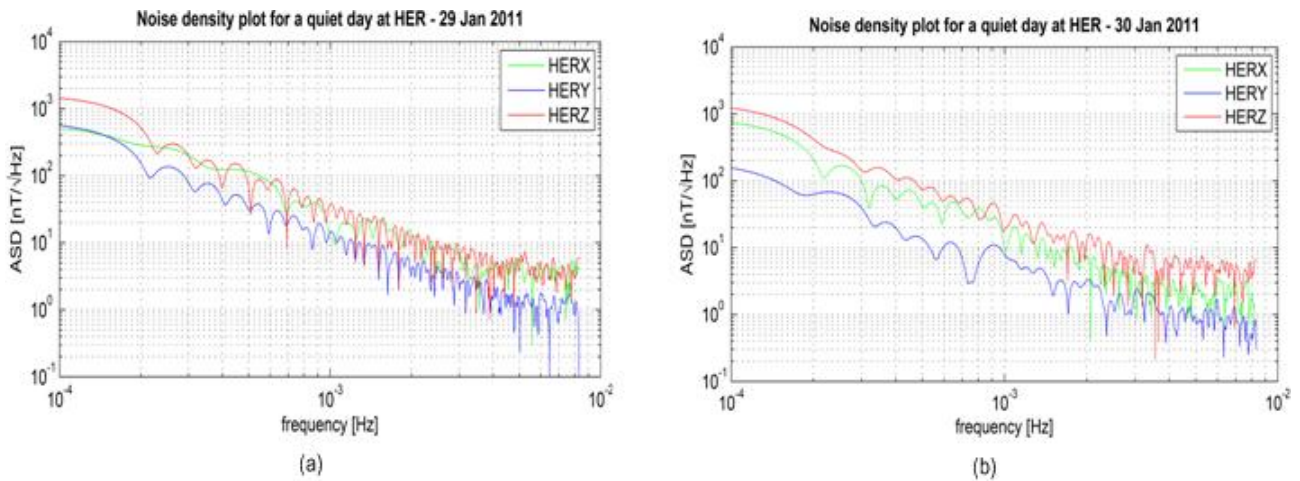
Figure 5.9: : Noise density of fluxgate signals at Hermanus (HER), South Africa, on 29 and 30 of January, 2011. At 1 mHz, the $1/f$ noise level was calculated to be 10.00 nT/$\sqrt{\text{Hz}}$. As for CLF, white noise appears to become important at around 3 mHz.
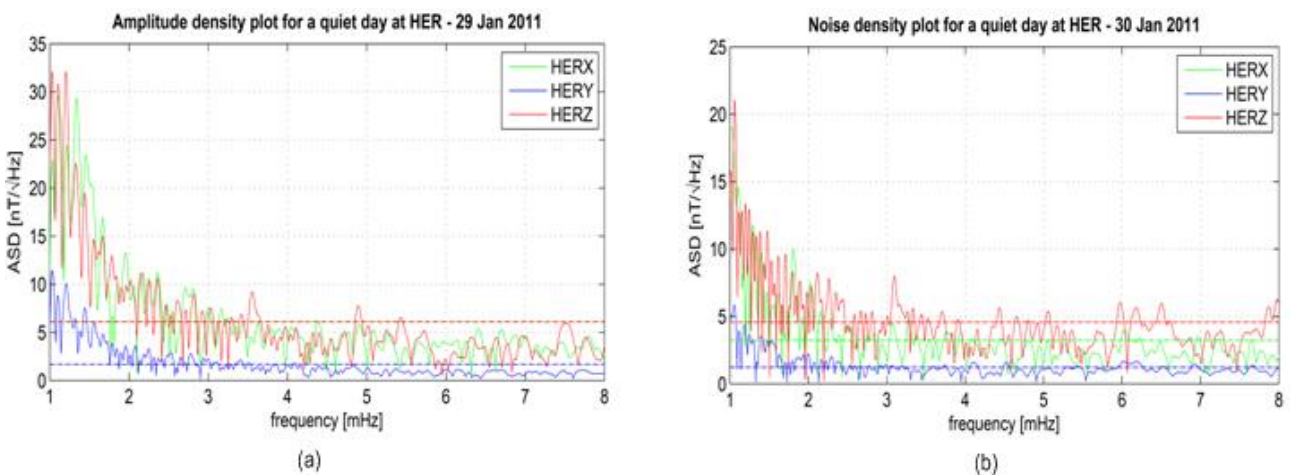
Figure 5.10: Amplitude density for signals at Hermanus (HER) on 29 and 30 January 2011.

Low frequencies rarely show as Dirac-delta peaks and hence it is more helpful to view the spectrum as an amplitude density rather than a noise density. The amplitude density plots are actually just the linear version of the noise density spectra but with a focus on the 1 – 8 mHz range, henceforth ultra-low frequency (ULF) range. The frequencies that showed Dirac-delta peaks on the noise density plots of the SQUID signals are listed in Table 5.1 while the ULF frequencies are shown in Table 5.2. The noise spectra of the fluxgate signals were not particularly helpful apart from providing a basis for estimating the fluxgate noise floor. The frequency peaks found in the ULF range from the amplitude density plots are listed in Table 5.3 and Table 5.5 for CLF, while Table 5.4 and Table 5.6 summarize the data from the HER station. It is clear from the data that a quiet day spectrum can exhibit the presence of many frequency peaks, which are probably due to the environmental, magnetic background noise.

60

Table 5.1: Quiet day frequencies as observed on 29 and 30 January 2011 from the Dirac-delta peaks on SQUID signal.

Station: LSBB – 29 and 30 Jan 2011					
NS		EW		Z	
Freq (Hz)	ASD (nT/√Hz)	Freq (Hz)	ASD (nT/√Hz)	Freq (Hz)	ASD (nT/√Hz)
-	-	0.60	0.028	-	-
-	-	0.70	0.049	-	-
1.00	0.020	1.26	0.017	1.00	0.011
1.28	0.012	1.91	0.012	1.91	0.007
1.91	0.012	-	-	-	-
2.81	0.011	-	-	2.00	0.022
-	-	3.00	0.007	3.00	0.005
-	-	3.95	0.006	3.98	0.004
-	-	-	-	4.81	0.004
6.06	0.021	6.06	0.016	6.06	0.007
-	-	7.81	0.006	-	-
-	-	10.80	0.265	10.78	0.182
11.06	0.060	11.05	0.069	-	-
15.63	0.007	15.63	0.009	15.63	0.007
		23.44	0.007		
-	-	39.06	0.007	30.30	0.002
		46.88	0.010	-	-
50.00	0.882	50.00	1.008	50.00	0.418

Table 5.2: ULF frequencies observed on SQUID channels on 29 and 30 January.

Station: LSBB (SQUID sensor)					
29 Jan 2011					
NS		EW		Z	
Freq (mHz)	ASD (nT/√Hz)	Freq (mHz)	ASD (nT/√Hz)	Freq (mHz)	ASD (nT/√Hz)
1.19	27.02	1.12	20.94	1.10	6.29
1.39	21.51	1.30	16.81	1.30	5.50
1.67	21.84	1.40	16.06	1.49	4.75
1.94	12.18	1.58	11.59	1.67	3.23
-	-	1.85	10.94	1.95	3.10
-	-	1.95	9.15	-	-
2.13	10.55	2.33	9.73	2.22	2.56
2.24	8.69	2.59	7.19	-	-
2.40	9.53	2.95	6.15	-	-
2.71	11.04	-	-	-	-
2.85	9.38	-	-	-	-
3.04	7.79	3.43	5.79	-	-
3.25	7.88	3.61	5.07	-	-
3.43	8.11	-	-	-	-
3.70	6.39	-	-	-	-
3.92	5.63	-	-	-	-
-	-	4.17	5.09	-	-
-	-	5.01	4.33	-	-
30 Jan 2011					
1.10	11.21	1.04	13.08	1.12	3.28
1.28	11.72	1.21	11.87	1.28	2.99
1.40	8.63	1.37	9.26	1.42	2.81
1.57	6.92	1.49	7.70	1.57	2.35
1.92	6.10	1.76	6.51	1.85	1.69
2.21	4.83	2.06	4.94	2.04	1.62
2.70	4.17	2.21	4.11	2.40	1.41
2.88	4.43	2.40	4.34	2.62	1.48
-	-	2.95	4.03	-	-
3.03	3.92	3.34	3.33	-	-
3.99	3.49	3.58	2.82	-	-
4.32	3.39	-	-	-	-
5.93	3.58	5.04	2.70	-	-
-	-	5.48	2.60	-	-
6.17	3.86	6.17	3.62	-	-

Table 5.3: ULF frequencies observed from the amplitude density plot of fluxgate signals at Chambon la Foret on 29 Jan 2011.

Station: Chambon la Forêt (CLF)					
CLFX		CLFY		CLFZ	
Freq (mHz)	ASD (nT/√Hz)	Freq (mHz)	ASD (nT/√Hz)	Freq (mHz)	ASD (nT/√Hz)
1.10	26.90	1.03	30.93	1.09	15.08
1.23	28.68	1.10	21.36	1.27	7.74
1.34	22.67	1.15	23.35	1.46	9.00
1.46	20.82	1.21	22.60	1.65	7.06
1.70	15.10	1.32	25.09	-	-
1.91	8.53	1.41	18.43	-	-
-	-	1.50	17.12	-	-
-	-	1.73	15.53	-	-
-	-	1.83	14.48	-	-
-	-	1.96	11.52	-	-
2.01	9.71	2.07	9.61	2.00	5.89
2.10	7.90	2.13	9.07	2.19	6.09
2.26	9.54	2.37	10.78	2.60	4.84
2.50	8.42	2.51	10.34	2.93	5.89
2.67	8.86	2.86	10.37	-	-
2.82	8.16	-	-	-	-
3.64	8.34	3.02	7.64	3.19	6.28
-	-	3.11	8.52	3.34	5.52
-	-	3.48	9.20	3.79	5.05
-	-	3.67	7.22	-	-
4.68	6.40	4.01	7.84	4.07	6.42
-	-	4.44	10.25	4.32	5.48
-	-	4.65	10.35	4.44	7.48
-	-	4.95	8.51	4.63	5.89
-	-	-	-	4.99	9.23
5.53	8.33	5.40	7.03	5.17	5.59
-	-	-	-	5.55	10.86
-	-	-	-	6.08	5.54
-	-	-	-	6.46	5.62

Table 5.4: ULF frequencies observed from the amplitude density plot fluxgate signals at Hermanus on 29 Jan 2011.

Station: Hermanus (HER)					
HERX		HERY		HERZ	
Freq (mHz)	ASD (nT/√Hz)	Freq (mHz)	ASD (nT/√Hz)	Freq (mHz)	ASD (nT/√Hz)
1.03	22.90	1.03	11.44	1.03	31.99
1.09	29.50	1.10	8.83	1.11	30.77
1.24	24.25	1.20	10.04	1.20	32.12
1.33	29.29	1.44	7.54	1.33	22.59
1.45	23.33	1.47	0.13	1.45	19.41
1.66	16.87	1.55	6.10	1.56	14.52
1.96	13.30	1.67	4.75	1.67	15.00
-	-	1.80	3.68	1.79	12.96
-	-	1.96	3.58	-	-
2.16	11.01	2.08	3.59	2.02	10.40
2.25	10.60	2.25	3.30	2.17	11.12
2.36	11.23	2.53	2.88	2.26	10.27
2.46	7.78	2.65	2.42	2.34	10.62
2.61	8.30	2.78	2.78	2.46	7.73
2.71	9.58	-	-	2.61	8.31
2.82	9.47	-	-	2.72	7.29
-	-	-	-	2.82	8.93
-	-	-	-	2.92	7.20
3.03	7.45	-	-	3.03	7.50
3.17	7.46	-	-	3.55	9.20
-	-	-	-	4.90	7.74
-	-	-	-	5.43	6.53

Table 5.5: ULF frequencies observed from the amplitude density plot of fluxgate signals at Chambon la Foret on 30 Jan 2011.

Station: Chambon la Forêt (CLF)					
CLFX		CLFY		CLFZ	
Freq (mHz)	ASD (nT/√Hz)	Freq (mHz)	ASD (nT/√Hz)	Freq (mHz)	ASD (nT/√Hz)
1.17	12.46	1.15	14.70	1.44	8.47
1.29	16.22	1.29	14.10	1.76	7.87
1.48	9.58	1.57	8.80	1.90	5.73
1.73	7.35	1.75	9.01	2.20	6.58
1.84	7.32	1.89	6.24	2.51	4.15
2.02	7.03	2.04	6.01	2.22	0.12
2.08	7.42	2.18	6.04	2.50	0.09
2.22	7.11	2.24	5.10	-	-
2.57	5.09	2.36	5.15	-	-
2.77	5.71	2.58	5.33	-	-
2.87	5.27	2.68	5.11	-	-
-	-	2.99	6.15	-	-
3.06	4.67	3.14	3.95	3.03	4.52
3.38	4.42	3.43	8.05	3.32	4.06
3.60	4.16	3.56	5.17	3.36	6.82
3.80	4.42	3.95	4.93	3.97	5.06
4.28	4.12	4.32	6.02	4.46	5.25
4.68	4.41	4.44	5.86	4.72	4.74
-	-	4.73	6.02	-	-
5.54	4.42	5.03	7.21	5.08	6.48
-	-	5.27	5.56	5.44	4.71
-	-	5.41	6.36	5.56	4.79
-	-	-	-	5.80	4.21
6.06	4.15	6.06	6.38	6.04	4.58
-	-	6.57	5.02	6.56	4.17

Table 5.6: ULF frequencies observed from the amplitude density plot fluxgate signals at Hermanus on 30 Jan 2011.

Station: Hermanus (HER)					
HERX		HERY		HERZ	
Freq (mHz)	ASD (nT/√Hz)	Freq (mHz)	ASD (nT/√Hz)	Freq (mHz)	ASD (nT/√Hz)
1.08	14.58	1.06	5.79	1.06	21.05
1.29	11.78	1.19	4.37	1.20	13.26
1.40	9.79	1.41	3.54	1.48	11.21
1.80	9.94	-	-	1.62	9.48
-	-	-	-	1.71	9.59
-	-	-	-	1.78	8.28
-	-	-	-	1.89	7.63
2.03	7.46	2.00	2.23	2.12	8.14
2.16	5.31	2.30	2.01	2.26	7.79
2.29	4.92	-	-	2.36	6.72
2.50	4.31	-	-	-	-
2.84	3.74	-	-	-	-
3.06	4.58	-	-	3.09	7.94
3.28	4.81	-	-	3.34	5.49
3.95	3.80	-	-	3.71	5.35
-	-	4.11	1.58	4.44	5.56
-	-	4.52	1.57	4.65	4.93
-	-	-	-	5.06	5.37
-	-	-	-	5.98	6.00
6.04	4.04	-	-	6.19	5.66
6.97	3.50	-	-	6.51	5.95
-	-	-	-	7.87	5.70
-	-	-	-	7.97	6.25

5.2   Storm-time Frequency Analysis[***]

For the subsequent magnetic storm analysis, fluxgate data from three INTERMAGNET stations – namely, Chambon la Forêt (CLF) in France, Ebro (EBR, 47.1°N, 0.5°E) in Spain and Furstenfeldenbruck (FUR) in Germany – were compared against the SQUID data from the Laboratoire Souterrain à Bas Bruit (LSBB). The frequency spectra were obtained using the Wiener-Khintchine theorem (FFT of autocorrelation, Appendix A.3) and peaks were manually selected. A normal distribution was used to aid the selection but there is still a measure of intuition required to determine which peaks are due to periodicity and which ones must be discarded as noise.

5.2.1   Case 1 – Moderate Storm on March 1

The K_p index profile for March 2011 is shown in Figure 5.11(a). It can be seen that there was significant magnetic activity on days 1, 11 and 12 of the month. D_{st} index plots (shown only for day 1) for these days reveal that the most active day was in fact day 1 and not day 11 as suggested by the K_p index profile. A moderate storm commenced around 13:00 UTC as can be seen in Figure 5.11(b). The time signals of the magnetic variation are plotted in Figure 5.12 with sudden storm commencement (SSC) occurring just before 12:00 UTC. All the field components show deviation from the quiet day variation. The noise density plot (Figure 5.13(a)) of the SQUID signals shows the appearance of Dirac-delta

---

*** NOTE: The storm-time analysis amplitudes are offset due to a programming error. For both SQUID and fluxgate data, the amplitudes ought to lie in a similar range of magnitude as the quiet day spectra, except of course for an increase in the amplitudes. Emphasis is hereby placed on the frequencies present as opposed to their amplitudes.

peaks between 0.1 Hz and 1 Hz not observed during a quiet day. These are listed in Table 5.7. The ULF frequencies from the SQUID data (Figure 5.13(b)) are shown in Table 5.8.

(a)

(b)
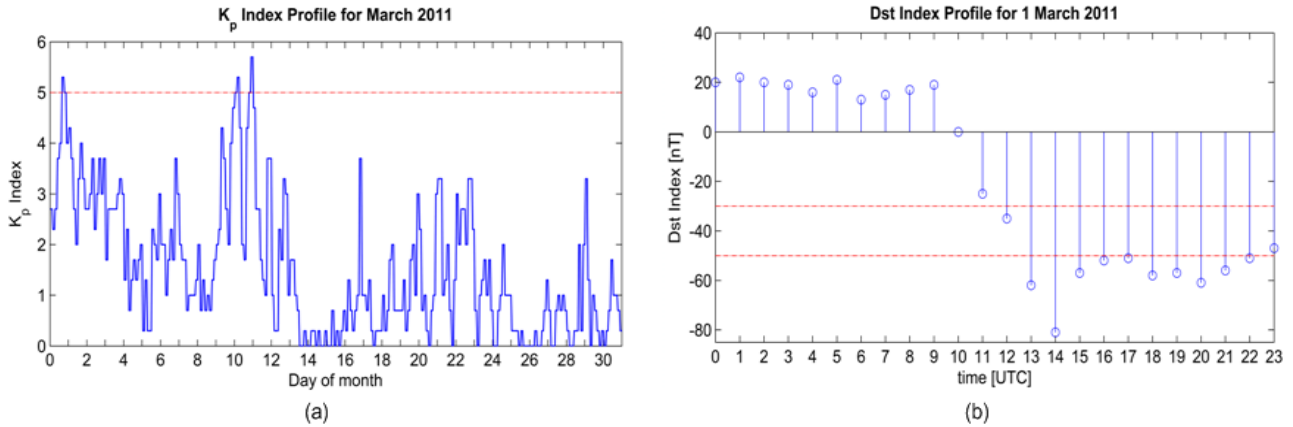
Figure 5.11: K_p **index profile for March 2011 (a), showing magnetic disturbances on days 1, 11 and 12 of the month. The** D_{st} **index variation on 1 March 2011 (b) shows that there was a moderate storm that commenced around 10:00 UTC.**
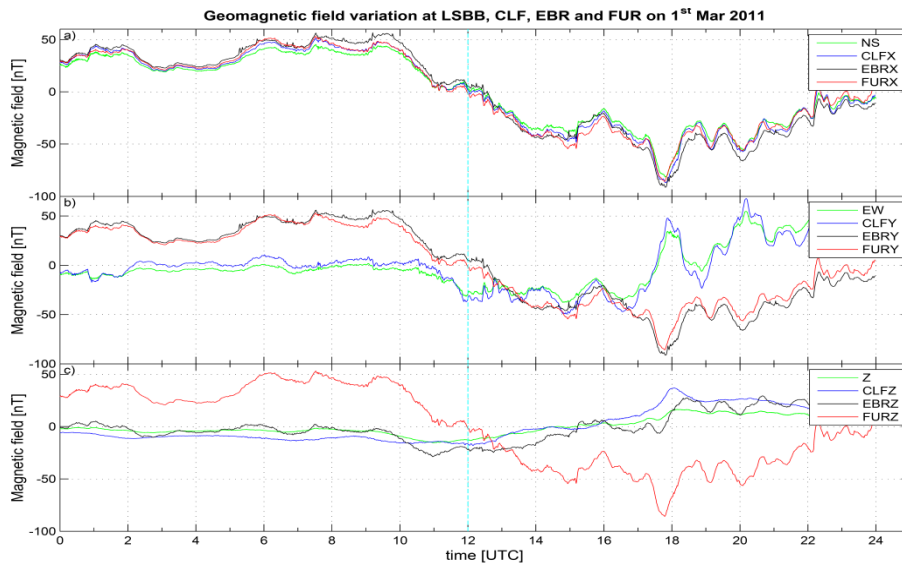
Figure 5.12: Time signals for the moderate storm on 1 March 2011. The vertical cyan line indicates the time of occurrence of intense magnetic activity based on D_{st} **index data.**

(a)

(b)
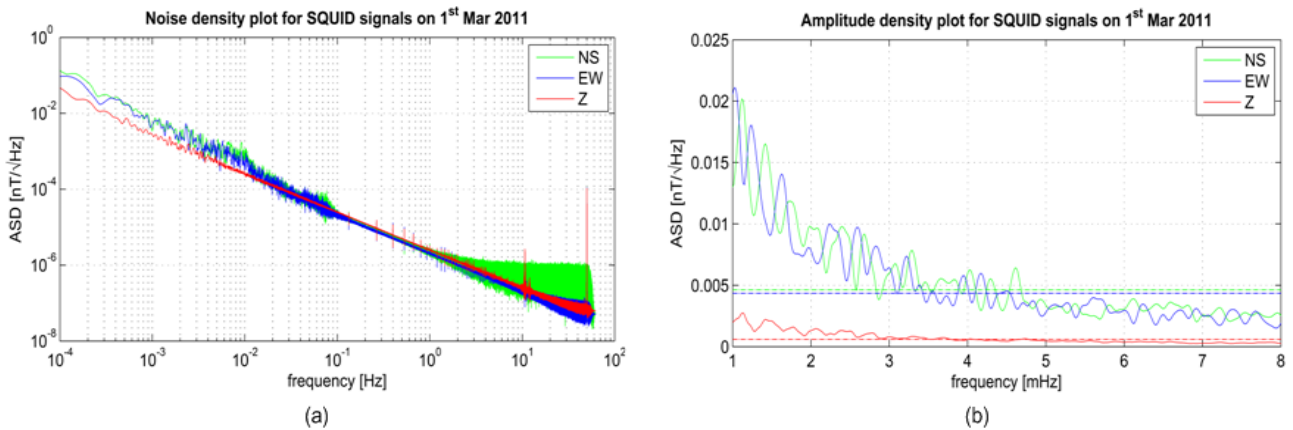
Figure 5.13: Noise density and amplitude density plots for SQUID signals on 1 March 2011.

Tables 5.7 to 5.9 shows the ULF frequencies obtained from the spectra in Figure 5.14. Taking values within 5% of each other, the recurring frequencies from the fluxgate data were 1.18 mHz, 1.46 mHz, 1.78 mHz and **2.51 mHz** on the x-components and 1.18 mHz, 1.46 mHz, 1.75 mHz, **1.93 mHz**, 2.22 mHz, **2.56 mHz** and 2.72 mHz on the y-component. The frequencies in bold text lie within 5% of the so-called "magic" frequencies which normally recur in studies of Pc5 pulsations.

Table 5.7: Frequencies observed between 0.1 and 1 Hz from the Dirac-delta peaks of the SQUID noise density plot

Freq (Hz)	Mean ASD (fT/√Hz)	Axis		
		NS	EW	Z
0.13	23.7	-	✓	✓
0.27	15.3	-	✓	✓
0.40	11.6	-	✓	✓
0.53	9.71	-	✓	✓
0.66	0.86	-	✓	✓
0.80	4.58	-	✓	✓

Table 5.9: ULF frequencies observed on the amplitude density plot of signals at CLF on 1 March 2011.

Sensor: Fluxgate (CLF)					
CLFX		CLFY		CLFZ	
Freq (mHz)	ASD (nT/√Hz)	Freq (mHz)	ASD (nT/√Hz)	Freq (mHz)	ASD (nT/√Hz)
1.22	1.79	1.18	2.43	-	-
1.46	1.49	1.45	1.88	-	-
1.78	1.27	1.77	1.31	-	-
-	-	1.93	1.25	-	-
2.03	1.06	2.55	0.10	-	-
2.39	0.95	2.72	0.95	-	-
2.53	0.86	-	-	-	-

Table 5.11: ULF frequencies observed on the amplitude density plot of signals at FUR on 1 March 2011.

Sensor: Fluxgate (FUR)					
FURX		FURY		FURZ	
Freq (mHz)	ASD (nT/√Hz)	Freq (mHz)	ASD (nT/√Hz)	Freq (mHz)	ASD (nT/√Hz)
1.18	2.05	1.46	1.49	-	-
1.47	1.70	1.75	0.97	-	-
1.77	1.39	1.93	0.86	-	-
2.05	1.18	2.22	0.80	-	-
2.38	1.08	2.56	0.68	-	-
-	-	2.72	0.72	-	-
3.17	0.84	3.22	0.54	-	-

Table 5.8: ULF frequencies observed on the amplitude density plot of SQUID signals on 1 March 2011.

Sensor: SQUID					
NS		EW		Z	
Freq (mHz)	ASD (pT/√Hz)	Freq (mHz)	ASD (pT/√Hz)	Freq (mHz)	ASD (pT/√Hz)
1.12	20.19	1.24	18.07	-	-
1.42	16.53	1.64	14.07	-	-
1.74	11.83	-	-	-	-
2.38	9.79	2.24	9.99	-	-
2.68	9.17	2.59	9.74	-	-
-	-	2.83	8.19	-	-
3.29	7.82	3.23	7.38	-	-
-	-	3.95	5.80	-	-
4.02	6.27	4.17	5.98	-	-
4.31	5.53	-	-	-	-
4.62	6.39	-	-	-	-

Table 5.10: ULF frequencies observed on the amplitude density plot of signals at EBR on 1 March 2011.

Sensor: Fluxgate (EBR)					
EBRX		EBRY		EBRZ	
Freq (mHz)	ASD (nT/√Hz)	Freq (mHz)	ASD (nT/√Hz)	Freq (mHz)	ASD (nT/√Hz)
1.18	1.63	1.18	1.54	-	-
1.46	1.44	1.46	1.34	-	-
1.78	1.25	-	-	-	-
2.09	1.06	2.22	0.75	-	-
2.38	0.88	2.56	0.69	-	-
2.51	0.84	-	-	-	-
3.17	0.86	3.02	0.52	-	-
4.63	0.65	-	-	-	-

The curves of the z-components were relatively flat, with no convincing peaks. As can be seen in Figure 5.14, the amplitudes on the z-components were also smaller than the amplitudes observed on the x- and y-components. This is indicative of the fact that electromagnetic excitation is predominantly in the vertical direction as the result of a perturbed ionosphere. That is, the electric field between the ionosphere and the ground excites magnetic fluctuations in the horizontal components. The lower amplitudes in the vertical components also indicate that the major contributor to $1/f$ noise is environmental effects, as opposed to sensor characteristics.

Comparing the SQUID data to the fluxgate x- and y-components, there is coincidence at 1.12 mHz (5.1% of 1.18 mHz), 1.42 mHz (2.74% of 1.46 mHz), 1.74 mHz, (2.3% of 1.78 mHz), in the north-south (NS) direction. In the east-west (EW) direction, coincidence occurs for 2.24 mHz (0.9% of 2.22 mHz), 2.59 mHz (1.17% of 2.56 mHz), and 2.83 mHz (4.04% of

2.72 mHz). There was also correspondence (99.69%) of 3.23 mHz on the EW component to 3.22 mHz on the FURY component.
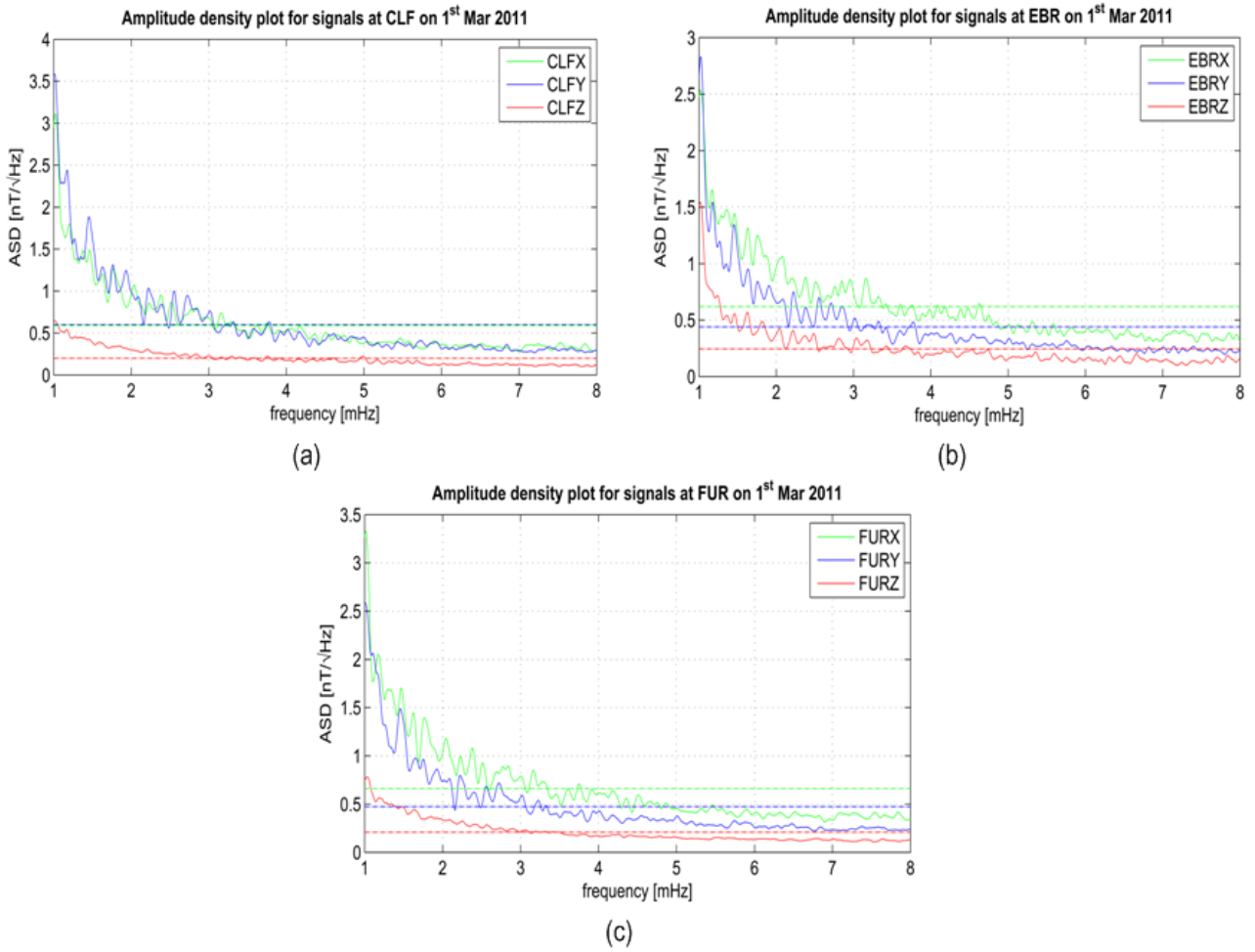
Figure 5.14: Amplitude density of signals at Chambon la Forêt (CLF) (a), Ebro (EBR) (b) and Furstenfeldenbruck (FUR) (c) during the moderate storm on 1 March 2011.

5.2.2   Case 2 – Moderate Storm on April 6

The K_p index profile for April 2011 is shown in Figure 5.15(a). Day 6 was magnetically the most active with a moderate storm peaking around 18:00 UTC as shown by the plot of hourly D_{st} index values in Figure 5.15(b). The variation of the magnetic field is plotted in Figure 5.16, with SSC (sudden storm commencement) occurring around 12:30 UTC.

(a)   (b)
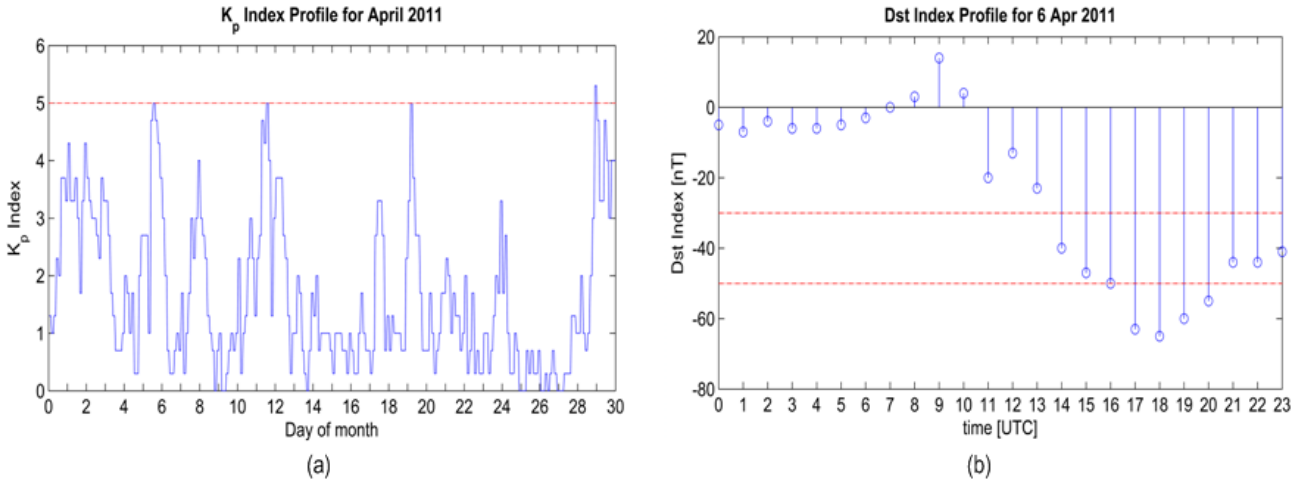
Figure 5.15: Variation of K_p index during April 2011 (a). Notable magnetic activity occurred on days 6, 12, 20, and 29. The most active was day 6 with a moderate storm commencing around 12:00 UTC based on D_{st} index (b).
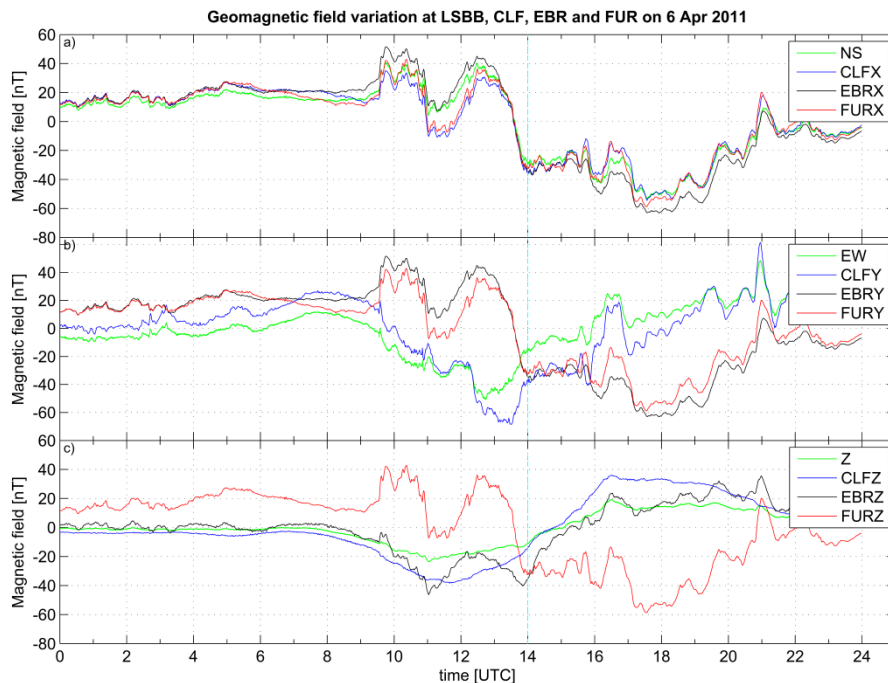
Figure 5.16: Time signals for the moderate storm on 6 April 2011. The commencement of the hour with the most intense activity is shown by the vertical cyan line. Sudden storm commencement occurred at around 12:30 UTC.

Tables 5.10 to 5.13 list the frequencies and amplitudes identified on the spectra in Figure 5.17 and Figure 5.18. The recurring frequencies from the fluxgate data are **1.30 mHz**, 1.74 mHz, **1.91 mHz**, 2.05 mHz and **2.60 mHz** x-components, and **1.31 mHz**, 1.39 mHz, 1.53 mHz, 2.21 mHz, 2.46 mHz, **2.70 mHz** and **3.34 mHz** on the y-components.

66
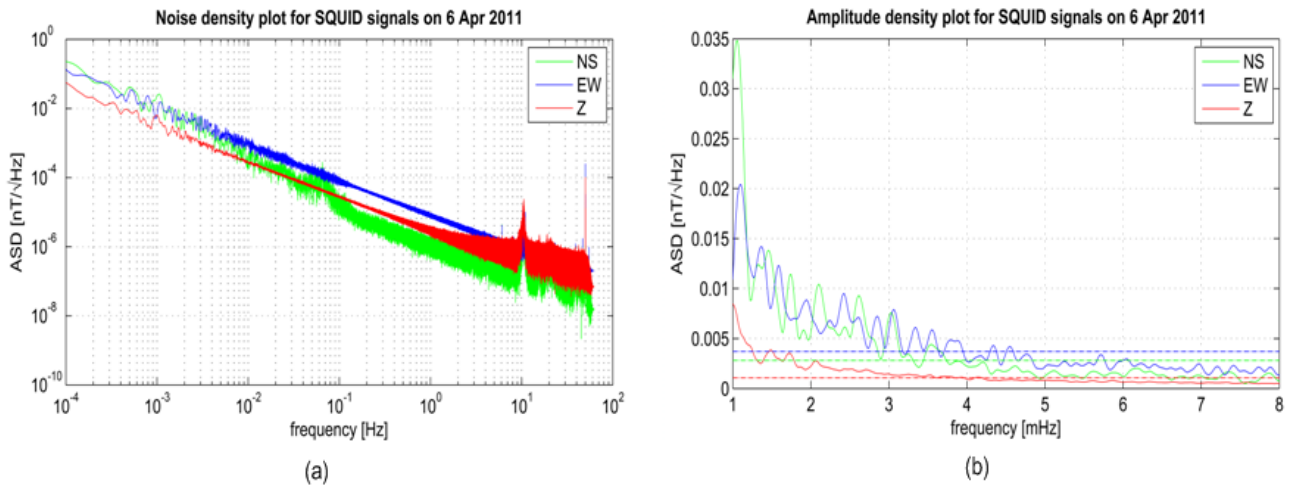
Figure 5.17: Noise density and amplitude density plots for SQUID signals on 6 April 2011.

Table 5.12: Frequencies observed in the ULF range on the amplitude density plot of SQUID signals on 6 April 2011.

Sensor: SQUID (LSBB)					
X (NS)		Y (EW)		Z	
Freq (mHz)	ASD (pT/√Hz)	Freq (mHz)	ASD (pT/√Hz)	Freq (mHz)	ASD (pT/√Hz)
1.06	34.81	1.10	20.41	1.48	3.83
1.46	13.82	1.37	14.18	1.73	3.53
1.74	11.43	1.58	12.31	-	-
-	-	1.94	8.85	-	-
2.10	10.44	2.43	9.46	-	-
2.61	9.29	2.85	7.22	-	-
3.04	7.64	3.07	7.86	-	-
-	-	3.34	6.11	-	-
-	-	3.55	5.87	-	-
-	-	4.34	4.31	-	-

Table 5.13: Frequencies observed in the ULF range on the amplitude density plot of signals at CLF on 6 April 2011.

Sensor: Fluxgate (CLF)					
X		Y		Z	
Freq (mHz)	ASD (nT/√Hz)	Freq (mHz)	ASD (nT/√Hz)	Freq (mHz)	ASD (nT/√Hz)
1.09	2.32	1.32	1.34	-	-
1.30	1.24	1.39	1.33	-	-
1.73	0.95	1.54	0.85	-	-
1.91	0.64	1.70	0.68	-	-
2.05	0.86	2.02	0.76	-	-
2.31	0.72	2.21	0.69	-	-
2.56	0.58	2.46	0.75	-	-
2.61	0.57	2.70	0.55	-	-
3.87	0.39	3.11	0.42	-	-
-	-	3.34	0.50	-	-
-	-	3.56	0.40	-	-

Table 5.14: Frequencies observed in the ULF range on the amplitude density plot of signals at EBR on 6 April 2011.

Sensor: Fluxgate (EBR)					
X		Y		Z	
Freq (mHz)	ASD (nT/√Hz)	Freq (mHz)	ASD (nT/√Hz)	Freq (mHz)	ASD (nT/√Hz)
1.79	2.08	1.12	0.95	1.08	1.36
1.31	1.28	1.31	0.88	1.30	0.70
1.75	0.93	1.40	0.78	1.43	0.60
1.91	0.69	1.53	0.57	1.73	0.65
-	-	-	-	1.92	0.42
2.06	0.79	2.09	0.38	2.05	0.48
2.29	0.68	2.46	0.38	-	-
2.60	0.58	-	-	-	-
-	-	3.12	0.26	-	-
-	-	3.35	0.26	-	-
-	-	3.89	0.23	-	-

Table 5.15: Frequencies observed in the ULF range on the amplitude density plot of signals at FUR on 6 April 2011.

Sensor: Fluxgate (FUR)					
X		Y		Z	
Freq (mHz)	ASD (nT/√Hz)	Freq (mHz)	ASD (nT/√Hz)	Freq (mHz)	ASD (nT/√Hz)
1.04	2.75	1.07	1.57	-	-
1.30	1.30	1.31	1.05	-	-
1.74	1.67	-	-	-	-
2.05	0.94	2.22	0.47	-	-
2.13	0.87	2.46	0.52	-	-
2.30	0.75	2.70	0.39	-	-
2.61	0.67	-	-	-	-
2.99	0.58	-	-	-	-
-	-	3.35	0.34	-	-

Comparing the SQUID spectrum against this, coincidence was noted at 1.74 mHz, 2.10 mHz (2.43% of 2.05 mHz) and 2.61 mHz (0.38% of 2.60 mHz) in the NS direction, and 1.37 mHz (1.44% of 1.39 mHz), 1.58 mHz (3.27% of 1.53 mHz), 1.94 mHz (1.57% of 1.91 mHz), 2.43 mHz (1.22% of 2.46 mHz) and 3.34 mHz in the EW direction. Several frequencies were identified on the EBRZ channel with good correlation to the frequencies identified on the EBRX and EBRY

channels. The two peaks identified on the Z channel of the SQUID data coincided well (within 5%) with the observations at EBR.

(a)

(b)

(c)
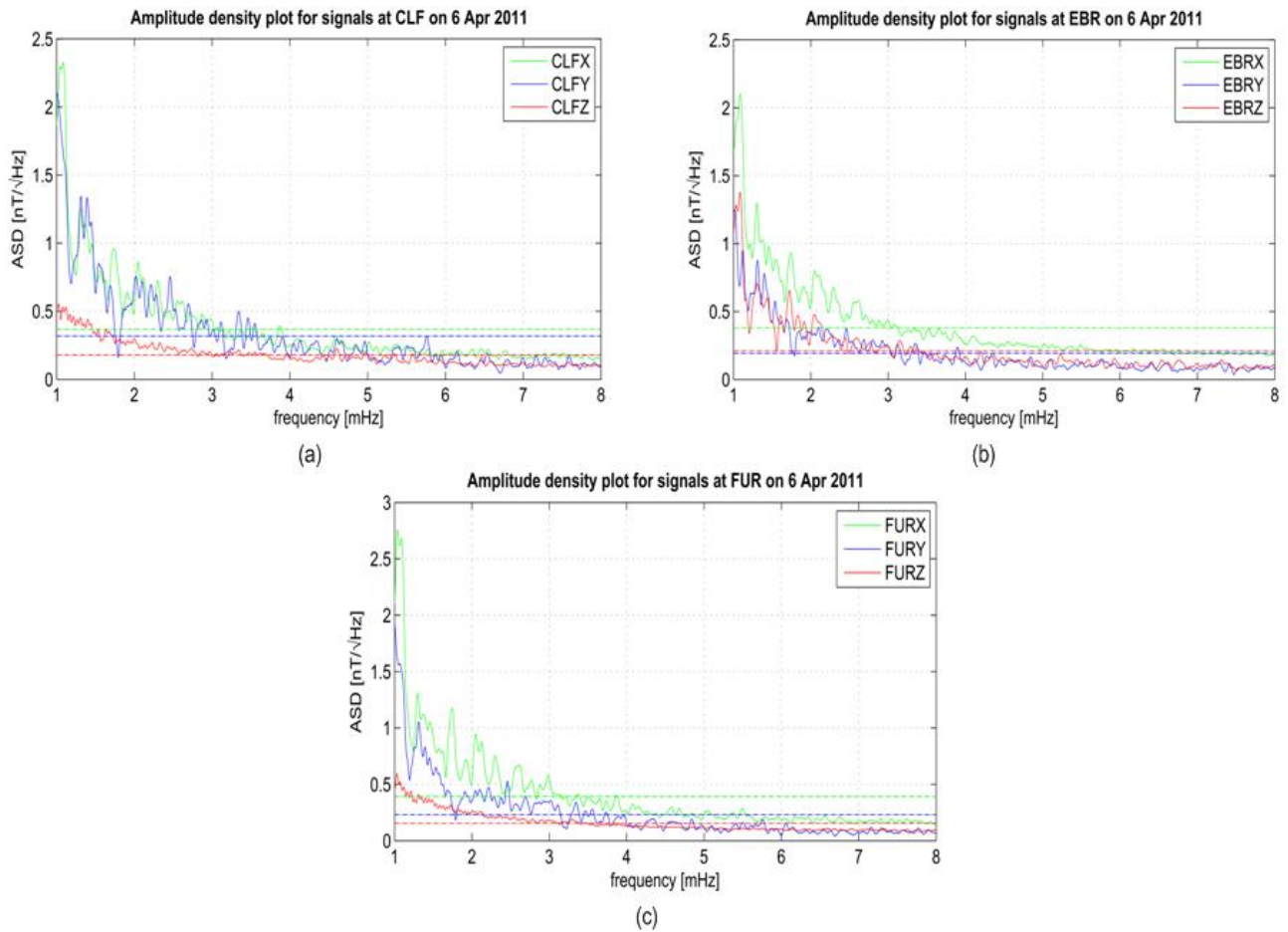
Figure 5.18: Amplitude density plots for signals at CLF, EBR and FUR for the moderate storm on 6 April 2011.

5.2.3   Case 3 – Moderate Storm on May 28 (with substorm on May 29)

Magnetic activity in the month of May 2011 was most intense on days 28 and 29, with disturbed conditions lasting over 36 hours as can be seen from the time signals in Figure 5.20. The K_p index values for the month are plotted in Figure 5.19(a) alongside the hourly D_{st} index over the two days.

(a)

(b)
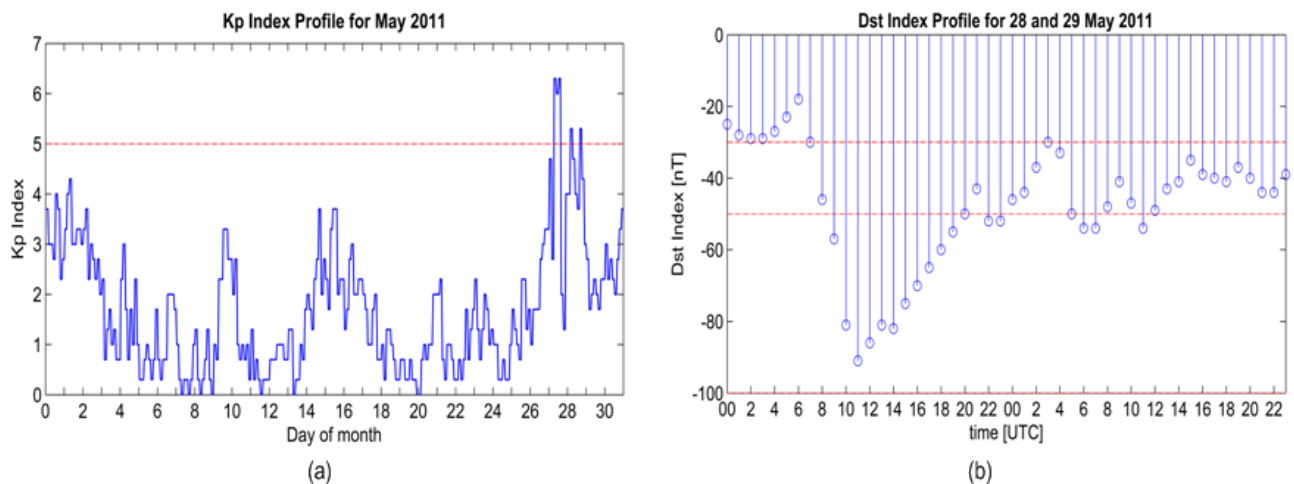
Figure 5.19: Variation of K_p index over May 2011 (a) and the hourly D_{st} index values for days 28 and 29 of the month (b).
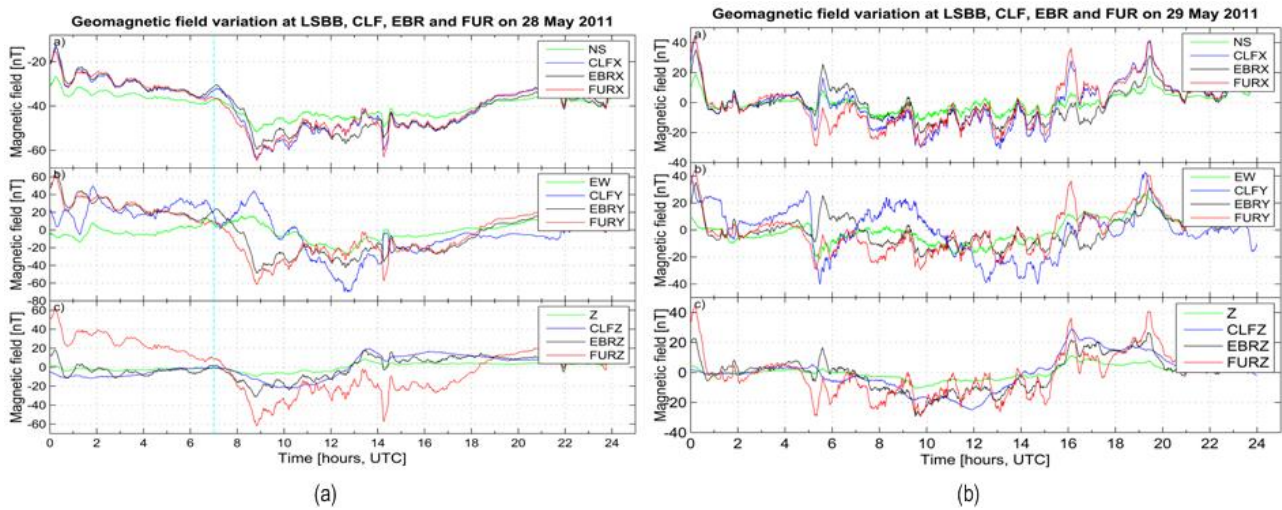
Figure 5.20: Time recordings of magnetic activity on 28 and 29 April 2011 at LSBB, CLF, EBR and FUR stations. A moderate storm occurred around 05:00 UTC on 28 May (a) with substorm effects evident on 29 May (b).
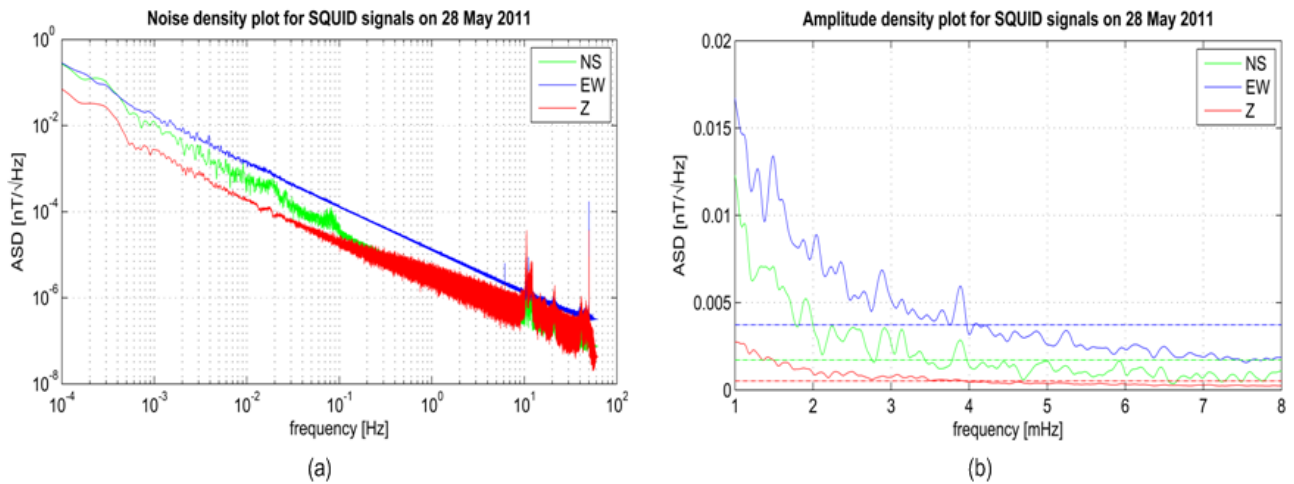
Figure 5.21: Noise density and amplitude density plots for SQUID signals on 28 may 2011.

The observations from the amplitude spectra on 28 May 2011, as shown in Figures 5.21 and 5.22, are summarized in Tables 5.14 to 5.17. The x- and y-components of the fluxgate data had very good agreement for several of the frequencies identified at the three observatories. Recurring on the x-components were 1.03 mHz, 1.28 mHz, 1.70 mHz, **1.91 mHz**, 2.31 mHz, and 3.06 mHz, while the y-components had recurrent values at 1.03 mHz, **1.33 mHz**, 1.71 mHz, 1.86 mHz, **2.63 mHz** and 3.25 mHz. Apart from a 98.08% agreement at 1.04 mHz between EBRZ and FURZ channels, there was no coincidence in the vertical direction. Comparing the SQUID data to these fluxgate observations, SQUID-to-fluxgate frequency correspondence was noted for 1.27 mHz (0.78% of 1.28 mHz), 1.70 mHz (exact coincidence), 1.91 mHz (exact coincidence), and 2.25 mHz (2.6% of 2.31 mHz) in the NS direction, and 1.28 mHz (2.29% of 1.31 mHz), 1.33 mHz (1.53% of 1.31 mHz), 1.70 mHz (0.58% of 1.71 mHz), 1.88 mHz (1.57% of 1.91 mHz), and 2.59 mHz (1.52% of 2.63 mHz) in the EW direction.

(a)

(b)

(c)
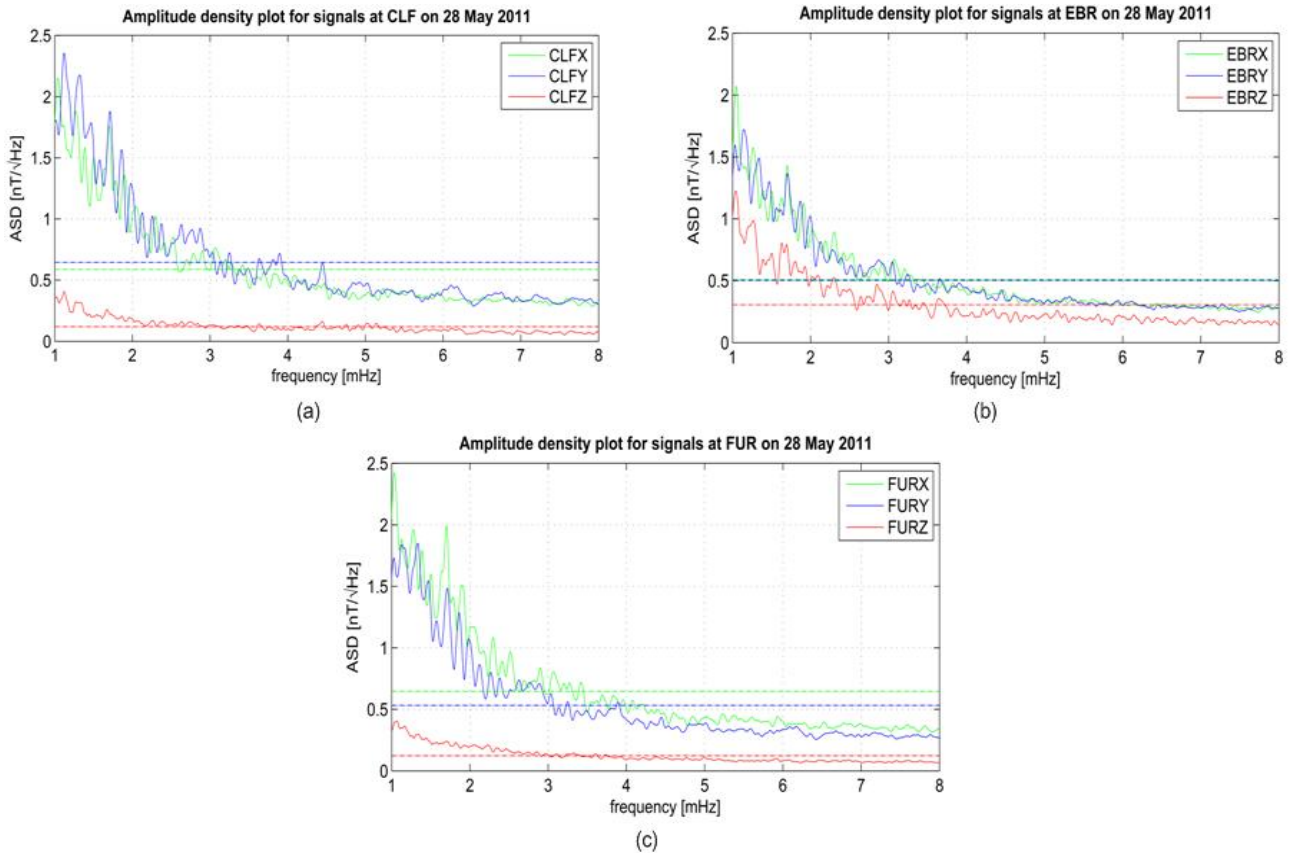
Figure 5.22: Amplitude density plots for signals at CLF, EBR and FUR for the moderate storm on 28 May 2011.

Table 5.16: Frequencies observed in the ULF range from the amplitude density plot of SQUID signals on 28 May 2011.

Sensor: SQUID					
X (NS)		Y (EW)		Z	
Freq (mHz)	ASD (pT/√Hz)	Freq (mHz)	ASD (pT/√Hz)	Freq (mHz)	ASD (pT/√Hz)
1.27	12.66	1.28	12.66	1.25	5.30
1.70	11.67	1.33	11.94	1.39	4.77
1.88	6.81	1.49	13.44	-	-
1.91	5.23	1.70	9.82	-	-
-	-	1.88	7.21	-	-
2.25	3.68	2.04	8.91	-	-
2.77	4.16	2.27	4.25	-	-
2.91	3.55	2.35	7.35	-	-
-	-	2.59	4.16	-	-
-	-	2.89	6.85	-	-
3.14	3.45	3.89	5.95	-	-
3.89	2.86	-	-	-	-
4.49	2.40	-	-	-	-

Table 5.17: Frequencies observed in the ULF range from the amplitude density plot of signals at CLF on 28 May 2011.

Sensor: Fluxgate (CLF)					
X		Y		Z	
Freq (mHz)	ASD (nT/√Hz)	Freq (mHz)	ASD (nT/√Hz)	Freq (mHz)	ASD (nT/√Hz)
1.03	2.14	1.11	2.34	1.12	0.40
1.28	1.87	1.31	2.18	1.68	0.26
1.69	1.75	1.71	1.88	-	-
1.89	1.35	1.86	1.56	-	-
-	-	1.99	1.29	-	-
2.30	1.02	2.63	0.95	2.64	0.16
2.82	0.85	3.25	0.72	-	-
3.06	0.76	3.89	0.72	3.64	0.14
-	-	-	-	4.45	0.16

Table 5.18: Frequencies observed in the ULF range from the amplitude density plot of signals at EBR on 28 May 2011.

Sensor: Fluxgate (EBR)					
X		Y		Z	
Freq (mHz)	ASD (nT/√Hz)	Freq (mHz)	ASD (nT/√Hz)	Freq (mHz)	ASD (nT/√Hz)
1.05	2.06	1.03	1.59	1.04	1.22
1.27	1.56	1.33	1.48	1.26	0.98
1.70	1.43	1.71	1.36	1.70	0.79
1.91	1.12	1.88	1.14	1.94	0.61
-	-	1.99	1.02	-	-
2.31	0.89	2.64	0.63	2.29	0.52
3.08	0.67	3.04	0.65	3.06	0.41
-	-	3.25	0.55	-	-

Table 5.19: Frequencies observed in the ULF range from the amplitude density plot of signals at FUR on 28 May 2011.

Sensor: Fluxgate (FUR)					
X		Y		Z	
Freq (mHz)	ASD (nT/√Hz)	Freq (mHz)	ASD (nT/√Hz)	Freq (mHz)	ASD (nT/√Hz)
1.04	2.42	1.03	1.73	1.06	0.40
1.28	1.95	1.33	1.85	-	-
1.70	1.99	1.72	1.48	-	-
1.91	1.51	1.86	1.27	-	-
-	-	1.98	1.07	-	-
2.31	1.10	2.63	0.74	-	-
2.52	0.96	-	-	-	-
2.91	0.83	-	-	-	-
3.06	0.81	3.04	0.62	-	-
3.42	0.72	3.24	0.56	-	-

70

The frequencies and respective amplitudes for the spectra on 29 May in Figures 5.23 and 5.24 are given in Tables 5.18 to 5.21. Notable frequencies from the fluxgate data were 1.07 mHz, **1.31 mHz**, 1.72 mHz, **1.97 mHz** and 2.55 mHz appearing on the x-components, while 1.16 mHz, 1.52 mHz, 1.76 mHz, **1.91 mHz**, and 2.14 mHz appeared on the y-components. Other frequencies worth noting were 1.35 mHz and 3.19 mHz evident on the y-components of the CLF and EBR data, and **4.25 mHz** on the x-components of the EBR and FUR data.
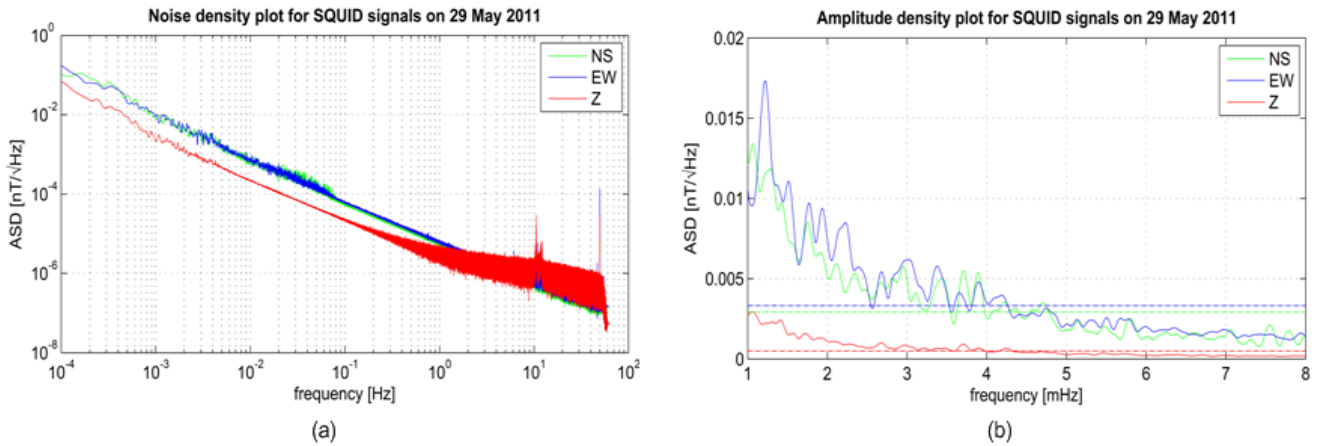
Figure 5.23: Noise and amplitude density spectra for SQUID signals on 29 May 2011.
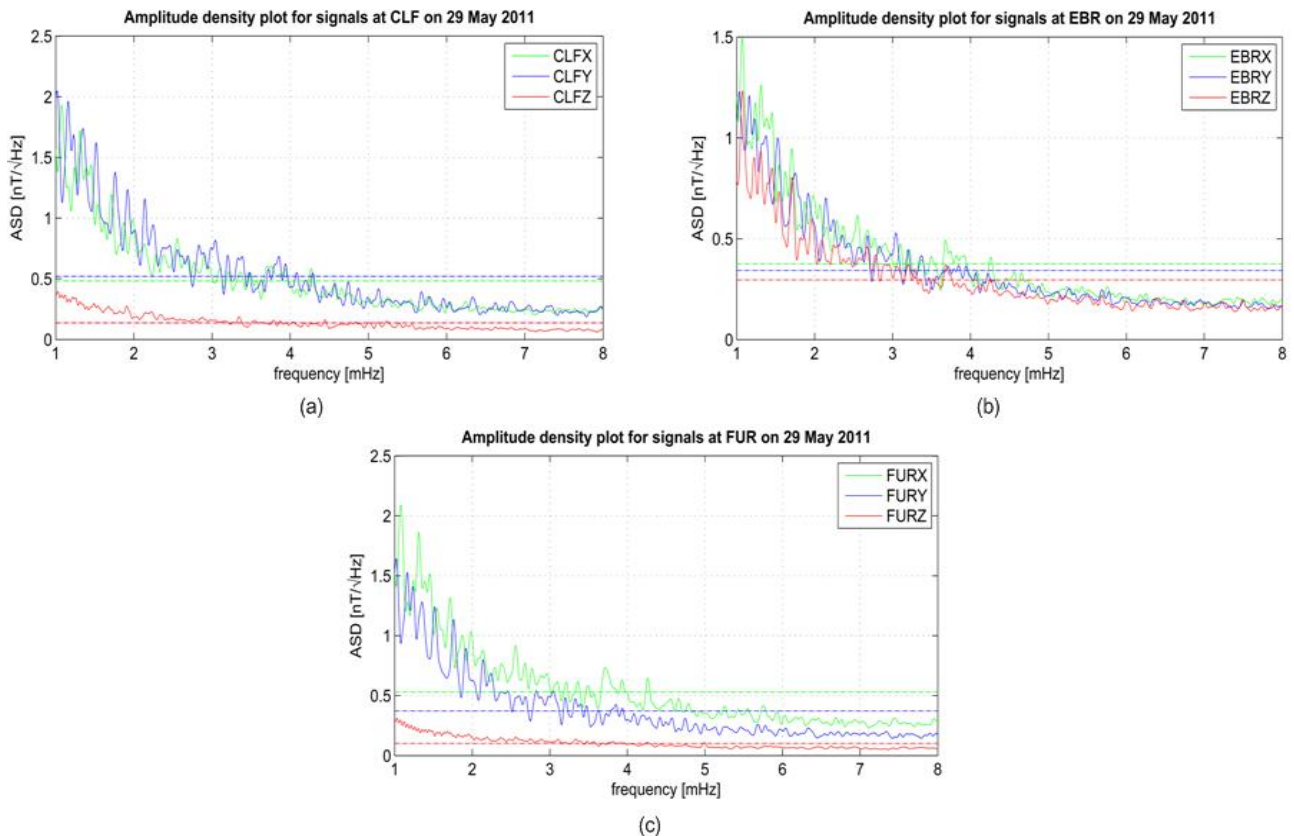
Figure 5.24: Amplitude density spectra for signals at CLF, EBR and FUR on 29 May 2011.

Comparison of the SQUID spectrum against the recurring frequencies from the fluxgate data show coincidence in the NS direction for 1.07 mHz (exact), 1.30 mHz (0.76% of 1.31 mHz), 1.36 mHz (3.82% of 1.31 mHz), 1.68 mHz (4.55% of 1.76 mHz), 1.76 mHz (2.33% of 1.72 mHz), 1.98 mHz (0.51% of 1.97 mHz), 2.56 mHz (0.39% of 2.55 mHz).

In the EW direction, frequency correspondence was at 1.52 mHz, (exact), 1.68 mHz (4.55% of 1.72 mHz), 1.77 mHz (0.57% of 1.76 mHz) and 2.13 mHz (0.46% of 2.14 mHz). There was also coincidence of the NS component at the frequencies 4.22 mHz and 4.26 mHz to the 4.25 mHz peak (noted for EBR and FUR signals) to 93.3% and 98.8% agreement, respectively. In addition, the peak at 1.36 mHz on the EW component was within 0.74% of 1.35 mHz observed on the y-components of CLF and EBR data.

Table 5.20: Frequencies observed in the ULF range from the amplitude density plot of SQUID signals on 29 May 2011.

Sensor: SQUID					
X		Y		Z	
Freq (mHz)	ASD (pT/√Hz)	Freq (mHz)	ASD (pT/√Hz)	Freq (mHz)	ASD (pT/√Hz)
1.07	13.39	1.22	17.34	1.06	2.95
1.30	11.82	1.36	11.42	1.30	3.56
1.36	12.74	1.52	11.04	1.42	2.43
1.68	6.93	1.68	8.32	1.49	3.42
1.76	8.48	1.77	9.73	1.71	1.59
1.98	5.40	1.94	9.39	-	-
2.12	5.94	2.13	6.53	2.01	2.61
2.56	5.76	2.22	8.49	2.38	2.10
2.67	4.78	2.56	4.90	2.68	1.00
2.92	3.32	2.68	5.44	-	-
2.95	5.80	2.91	6.14	-	-
3.44	5.06	3.38	5.77	3.71	0.93
3.71	5.50	3.83	5.16	-	-
3.79	3.77	3.89	4.80	-	-
3.89	5.38	-	-	-	-
4.22	3.55	-	-	4.23	0.67
4.26	2.59	-	-	-	-
4.56	2.66	-	-	-	-
-	-	5.07	3.14	-	-

Table 5.21: Frequencies observed in the ULF range from the amplitude density plot of signals at CLF on 29 May 2011.

Sensor: Fluxgate (CLF)					
X		Y		Z	
Freq (mHz)	ASD (nT/√Hz)	Freq (mHz)	ASD (nT/√Hz)	Freq (mHz)	ASD (nT/√Hz)
1.08	1.93	1.16	1.96	-	-
1.31	1.71	1.35	1.74	-	-
1.72	1.19	1.51	1.61	-	-
1.87	0.96	1.76	1.34	-	-
1.99	0.99	1.93	1.24	-	-
2.55	0.83	2.14	1.16	-	-
2.91	0.69	-	-	-	-
-	-	3.20	0.69	-	-
-	-	3.72	0.58	-	-

Table 5.22: Frequencies observed in the ULF range from the amplitude density plot of signals at EBR on 29 May 2011.

Sensor: Fluxgate (EBR)					
X		Y		Z	
Freq (mHz)	ASD (nT/√Hz)	Freq (mHz)	ASD (nT/√Hz)	Freq (mHz)	ASD (nT/√Hz)
1.07	1.49	1.16	1.21	1.08	1.23
1.31	1.26	1.52	1.00	1.30	0.93
1.71	0.95	1.75	0.82	1.45	0.85
1.97	0.71	1.91	0.72	1.71	0.80
-	-	-	-	1.96	0.60
2.28	0.59	2.14	0.70	2.08	0.49
2.55	0.61	2.67	0.51	2.67	0.46
3.10	0.47	3.04	0.53	3.20	0.37
3.68	0.49	3.19	0.44	-	-
-	-	3.37	0.42	-	-
4.25	0.40	-	-	-	-

Table 5.23: Frequencies observed in the ULF range from the amplitude density plot of signals at FUR on 29 May 2011.

Sensor: Fluxgate (FUR)					
X		Y		Z	
Freq (mHz)	ASD (nT/√Hz)	Freq (mHz)	ASD (nT/√Hz)	Freq (mHz)	ASD (nT/√Hz)
1.08	2.08	1.17	1.52	-	-
1.31	1.86	1.36	1.28	-	-
1.72	1.98	1.52	1.23	-	-
1.98	1.04	1.76	1.13	-	-
-	-	1.91	0.88	-	-
2.57	0.90	2.14	0.80	-	-
3.72	0.74	-	-	-	-
4.27	0.64	-	-	-	-

5.2.4 Case 4 – Intense Storm on August 6

The overview of magnetic activity during August 2011 is shown in Figure 5.25(a) while the hourly degree of disturbance on day 6 of the month is plotted in Figure 5.25(b). The plot shows that there was an intense storm ($D_{st} > 100$) during the hour of 03:00 UTC. The time signals are plotted in Figure 5.26.

(a)   (b)

Figure 5.25: Variation of K_p index over August 2011 and the D_{st} index profile for day 6 of the month. Magnetic activity was significant from late hours of day 5 and climaxed at 03:00 UTC on day 6.
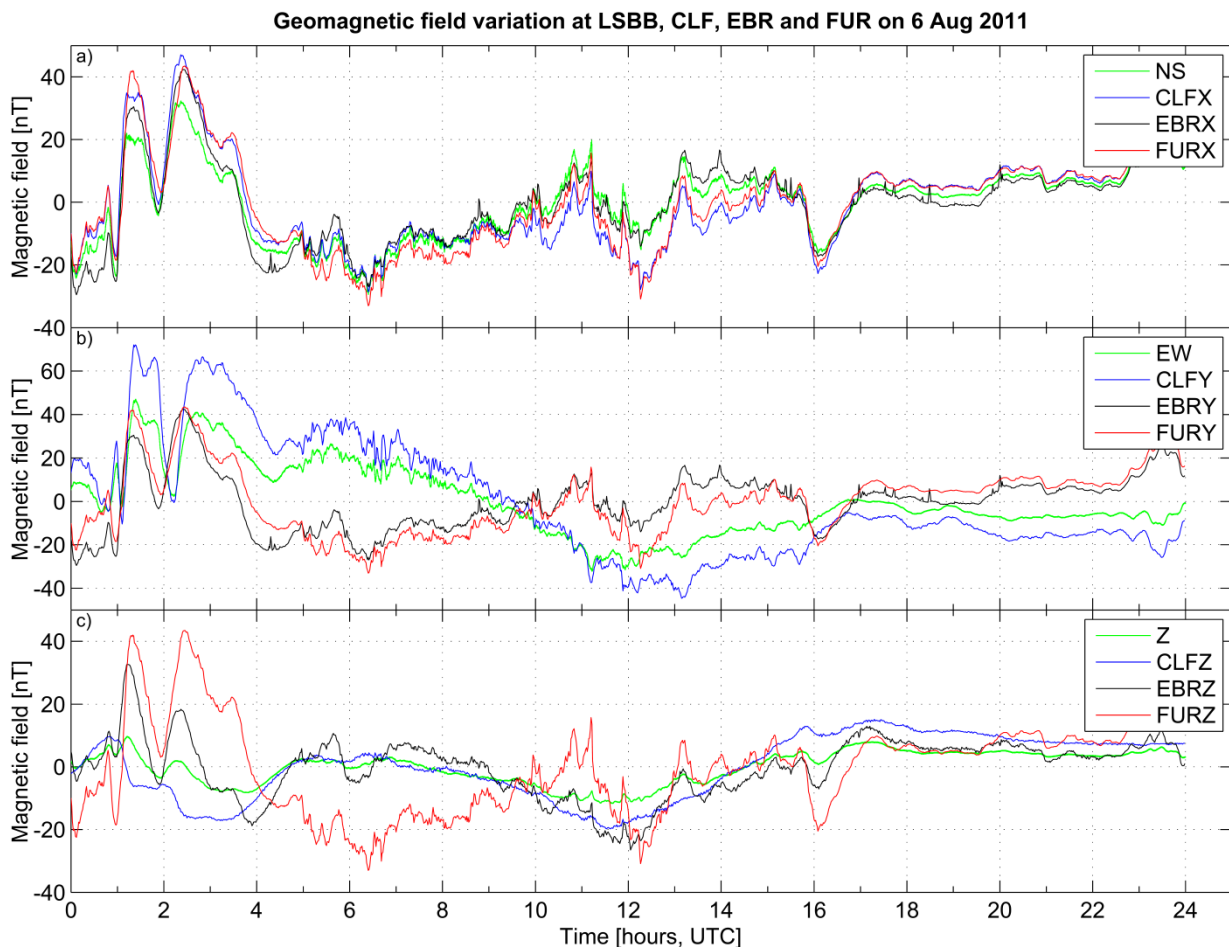
Figure 5.26: Time recordings of magnetic activity on 6 August 2011 at LSBB, CLF, EBR and FUR stations. A major storm occurred in the early hours of the day.

73

Figure 5.27: Noise and amplitude density spectra for signals at LSBB on 6 August 2011.

The noise density plot of the SQUID signals (Figure 5.27(a)) shows Dirac-delta peaks in the low-frequency range of the vertical (Z) component at 10.8 mHz $(0.49 \text{ pT}/\sqrt{\text{Hz}})$, 21.9 mHz $(0.18 \text{ pT}/\sqrt{\text{Hz}})$ and 43.3 mHz, $(0.12 \text{ pT}/\sqrt{\text{Hz}})$. The first two correspond to frequencies in the P_c4 range $(7 - 22 \text{ mHz})$ while the latter falls in the P_c3 range $(22 - 100 \text{ mHz})$. The $1 - 8$ mHz ULF range characteristics of the SQUID data are shown in Table 5.24, while Tables 5.23 to 5.25 show the ULF frequencies obtained from the amplitude density plots of the fluxgate signals in Figure 5.28.
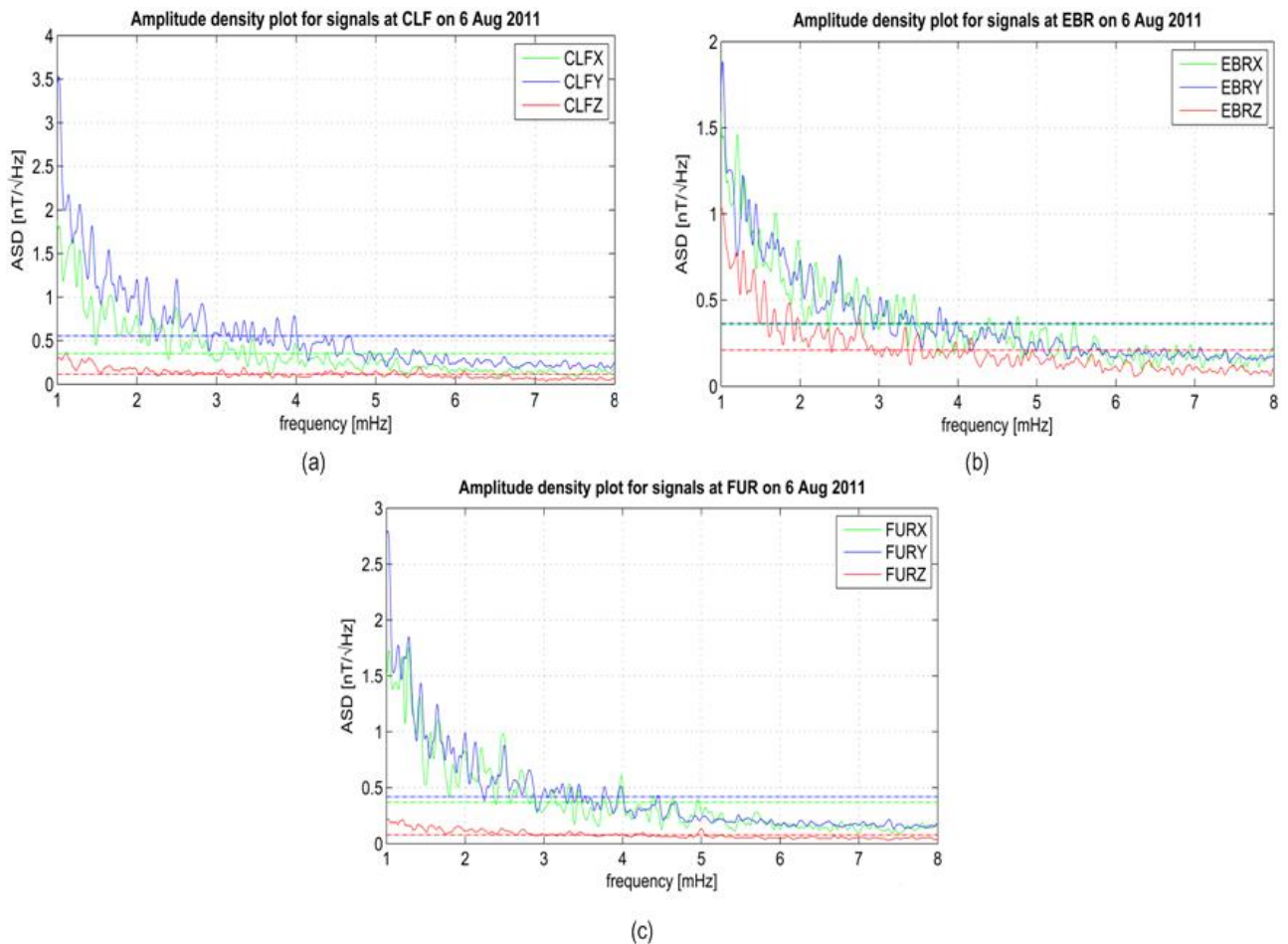
Figure 5.28: Amplitude density spectra for signals at CLF, EBR and FUR on 6 August 2011.

The x-components of the fluxgate data had recurring frequencies (within 5%) of 1.26 mHz, 1.67 mHz, 2.48 mHz, and 2.71 mHz, while **3.44 mHz** was exclusive to CLFX and EBRX signals. The CLFX component also had 99.74% coincidence at **4.00 mHz** with FURX. Agreement of the y-components was at 1.28 mHz, 1.44 mHz, 2.00 mHz, 2.12 mHz, **2.50 mHz** and 2.82 mHz. The CLFY and EBRY components had 99.73% correlation at 3.76 mHz, while CLFY and FURY coincided exactly at 3.97 mHz.

In comparison, the SQUID spectrum coincided with the recurring fluxgate frequencies at 1.28 mHz (1.59% of 1.26 mHz), 1.65 mHz (1.20% of 1.67 mHz), and 2.50 mHz (0.80% of 2.48 mHz) in the NS component. The EW component coincidence at 1.29 mHz (0.78% of 1.28 mHz), 2.13 mHz (0.47% of 2.12 mHz) and 2.50 mHz (0.81% of 2.48 mHz).

Table 5.24: Frequencies observed in the ULF range from the amplitude density plot of SQUID signals on 6 Aug 2011.

Sensor: SQUID					
X (NS)		Y (EW)		Z	
Freq (mHz)	ASD ($pT/\sqrt{Hz}$)	Freq (mHz)	ASD ($pT/\sqrt{Hz}$)	Freq (mHz)	ASD ($pT/\sqrt{Hz}$)
1.20	16.89	1.29	14.36	-	-
1.28	17.09	1.44	12.88	-	-
1.42	11.35	1.65	11.13	-	-
1.65	10.90	1.79	8.75	-	-
2.00	8.11	2.00	0.11	-	-
2.50	9.28	2.13	7.97	-	-
-	-	2.50	8.62	-	-

Table 5.25: Frequencies observed in the ULF range from the amplitude density plot of signals at CLF on 6 Aug 2011.

Sensor: Fluxgate (CLF)					
X (NS)		Y (EW)		Z	
Freq (mHz)	ASD ($nT/\sqrt{Hz}$)	Freq (mHz)	ASD ($nT/\sqrt{Hz}$)	Freq (mHz)	ASD ($nT/\sqrt{Hz}$)
1.29	1.52	1.15	2.17	-	-
1.67	1.02	1.28	2.06	-	-
2.49	0.88	1.44	1.08	-	-
2.74	0.63	1.64	1.54	-	-
-	-	2.00	1.20	-	-
-	-	2.13	1.22	-	-
-	-	2.50	1.20	-	-
-	-	2.82	0.92	-	-
3.45	0.53	3.76	0.76	-	-
-	-	3.97	0.78	-	-
4.00	0.47	-	-	-	-

Table 5.26: Frequencies observed in the ULF range from the amplitude density plot of signals at EBR on 29 May 2011.

Sensor: Fluxgate (EBR)					
X		Y		Z	
Freq (mHz)	ASD ($nT/\sqrt{Hz}$)	Freq (mHz)	ASD ($nT/\sqrt{Hz}$)	Freq (mHz)	ASD ($nT/\sqrt{Hz}$)
1.20	1.46	1.28	1.22	1.28	0.79
1.28	1.21	1.44	1.05	1.41	0.68
1.49	0.91	-	-	1.55	0.64
1.69	1.03	-	-	1.87	0.48
1.97	0.85	-	-	1.97	0.40
2.20	0.72	2.02	0.73	2.75	0.39
2.51	0.73	2.12	0.71	3.34	0.34
2.71	0.63	2.50	0.75	3.49	0.30
2.85	0.58	2.82	0.52	4.17	0.28
3.44	0.53	3.10	0.49	-	-
-	-	3.77	0.45	-	-
4.76	0.40				

Table 5.27: Frequencies observed in the ULF range from the amplitude density plot of signals at FUR on 6 Aug 2011.

Sensor: Fluxgate (FUR)					
X		Y		Z	
Freq (mHz)	ASD ($nT/\sqrt{Hz}$)	Freq (mHz)	ASD ($nT/\sqrt{Hz}$)	Freq (mHz)	ASD ($nT/\sqrt{Hz}$)
1.26	1.76	1.29	1.83	-	-
1.42	1.30	1.43	1.43	-	-
1.67	1.10	1.64	1.24	-	-
1.99	0.83	-	-	-	-
2.20	0.85	2.00	0.99	-	-
2.48	0.98	2.12	0.90	-	-
2.72	0.66	2.49	0.87	-	-
-	-	2.82	0.66	-	-
3.32	0.53	3.44	0.53	-	-
3.99	0.61	3.97	0.51	-	-

5.2.5   Case 5 – Intense Storm on September 26

September 2011 was magnetically quite active with $K_p > 5$ on five days of the month (Figure 5.29(a)). The most intense activity was on day 26 of the month, for which the hourly D_{st} index values are plotted in Figure 5.29(b). Time signals are shown in Figure 5.30.
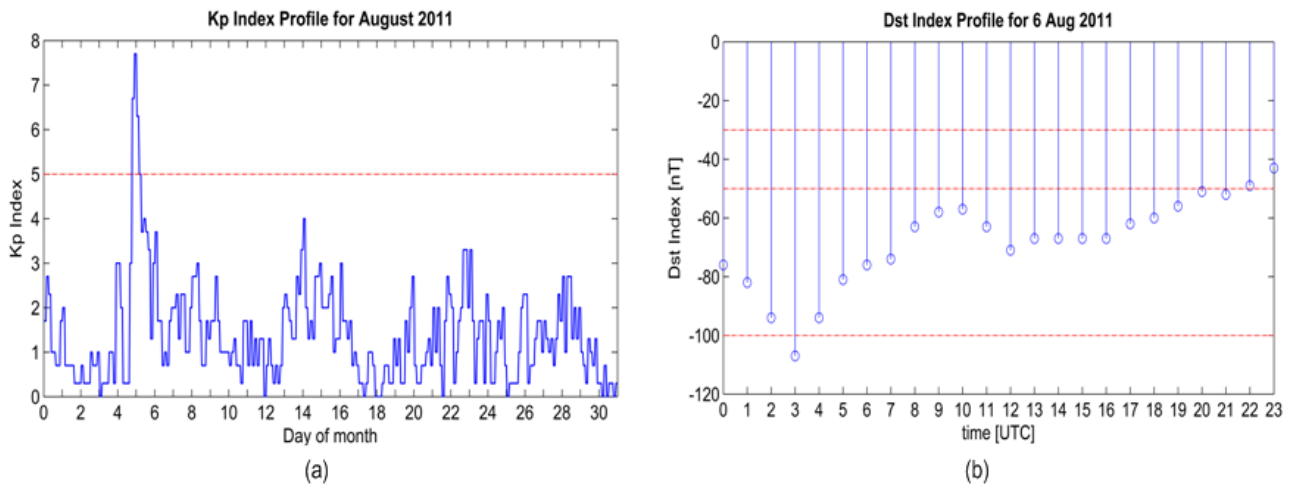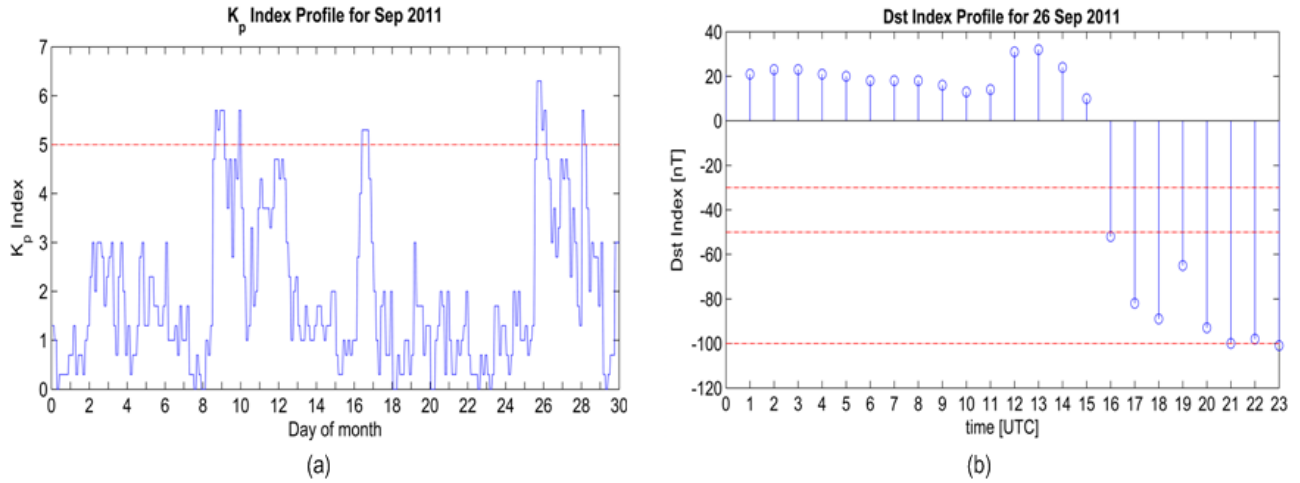

Figure 5.29: Variation of K_p index over September 2011 and the D_{st} index profile for day 26 of the month. Magnetic activity was moderate from about 16:00 UTC and reached a climax at 21:00 UTC.
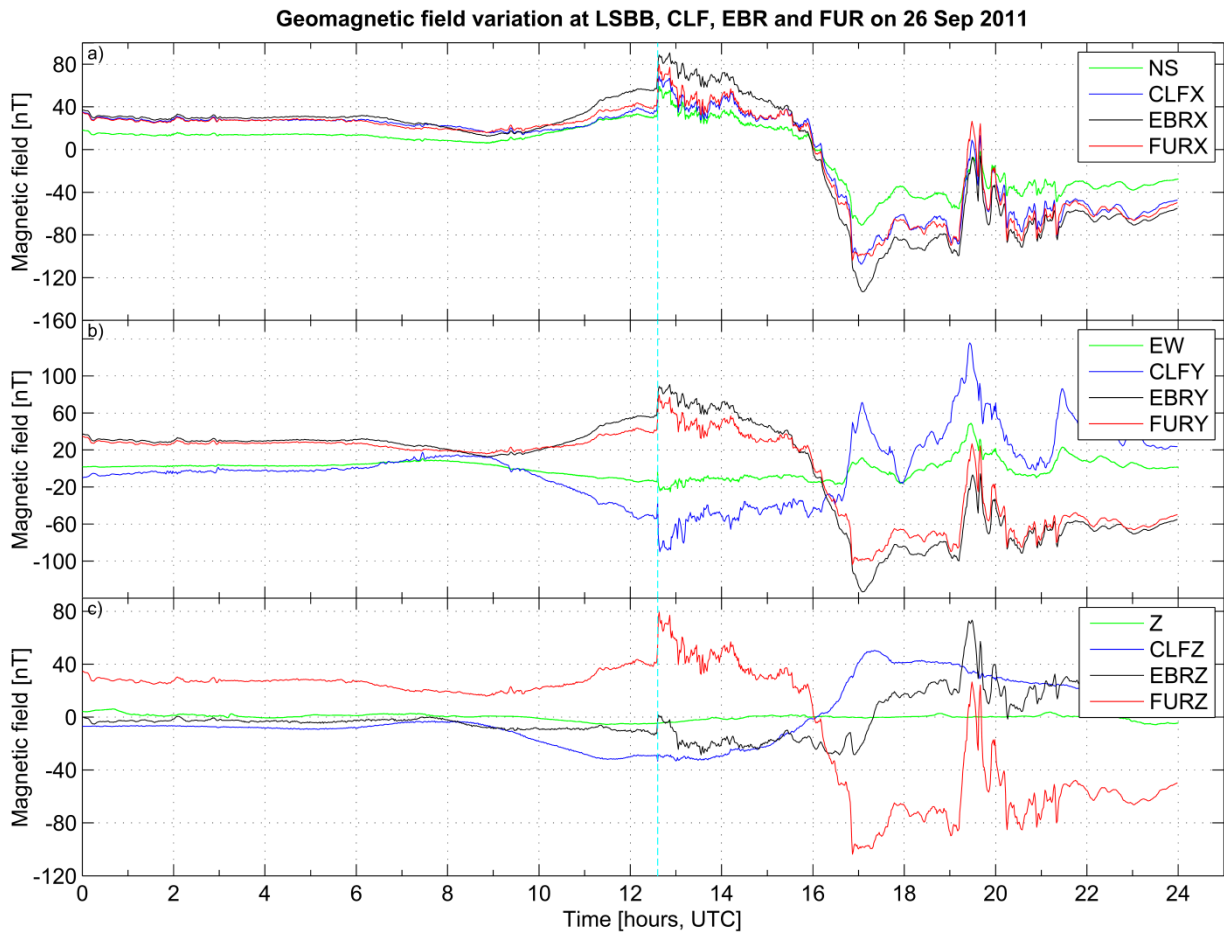
Figure 5.30: Time recordings of magnetic activity on 26 September 2011 at LSBB, CLF, EBR and FUR stations. The SSC (sudden storm commencement occurred around 12:30 UTC).
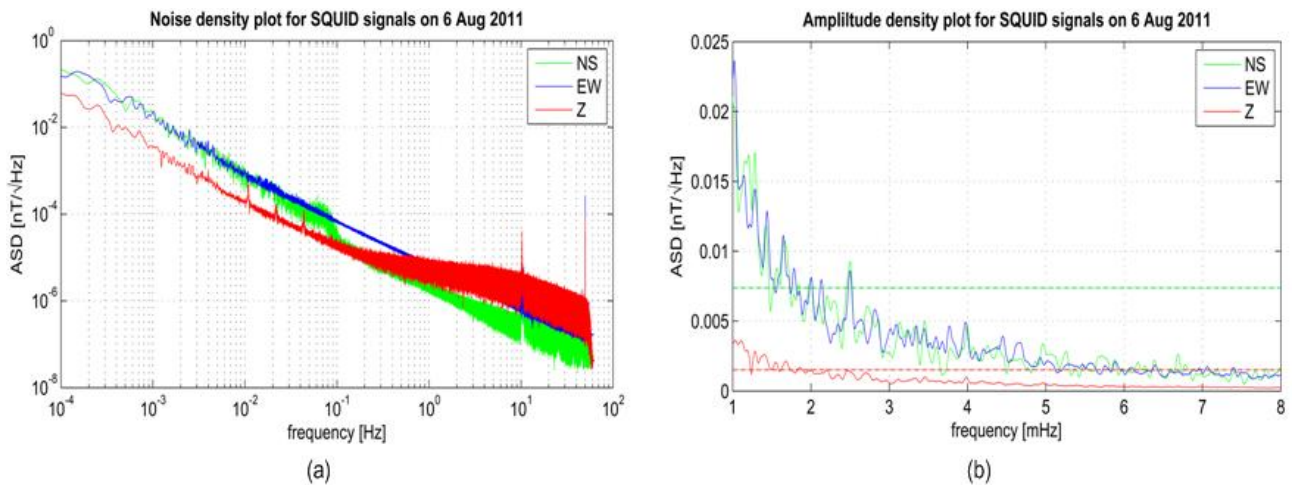
76

(a)

(b)
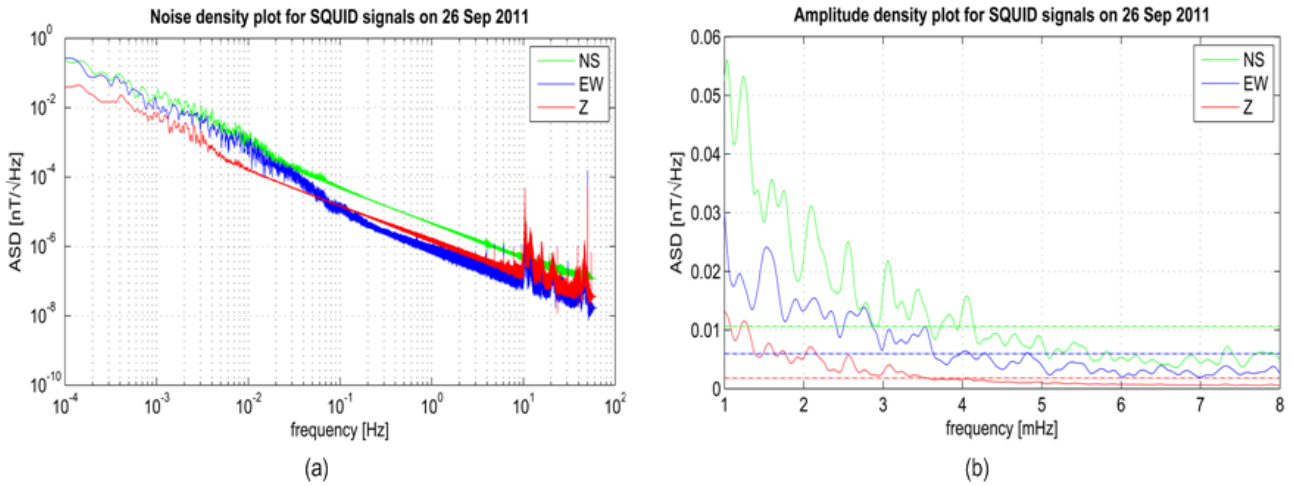
Figure 5.31: Noise and amplitude density spectra for signals at LSBB on 26 September 2011.

The noise density plot of the SQUID signals (Figure 5.31(a)) shows Dirac-delta peaks at 4.81 Hz $(0.86 \text{ fT}/\sqrt{\text{Hz}})$ on the vertical (Z) component, 7.81 Hz $(0.91 \text{ fT}/\sqrt{\text{Hz}})$ on both EW and Z components, and 9.62 Hz with amplitude densities of $0.88 \text{ fT}/\sqrt{\text{Hz}}$ and $1.15 \text{ fT}/\sqrt{\text{Hz}}$ on the Z and EW components, respectively. The ULF frequencies of the SQUID amplitude density spectrum are shown in Table 5.26, while the frequencies observed on the fluxgate spectra (Figure 5.32) are given in Tables 5.27 to 5.29.

(a)

(b)

(c)
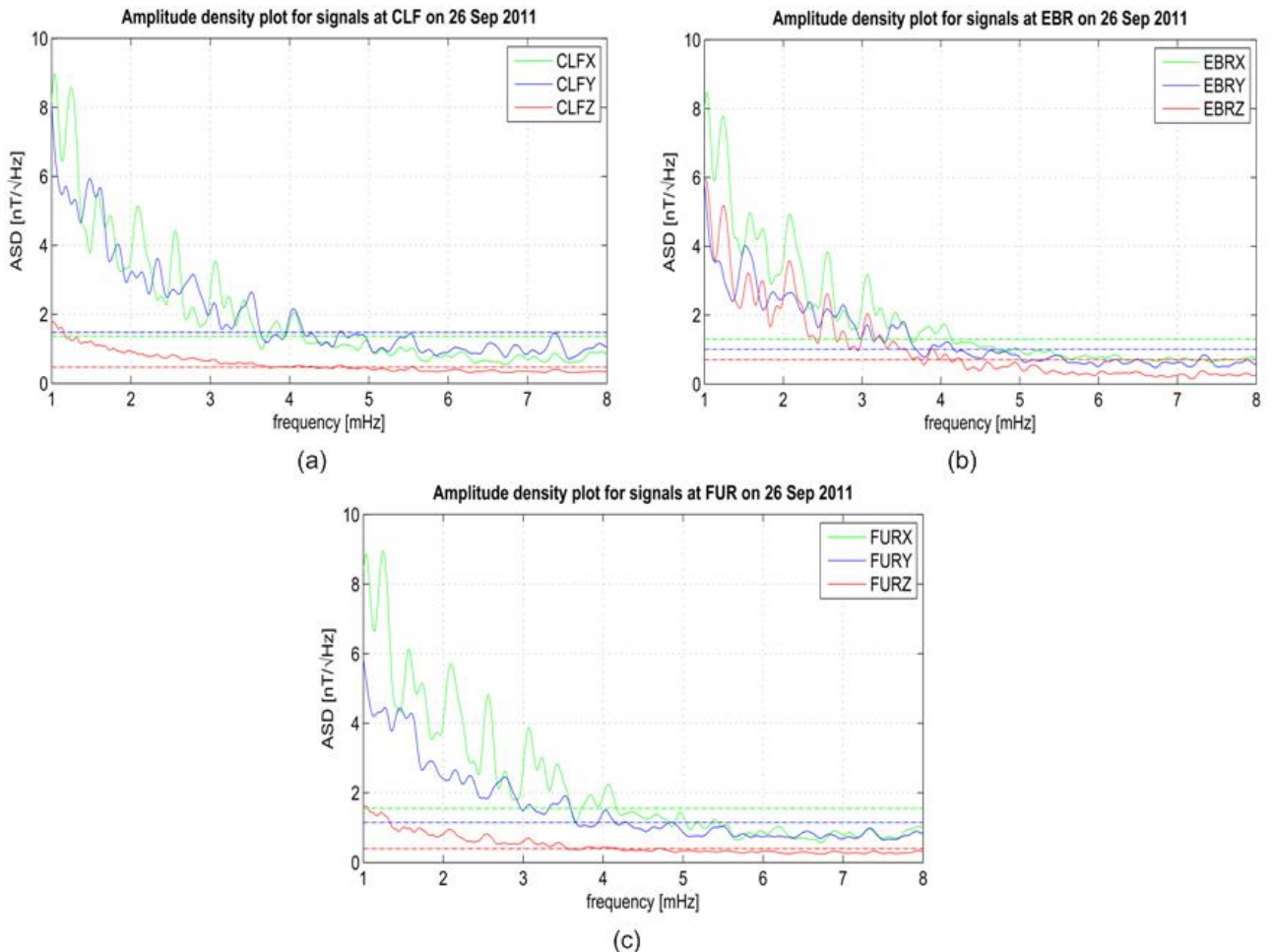
Figure 5.32: Amplitude density spectra for signals at CLF, EBR and FUR on 26 September 2011.

The x-components of the fluxgate signals coincided at 1.23 mHz, 1.58 mHz, 2.09 mHz, **2.56 mHz** and 3.06 mHz, while the y-components coincided at frequencies of 1.48 mHz, 2.34 mHz and **3.51 mHz**. The CLFX and FURX components coincided exactly at **3.42 mHz** and within 99.51% at 4.05 mHz. Against this, the SQUID spectrum coincided at 1.25 mHz (1.63% of 1.23 mHz), 1.59 mHz (0.63% of 1.58 mHz) and 3.06 mHz (exact) for the NS component, and 1.52 mHz (2.70% of 1.48 mHz) and 3.55 mHz (1.14% of 3.51 mHz) for the EW component.

The NS component of the SQUID data was also in good agreement with CLFX and FURX components at 3.42 mHz (exact) and at 4.06 mHz, with 0.25% deviation of the NS value.

Table 5.28: Frequencies observed in the ULF range from the amplitude density plot of SQUID signals on 26 Sep 2011.

Sensor: SQUID (12 to 24 UTC)					
X		Y		Z	
Freq (mHz)	ASD (pT/√Hz)	Freq (mHz)	ASD (pT/√Hz)	Freq (mHz)	ASD (pT/√Hz)
1.25	52.90	1.52	24.11	1.25	11.53
1.59	35.69	3.07	10.14	2.56	5.63
1.74	33.80	3.55	10.62	-	-
2.09	31.17	-	-	-	-
2.55	24.91	-	-	-	-
3.06	21.79	-	-	-	-
3.43	16.93	-	-	-	-
4.05	15.83	-	-	-	-

Table 5.29: Frequencies observed in the ULF range from the amplitude density plot of signals at CLF on 26 Sep 2011.

Sensor: Fluxgate (CLF, 12 to 24 UTC)					
X (NS)		Y (EW)		Z	
Freq (mHz)	ASD (nT/√Hz)	Freq (mHz)	ASD (nT/√Hz)	Freq (mHz)	ASD (nT/√Hz)
1.03	8.96	1.48	5.93	-	-
1.25	8.56	1.84	4.03	-	-
1.58	5.51	-	-	-	-
2.09	5.12	2.33	3.61	-	-
2.56	4.41	-	-	-	-
3.06	3.53	3.05	2.33	-	-
3.42	2.40	3.52	2.64	-	-
4.06	2.05	4.05	2.16	-	-

Table 5.30: Frequencies observed in the ULF range from the amplitude density plot of signals at EBR on 26 Sep 2011.

Sensor: Fluxgate (EBR, 12 to 24 UTC)					
X		Y		Z	
Freq (mHz)	ASD (nT/√Hz)	Freq (mHz)	ASD (nT/√Hz)	Freq (mHz)	ASD (nT/√Hz)
1.23	7.76	1.53	4.01	1.23	5.18
1.58	4.98	-	-	1.56	3.22
1.74	4.51	-	-	1.74	3.00
2.09	4.94	2.34	2.38	2.08	3.57
2.57	3.83	2.76	2.29	2.56	2.61
3.06	3.18	3.07	1.72	3.07	2.04
-	-	3.51	1.81	-	-

Table 5.31: Frequencies observed in the ULF range from the amplitude density plot of signals at FUR on 26 Sep 2011.

| Sensor: Fluxgate (FUR, 12 to 24 UTC)					
X		Y		Z	
Freq (mHz)	ASD (nT/√Hz)	Freq (mHz)	ASD (nT/√Hz)	Freq (mHz)	ASD (nT/√Hz)
1.24	8.95	1.46	4.43	-	-
1.58	6.11	1.86	2.91	-	-
2.09	5.70	2.15	2.66	-	-
2.56	4.81	2.34	2.50	-	-
3.06	3.86	3.53	1.91	-	-
3.42	2.83	-	-	-	-
4.06	2.25	4.03	1.50	-	-

5.3 Summary of Storm-time Observations

For all five storms considered, there were fewer frequency peaks identified than on a quiet day. This suggests that the energy increase in the geomagnetic spectrum during disturbed conditions is concentrated across selected frequency bands. The energy increase can be seen from the larger storm-time amplitude densities.

Although this is not a study on pulsations, it is worth noting that some of the recurring frequencies observed correspond specifically to values attributed to field line resonances (FLRs) in the magnetosphere, namely 1.3 mHz, 1.91 mHz, 2.6 mHz, 3.4 mHz and 4.2 mHz [63]. Due to their frequent recurrence in various geomagnetic studies of ULF waves, these frequencies are also often referred to as "magic" frequencies. Taking values within 5%, the most recurring "magic" frequency (on both fluxgate and SQUID signals) was 2.6 mHz.

The comparisons between the frequency components of the SQUID and fluxgate datasets are summarized in Table 5.32. The frequencies recurring on the x- and y-components of the fluxgate data are represented by X and Y, respectively, while SQUID components coinciding within 5% of the fluxgate values are represented by NS and EW.

Overall, there was at least 59% agreement between the fluxgate and SQUID observations, where correspondence is with respect to recurring frequencies from all three fluxgate datasets considered. Correspondence between LSBB (SQUID) and a single observatory have been neglected in order to emphasize regional correlation rather than local or isolated features.

Table 5.32: Summary of recurring frequencies on fluxgate channels and coincidence to SQUID channels.

Case 1				Case 2				Case 3				Case 4				Case 5			
Frequency (Hz)				Frequency (Hz)				Frequency (Hz)				Frequency (Hz)				Frequency (Hz)			
X	NS	Y	EW	X	NS	Y	EW	X	NS	Y	EW	X	NS	Y	EW	X	NS	Y	EW
1.18	1.12	1.18	2.24	1.30	1.74	1.31	1.37	1.03	1.27	1.03	1.28	1.26	1.26	1.28	1.29	1.23	1.25	1.48	1.52
1.46	1.42	1.46	2.59	1.74	2.10	1.39	1.58	1.28	1.70	1.33	1.33	1.67	1.65	1.44	2.13	1.58	1.59	2.34	3.55
1.78	1.74	1.75	2.83	1.91	2.61	1.53	1.94	1.70	1.91	1.71	1.70	2.48	2.50	2.00	2.50	2.09	3.06	3.51	
2.51		1.93		2.05		2.21	2.43	1.91	2.25	1.86	1.88	2.71		2.12		2.56			
		2.22		2.60		2.46	2.46	2.31		2.63	2.59			2.50		3.06			
		2.56				2.70	3.34	3.06		3.25				2.82					
		2.72				3.34													
75%		43%		60%		86%		67%		83%		75%		50%		60%		67%	
59%				73%				75%				63%				64%			

The agreement between the SQUID and fluxgate data affirm the reliability of SQUID magnetometers as instruments to complement geophysical research with regards to magnetic field monitoring. This is an important result since little work has been done on the investigation of various geophysical phenomena using SQUID data.

6 Summary and Conclusion

Highlights of the Study and Recommendations

Superconductivity was briefly discussed in Chapter 1, introducing SQUID sensors and their application as instruments for geophysical research with regard to investigating ionospheric and seismic coupling to geomagnetic activity. The influence of solar activity on the near-space environment was reviewed in Chapter 2, stating the characteristics of magnetically disturbed conditions in terms of magnetic field perturbations and ionospheric variability. This was concluded with an overview on the information extracted from conventional magnetic measurements. Following a more detailed discussion on SQUID theory, the key concepts of advanced magnetometry were presented in Chapter 3. The main difference to conventional magnetometry is the capability of detecting the magnetic influence of small-scale ionospheric perturbations, some of which are associated with seismic activity. The theory and procedure for analyzing these magnetic signals was the subject of Chapter 4, and a comparative study between fluxgate and SQUID data was undertaken in Chapter 5. This demonstrated the good correspondence between SQUID and fluxgate signals for geomagnetic storms in 2011.

6.1 Significance of the Study

Fast Fourier Transforms (FFTs) are widely used in various engineering and science disciplines to examine the frequency content of discretely sampled data. However, the associated spectra often lack consistency with the analytic expressions. A common error is the lack of distinction between the definitions of the power spectral density (PSD) and the energy spectral density (ESD). In this study we have shown from first principles how these spectra arise naturally from Parseval's theorem – a conservation law for the total power in a signal, and hence obtained discrete formulae that are consistent with the physical meaning of those quantities. In particular, we outlined the procedure to obtain the frequency spectrum of discrete data yielding an amplitude spectrum (AS) with amplitudes equal to the input signal. This was illustrated using an artificially generated signal in MATLAB. Though a very basic undertaking, this is very important for magnetometry with respect to the determination of noise floors. If the FFT is not properly scaled – which tends to be the case due to the use of different conventions and/or formulae – the noise density amplitudes will be false and hence result in wrong conclusions. The computation of the FFT presented here has been examined carefully to ensure consistency with LSBB. Thus any interested parties wishing to reproduce results from LSBB or Hermanus will be able to do so with ease, having this work as a reference.

Our results also show the effectiveness of the Wiener-Khintchine theorem (Section 4.3.3) in smoothing the spectra of noisy data. The theorem requires that the autocorrelation function first be computed and this function is then Fourier-transformed to obtain a power spectrum (nT^2). The amplitude spectral density (ASD) can then be obtained by first multiplying the power spectrum by the duration T, and then taking the square root to obtain units of $\mathrm{nT}/\sqrt{\mathrm{Hz}}$.

The autocorrelation function is a comparison of a signal with itself, either at corresponding samples (zero-lag) or with displacement in time (lag). Since there is no covariance between random components from one lag to another, the

autocorrelation function easily reduces noise. It is thus a natural statistical procedure that in fact normalizes a signal by the variance of its samples so that the output contains the most probable values based on a normal distribution. The extent to which noise is reduced depends on size of lag, with a longer lag making low-frequency phenomena more obvious. In this study, the lag was chosen as a quarter of the number of samples of a signal. This proved to be an optimum choice across all frequencies.

More importantly, this study has shown that there is good coincidence between SQUID and fluxgate measurements yielding a 59% correlation at the very least. The correlation was based only on the recurrent frequency components at three INTERMAGNET observatories around LSBB, focusing on geomagnetic storms during 2011. Hence, while the shielding at the LSBB is ideal for monitoring faint magnetic signals, it has been shown that the SQUID magnetometer performs well even during strong perturbations of the field. In fact, the frequency spectrum suggests a rich distribution of physical phenomena such as geomagnetic pulsations and Schumann resonance. Pc1 (0.2 – 5 Hz) frequencies were observed between 0.1 and 1 Hz on the noise density spectrum of the SQUID data on 1 March 2011, while frequencies in the Pc5 $(1 - 7\ \text{mHz})$ range were present for literally every storm considered. Though frequencies in the Pc1 range did not recur, we note that if pulsations in this range are present during a storm, the information will be contained in the SQUID data.

The manifestation of a global, electric field excitation (Schumann resonance) was indicated by the appearance of a 7.81 Hz peak on the noise density plot of the SQUID data for the storm on 26 September 2011. Such observations cannot be made on fluxgates due to the low sampling frequency ($\sim$16.7 mHz) used at many observatories. Clearly, SQUID magnetometers are a good complement to fluxgate measurements.

6.2   Limitations and Recommendations for Future Research

Considering the natural coupling that exists between the geomagnetic field and the ionosphere, it would have been ideal to examine some ionospheric parameters such as f_0F_2 (maximum frequency of the F_2 layer), and how they are affected by energy transport in the magnetosphere due to field-line resonances (FLRs).

It has been reported that the signals arriving at LSBB during quiet days are a global magnetic response. How this may change during intense magnetic activity is unclear. A comparison to fluxgate data at different latitudes could give some insights into this. And while LSBB data have shown similarity in quiet day variation and Pc5 pulsations to observatories close to the north pole, no correlations have been performed for observatories in the southern hemisphere. This study in particular used data from stations within 5° of latitude with respect to each other, and hence it remains unclear to what degree a global magnetic response is recorded.

In this regard, we recommend the following:

a)   Undertake a detailed study to investigate the correlation between SQUID data and perturbations in the ionosphere. A comparison of the frequencies associated with the ionospheric, wave-like perturbations and the magnetic spectrum would be very significant. SQUID data from Hermanus would be ideal for this research since ionosonde data are available locally.

b) Perform a longer term survey of the frequencies associated with magnetically disturbed conditions using data over a two to three year span. The results should be categorized according to minor, moderate and intense storms, in order to identify the main "role players" in each of these categories.

c) Investigate the correlation between SQUID data at LSBB and Hermanus in order to verify the near-field response to electromagnetic effects.

Appendices

Downloading and processing LSBB Data

A.1   Downloading Data

LSBB data is accessible at http://www.lsbb.eu/spip.php?rubrique218 under the "Data Access" pane. Magnetometer data is indicated by the letters MGN, while all other data are for seismic recordings. Note that there is also an English site (http://lsbb.oca.eu/spip.php?rubrique206) but the Data Access window is not available. If download failures are encountered on the French site, chances are the users IP address may be outdated or there might be some restrictions imposed on the network by the Administrator. One efficient way to download the data, particularly for multiple files, is via an FTP download using a program like *wget.* This downloads data via the terminal in Linux and the command window in Windows by logging onto the server directly. Wget is normally a default application in Linux but if it is missing, it can be installed by running the command `sudo apt-get install wget` in the terminal. For Windows, wget.exe can be downloaded at http://users.ugent.be/~bpuype/cgi-bin/fetch.pl?dl=wget/wget.exe and must be saved in the directory in which the command window is opened.

A manual providing wget guidelines and commands is available at http://www.gnu.org/software/wget/manual/wget.html. If the download still fails while using wget, reasons might be a network failure or an old IP address. On Windows systems, some anti-viruses might also hinder the download and might thus need to be disabled for the download to proceed.

A.2   Data Processing

A simple code for reading SEGY files into MATLAB and plotting the time signals is shown below. The code was made available by Dr. Elisabeth Pozzo di Borgo (Université d´Avignon et des Pays du Vaucluse). It requires the user-defined functions *lire_segy_head* and *lire_segy_data* to run successfully. These functions are available from LSBB on request.

```
clear all
close all
clc
% File name to read au format segy (one component)
data_file_name = 'X:\LSBB_SEGY_Data\MGN\2011.09.08-23.59.59.FR.MGN.00.HGE.SEGY'
delay = 0*3600+0*60+0; %  delay from the beginning the file beginning
winlength = 0.5*3600 ;  % length of the temporal signal in secondes
% File Reading : header then data
prhd = lire_segy_head(data_file_name,'ieee-le'); %preliminary header
[amplitude,head] = lire_segy_data(data_file_name,prhd,delay,winlength);
transducer_coefficient = 1/(20*0.83);   % SQUID in low sensitivity (20Phi0)
sensitivity = 2*20/(2^32); % input +/- 20V ; codage 32 bits
amplitude =  -(amplitude-mean(amplitude) ) * sensitivity / transducer_coefficient;%
convert data in nT
dt = head.deltaSample/1000000
time = (0:dt:(length(amplitude)-1)*dt);
plot (time, amplitude)
```

A.3   Computing the Amplitude Spectral Density using the Wiener-Khintchine Theorem

The program below plots the amplitude spectral density (ASD) by computing the FFT of the autocorrelation function. This output is actually the square of the FFT amplitude that would be obtained Fourier transforming the signal directly. The FFT of the autocorrelation function is then multiplied by the duration T in order to obtain a PSD. The ASD is then obtained as the square root of the PSD.

```matlab
% Computation of frequency spectra using the Wiener-Khintchine theorem

clear all
close all
clc

delay=0*3600+0*60+0; %  delay from the beginning the file beginning
winlength = 12*3600;  % length of the temporal signal in seconds

% load squid data
% data_file_name1 = HGN(x-comp),data_file_name2 = HGE(y-comp),data_file_name3 = HGZ (z-comp)
data_file_name1 = 'X:\SQUID_Data\2011.01.29-00.00.00.FR.MGN.00.HGN.SEGY';
data_file_name2 = 'X:\SQUID_Data\2011.01.29-00.00.00.FR.MGN.00.HGE.SEGY';
data_file_name3 = 'X:\SQUID_Data\2011.01.29-00.00.00.FR.MGN.00.HGZ.SEGY';
% LSBB, Rustrel, France: Geodetic Latitude: 43.9; Geodetic Longitude: 5.5 approx

% File Reading : header then data
prhd1 = lire_segy_head(data_file_name1,'ieee-le');  %preliminary header
prhd2 = lire_segy_head(data_file_name2,'ieee-le');
prhd3 = lire_segy_head(data_file_name3,'ieee-le');

[NS,headx] = lire_segy_data(data_file_name1,prhd1,delay,winlength);
[EW,heady] = lire_segy_data(data_file_name2,prhd2,delay,winlength);
[VZ,headz] = lire_segy_data(data_file_name3,prhd3,delay,winlength);

%% squid output in nanotesla
transducer_coefficient = 1/(20*0.83);  % SQUID in low sensitivity (20Phi0)
sensitivity = 2*20/(2^32);% input +/- 20V ; codage 32 bits
NS = -(NS-mean(NS)) * sensitivity/transducer_coefficient;% convert data in nT
EW = -(EW-mean(EW)) * sensitivity/transducer_coefficient;
VZ = -(VZ-mean(VZ)) * sensitivity/transducer_coefficient;

dt1 = headx.deltaSample/1000000; % sampling interval in seconds
fs1 = 1/dt1; % sampling frequency of SQUID data (125Hz for HG);
l = length(NS);
Nn = 2^nextpow2(l); % number of fft points as a power of 2
f1 = (0:Nn-1)*fs1/Nn; % frequency axis of squid data
time1 = 0:dt1:(l-1)*dt1;

% Spectral analysis
lag = 0.25*l; % define according to whether interested in low or high frequencies. For high frequencies lag ~ l
NS = detrend(NS);
EW = detrend(EW);
VZ = detrend(VZ);
NS = 2*xcorr(NS,lag,'unbiased');
NS(1:lag) = [];
NS = 2*NS .* hanning(length(NS),'periodic'); % Hann window has best tread off for fequency resolution and amplitude accuracy
EW = xcorr(EW,lag,'unbiased');
EW(1:lag) = [];
EW = 2*EW .* hanning(length(EW),'periodic');
VZ = xcorr(VZ,lag,'unbiased');
VZ(1:lag) = [];
VZ = 2*VZ .* hanning(length(VZ),'periodic');
```

84

```matlab
ESD_squidx = 2*abs(fft(NS,Nn)/length(NS)); % Wiener-Khinchin theorem, ESD = energy
spectral density in nT^2
ESD_squidy = 2*abs(fft(EW,Nn)/length(EW));
ESD_squidz = 2*abs(fft(VZ,Nn)/length(VZ));

ASD_squidx = sqrt(ESD_squidx*(l*dt1)); % amplitude spectral density, nT/sqrt(Hz);
ASD_squidy = sqrt(ESD_squidy*(l*dt1));
ASD_squidz = sqrt(ESD_squidz*(l*dt1));

figure,loglog(f1(1:Nn/2),ASD_squidx(1:Nn/2),'g',f1(1:Nn/2),ASD_squidy(1:Nn/2),'b',f1(1:Nn
/2),ASD_squidz(1:Nn/2),'r'),grid,legend('NS','EW','Z')
title('Noise density plot for SQUID signals on a quiet day 2011','FontWeight','bold',...
    'FontSize',12),
xlabel('frequency [Hz]','FontSize',12),ylabel('Amplitude spectral density
[nT/{\surd}Hz]','FontSize',12)
```

References

[1]   T. P. Orlando, K. A. Delin, "Foundations of Applied Superconductivity", Addision-Wesley Publishing Company, Inc., Massachusetts, 1991, pp 1, 31

[2]   T. P. Orlando, K. A. Delin, "The Electrical Engineering Handbook", CRC Press, Boca Raton, FL, 1993, pp. 1114–1123.

[3]   E. F. van der Merwe, W. J. Perold, "An Introduction to Superconductivity", in the 8th South African Symposium on Antennas and Propagation and Microwave Theory and Techniques, University of Stellenbosch, 1994, pp 19.

[4]   D. Bertrand, "A Relativistic BCS Theory of Superconductivity", Universit´ecatholique de Louvain Facult´e des Sciences, D´epartement de Physique, PhD Thesis, 2005, pp15, 16

[5]   J. Bardeen, *et al*, "Theory of Superconductivity", Physical Review, Vol 108, Num 5, 1957, pp 1176, 1178 – 1204.

[6]   P. L. Richards, *et al*, "Student Laboratory demonstration of Flux Quantization and the Josephson Effect in Superconductors", American Journal of Physics, Vol. 36, No 8, 1968, pp 691, 692

[7]   H. Hayakawa, N. Nobuyuki, *et al*, "Superconducting Digital Electronics", Proceedings of the IEEE, Vol. 92, No. 10, October 2004, pp 1549, 1550.

[8]   S. P. Benz, C. Hamilton, "Application of the Josephson Effect to Voltage Metrology", in Proceedings Of the IEEE, Vol. 92, No. 10, October 2004, pp 1618.

[9]   R. P. Feynman, *et al*, "The Feynman Lectures on Physics", Addision-Wesley Publ. Co., Chapter 21, Vol. 3, 1965, pp 21-17

[10]   A. A. Abrikosov, "On the Magnetic Properties of Superconductors of the Second Group", Soviet Physics JETP Vol. 5, No. 6, December 1957, pp 1174

[11]   A. Rydh, "Vortex Properties from Resistive Transport Measurements on Extreme Type-II Superconductors", Doctoral Dissertation, Solid State Physics, Dept. of Physics & Dept. of Electronics, Royal Institute of Technology (KTH), Stockholm 2001, pp 10, 15

[12]   B. Rosenstein, D. Li, "Ginzburg-Landau theory of type II superconductors in magnetic field", Reviews of Modern Physics, Vol. 82, January–March 2010, pp112

[13]   G. Waysand, J. Marfaing, *et al*, "Earth–ionosphere Couplings, Magnetic Storms, Seismic Precursors and TLEs: Results and Prospects of the [SQUID]² System in the low-noise Underground Laboratory of Rustrel-Pays d'Apt", Comptes Rendus Physique, Elsevier Masson SAS (for Académie des Science) Vol. 12, Is. 2, 2011, pp 192 – 202.

[14]   J. J. Love, "Magnetic Monitoring of Earth and Space", American Institute of Physics, Physics Today, 2008, pp 31

[15]   G. Waysand, P. Barroy, *et al*, "Seismo-ionosphere detection by underground SQUID in low-noise environment in LSBB-Rustrel, France", The European Physical Journal, Applied Physics, Vol. 47, Is. 1, 2009, pp 1 – 4.

[16]   J. Marfaing, E. Pozzo di Borgo, *et al*, "Global Observation of 24 November Pc5 Pulsation by Single Mid-latitude Underground [SQUID]² System", Annales Geophysicae, Vol. 29, pp 1977 – 1884, 2011

[17]   T. E. Cravens, "Physics of Solar System Plasmas", Cambridge University Press, 1997, pp 159 – 167, 181 – 187, 211, 270 – 280,

[18]   N. Meyer-Vernet, "Basics of The Solar Wind", Cambridge University Press, 2007, pp 3, 17, 156, 318, 368, 386

[19]   G. K. Parks, "Physics of Space Plasmas – An Introduction", Second Edition, Westview Press, 2004, pp 6, 16

[20]   J. A. Klimchuk, "Theory of Coronal Mass Ejections", in "Space Weather", edited by P. Song, H. J. Singer, and G. L. Siscoe, Geophysical Monograph Series, Vol. 125, American Geophysical Union, 2001, pp 143

[21]   S. W. Kahler, "Origin and Properties of Solar Energetic Particles in Space", in "Space Weather", edited by P. Song, H. J. Singer, and G. L. Siscoe, Geophysical Monograph Series, Vol. 125, American Geophysical Union, 2001, pp 109 – 120

[22]   J. Hundhausen, "The Solar Wind", in "Introduction to Space Physics", edited by M. G. Kivelson & C. T. Russell, Cambridge University Press, 1995, pp 91 – 128

[23]   W. Baumjohann, R. A Treumann, "Basic Space Plasma Physics", Imperial College Press, 2004, pp 19 – 33

[24]   R. A. Wolf, "Magnetospheric Configuration", "Introduction to Space Physics", edited by M. G. Kivelson & C. T. Russell, Cambridge University Press, 1995, pp 289 – 327

[25]   W. J. Hughes, "The Magnetopause, Magnetotail, and Magnetic Reconnection", in "Introduction to Space Physics", edited by M. G. Kivelson & C. T. Russell, Cambridge University Press, 1995, pp 227 – 284

[26]   F. F. Chen, "Introduction to Plasma Physics and Controlled Fusion, Volume 1: Plasma Physics", Second Edition, Plenum Press, 1984, pp 19 – 34

[27]   L. F. McNamara, "The Ionosphere: Communications, Surveillance, and Direction Finding", Krieger Publishing Company, 1991, pp 17 – 28, 105 – 121

[28]   G. S. Tsolis, T. D. Xenos, "Seismo-Ionospheric Coupling Correlation Analysis of Earthquakes in Greece, using Empirical Mode decomposition", Nonlinear Processes Geophysics, 16, 2009, pp 123, 124

[29]   R. L. McPherron, P. O'Brien, "Predicting Geomagnetic Activity: The D_{st} Index", in, "Space Weather", edited by P. Song, H. J. Singer, and G. L. Siscoe, Geophysical Monograph Series, Vol. 125, American Geophysical Union, 2001, pp 339 – 345

[30]   R. L. McPherron, "Magnetospheric Dynamics", in "Introduction to Space Physics", edited by M. G. Kivelson & C. T. Russell, Cambridge University Press, 1995, pp 400 – 442

[31]   M. Moldwin, "An Introduction to Space Weather", Cambridge University Press, 2008, pp 80 – 89

[32]   L. J. Lanzerotti, "Space Weather Effects on Technologies", in, "Space Weather", edited by P. Song, H. J. Singer, and G. L. Siscoe, Geophysical Monograph Series, Vol. 125, American Geophysical Union, 2001, pp 11 – 20

[33]   M. J. Caruso, C. H. Smith, *et al*, "A New Perspective on Magnetic Field Sensing", Honeywell Microelectronics and Precision Sensors, [Online resource: http://www51.honeywell.com/aero/], pp 2 – 4, 9 – 13

[34]   J. E. Lenz, "A Review of Magnetic Sensors", Proceedings of the IEEE, Vol. 78, No.6, 1990, pp 973, 976, 977, 979, 980

[35]   A. Edelstein, "Advances in Magnetometry", Journal of Physics: Condensed Matter 19, IOP Publishing, 2007, pp 3, 4, 6, 9

[36]   M. H. Acuña, "Space-based Magnetometers", Review of Scientific Instruments, Vol. 73, Is. 11, 2002, pp 3717 – 3736

[37]   C. Reig, *et al*, "Magnetic Field Sensors Based on Giant Magnetoresistance (GMR) Technology: Applications in Electrical Current Sensing", Sensors, Vol. 9, Issue 10, pp 7919 – 7942

[38]   G. Le, W. J. Burke, *et al*, "C/NOFS Measurements of Magnetic Perturbations in the Low-latitude Ionosphere during Magnetic Storms", Journal of Geophysical Research, Vol. 116, 2011, pp 1 – 11

[39] M. G. Kivelson, "Pulsations and Magnetohydrodynamic Waves", in "Introduction to Space Physics", edited by M. G. Kivelson & C. T. Russell, Cambridge University Press, 1995, pp 330 – 353

[40] R. L. Kessel, I. R. Mann, *et al*, "Correlation of Pc5 Wave Power Inside and Outside the Magnetosphere during high Speed Streams", Annales Geophysicae 21, European Geosciences Union, 2003, pp 1 – 13

[41] J. Clarke, A. I. Braginski, (Editors), "The SQUID Handbook, Vol. I Fundamentals of SQUIDs and SQUID Systems", WILEY-VCH Verlag GmbH & Co., 2004, pp 5 – 10, 31 – 41, 44 – 46, 48, 128, 131, 141, 144, 188 – 190, 203, 294

[42] K. Suzuki, Y. Okabe, "Optimization of a dc SQUID Magnetometer to Minimize the Field Resolution", IEEE Transactions On Applied Superconductivity, Vol. 5, No. 2, 1995, pp 2172.

[43] R. Kleiner, D. Koelle, *et al*, "Superconducting Quantum Interference Devices: State of the Art and Applications", in Proceedings of the IEEE, Vol. 92, No. 10, October 2004, pp 1534 – 1548

[44] W. Buckel, R. Kleiner, "Superconductivity – Fundamentals and Applications", Second, Revised and Enlarged Edition, WILEY-VCH Verlag GmbH & Co., 2004, pp 410, 417, 426

[45] R. L. Fagaly, "Superconducting quantum interference device instruments and applications", Review Of Scientific Instruments 77, 101101, American Institute of Physics, 2006, pp 38 – 40.

[46] J. Vrba, S. E. Robinson, "Signal Processing in Magnetoencephalography", Methods, Vol. 25, Is. 4, Elsevier Science 2001, pp 249 – 271.

[47] V. Schultze, R. Stolz, *et al*, "Magnetic field measurements using very sensitive SQUIDs", in Proceedings of the 27th General Assembly of the International Union of Radio Science (URSI), Maastricht, Netherlands, 2002.

[48] S. Gaffet, Y. Guglielmi, *et al*, "Simultaneous Seismic and Magnetic Measurements in the Low-Noise Underground Laboratory (LSBB) of Rustrel, France, during the 2001 January 26 Indian Earthquake", Geophysical Journal International, Vol. 155, Is. 3, 2003, pp 981 – 990.

[49] G. Waysand, E. Pozzo di Borgo, *et al*, "Azimuthal Analysis of [SQUID]2 Signals for Mesopause and Sprites Excitations", in the inter-Disciplinary Underground Science and Technology (i-DUST) Conference 2010, EDP Sciences, 2011, pp 1

[50] X. Zhang, X. Shen, "Electromagnetic Anomalies around the Wenchuan Earthquake and their Relationship with Earthquake Preparation", International Journal of Geophysics, Vol. 2011, Article ID 904132, Hindawi Publishing Corporation, pp 1 – 7.

[51] A.K. Gwal, S. K. Jain, *et al*, "Study of Ionospheric Perturbations during Strong Seismic Activity by Correlation Analysis Method", Asian Journal of Earth Sciences, Academic Journals Inc., 2012, pp

[52] S. S. Kouris, P. Spalla, B. Zolesi, "Could ionospheric variations be Precursors of a Seismic Event? A Short Discussion," Annals of Geophysics, Vol. 44, No. 2, 2001, pp 395 – 402

[53] S. S. De, B. K. De*, et al*, 'Studies on the Precursors of an Earthquake as the VLF Electromagnetic Sferics", Romanian Journal of Physics, Vol. 56, No. 9–10, pp 1208 – 1227

[54] P. Bloomfield, "Fourier Analysis of Time Series – An Introduction", Second Edition, John & Sons Inc., 2000, pp 8, 19 – 21

[55] S. V. Vaseghi, "Advanced Digital Signal Processing and Noise Reduction", Second Edition, John wiley & Sons Ltd, 2000, pp 264 – 273

[56]   K. F. Riley, *et al*, "Mathematical Methods for Physics and Engineering", Cambridge University Press, 2006, pp 84 – 93, 140, 415 – 417, 426

[57]   M. Båth, "Spectral Analysis in Geophysics", Elsevier Scientific Publishing Company, 1974, pp 26, 172.

[58]   R. Wrede, M. R. Spiegel, "Theory and Problems of Advanced Calculus", Second Edition, Schaum's Outline Series, The McGraw-Hill Companies, 2002, pp 340, 342

[59]   W. H. Press, S. A. Teukolsky, *et al*, "Numerical Recipes in C – The Art of Scientific Computing", Second Edition, Cambridge University Press, 2002 Reprint, pp 498 – 505, 538, 550

[60]   Y. W. Lee, J. B. Weisner, T. P. Cheatham Jr., "The Application of Correlation Functions in the Detection of Small Signals in Noise", Technical Report No. 141, Research Laboratory of Electronics, Massachusetts Institute of Technology, 1949, pp1

[61]   J. Marfaing, J.J Bois, *et al*, "About the World-wide Magnetic-background Noise in the Millihertz Frequency Range", EPL Journal, 2009, pp 1 – 5.

[62]   V. V. Surkov, O.A. Pokhotelov, *et al*, "Excitation of the Ionospheric Resonance Cavity by Neutral Winds at Middle Latitudes", Annales Geophysicae, European Geosciences Union, 2004, pp 2877

[63]   S. K. Sung, K. H. Kim, *et al*, "Simultaneous Ground-based and Satellite Observations of Pc5 Geomagnetic Pulsations: A Case Study Using Multipoint Measurements", Earth Planets Science, Vol. 58, 2006, pp 873, 874